Die approbierte Originalversion dieser Diplom-/Masterarbeit ist an der Hauptbibliothek der Technischen Universität Wien aufgestellt (http://www.ub.tuwien.ac.at).

The approved original version of this diploma or master thesis is available at the main library of the Vienna University of Technology (http://www.ub.tuwien.ac.at/englweb/).

DIPLOMARBEIT

Spatiotemporal Analyses of Remotely Sensed Soil Moisture with Respect to Regional Climate Modes and Solar Activity in Australia

Ausgeführt am Institut für Photogrammetrie und Fernerkundung
zum Zwecke der Erlangung des akademischen Grades eines Diplom-Ingenieur

unter der Leitung von
Univ.Prof. Dipl.-Ing. Dr.techn. Wolfgang Wagner

und der Betreuung durch
MSc. Dr.rer.nat. Wouter Dorigo

eingereicht an der Technischen Universität Wien
Fakultät für Mathematik und Geoinformation
von

Bernhard Bauer-Marschallinger

Matrikelnummer 0526855
Brandstatt 4
4650 Edt bei Lambach

Wien, am 15. Mai 2012 . . . . . .

Abstract

Soil moisture is an important environmental variable with impact on hydrological, meteorological and climatological processes as well as on agriculture and socioeconomics. The interactions between soil moisture and climatological variables are still the subject of research in various scientific disciplines. Climate and, hence, soil moisture variations are related to a number of atmospheric and oceanic periodical phenomena called climate modes. Furthermore, the impact of solar variation on the Earth's climate is still matter of dispute.

Interactions between climate variations and climate modes are particularly strong in Australia. This study explores WACMOS surface soil moisture (SSM) over Australia in the period 1979-2010. This is motivated by the very first possibility of analysing remotely sensed soil moisture variations over a continuous period of 32 years.

The WACMOS data merges passive and active microwave data and offers a sampling of 0.25 degrees in space and one day in time. The soil moisture regime of Australia is assembled and then broken down into monthly and seasonal means as well as corresponding anomalies. An Empirical Orthogonal Functions (EOF) analysis is applied to the SSM data in order to extract major variations in Australia's hydrological conditions. Also Complex EOF (CEOF) techniques are deployed to investigate propagating SSM patterns. The relationships of SSM anomalies and SSM EOFs with climate indices and solar activity are examined with Spearman rank correlation analysis.

Strong relationships are found between Southern Oscillation Index (SOI) and SSM in eastern and northern Australia, especially during southern summer and spring season. Similar connections are detected between Southern Annular Mode Index (SAMI) and SSM during summer and spring. The Indian Ocean Dipole Mode Index (IODMI) is coupled with SSM variations in the western parts of the continent, especially in autumn and winter season. However, this connection is detected to emerge since the late 1990s. Solar radio flux (F10.7) does not show significant relations to Australian SSM signals. The findings agree with previous research on atmospheric and oceanic oscillations and their impact on Australia's climate. It is shown that the WACMOS data properly reproduces Australia's soil moisture conditions and enables long-term analysis of hydrological processes.

Kurzfassung

Der Umweltparameter Bodenfeuchte ist ein essentieller Faktor in Hydrologie, Wetter und Klima aller Ökosysteme der Erde. Bodenfeuchte bildet des Weiteren die Grundlage für Land - und Viehwirtschaft und hat somit weitreichenden Einfluss auf gesellschaftliche und wirtschaftliche Prozesse. Der Zusammenhang zwischen Bodenfeuchte und anderen Umweltparametern ist komplex und ist Gegenstand aktueller Forschung verschiedener Disziplinen. Klimatische Bedingungen, und somit auch Bodenfeuchte, befinden sich im stetigen Wandel und sind Schwankungen unterworfen, die periodischen Vorgängen in den Ozeanen und der Atmosphäre zugeordnet werden. Darüber hinaus existiert mit der variierenden Sonnenaktivität eine weitere Größe, deren möglicher Einfluss auf das Klima der Erde bis heute ungeklärt ist.

Auf dem Kontinent Australien sind die Zusammenhänge zwischen hydrologischen Bedingungen und klimatischen Schwankungen besonders spürbar. Diese Diplomarbeit untersucht diese Zusammenhänge mit Bezugnahme auf die WACMOS Fernerkundungsdaten über Oberflächenbodenfeuchte (SSM) in Australien von 1979 bis 2010. Die Motivation dahinter liegt in der Tatsache, dass hiermit zum ersten Mal eine Untersuchung von satellitengestützten Bodenfeuchtemessungen über einen Zeitraum von 32 Jahren möglich ist.

Der WACMOS Datensatz verbindet SSM-Daten von passiven und aktiven Mikrowellensystemen und bietet tägliche Werte bei einer räumlichen Auflösung von 0,25 Grad. Im Zuge dieser Arbeit wurden diese Daten in Monats- und Saisonmittelwerte mit zugehörigen Anomalien umgerechnet. Um die wichtigsten Schwankungen in der Bodenfeuchte Australiens herauszulösen, wurde eine Hauptkomponentenanalyse (EOF) durchgeführt. Des Weiteren wurde eine komplexe EOF Analyse (CEOF) betrieben, um zeitliche Variationen zu erkennen. Schlussendlich wurden die SSM Anomalien und die Ergebnisse der EOF Zerlegung in Beziehung zu Klimaindizes und Sonnenaktivität gesetzt und mit Methoden der Spearman-Korrelationsrechnung untersucht.

Starke Zusammenhänge wurden zwischen dem Southern Oscillation Index (SOI) und der Bodenfeuchte in Nord- und Ostaustralien gefunden, besonders im Südsommer und -frühling. Für den Southern Annular Mode Index (SAMI) kamen vergleichbare Ergebnisse zu Tage. Auf der anderen Seite des Kontinents wurde ein Zusammenhang im Südwinter und -herbst zwischen SSM

und dem Indian Ocean Dipole Mode Index (IODMI) gefunden. Dieser konnte jedoch nur ab den 1990er Jahren festgestellt werden. Bezüglich Sonnenaktivität, gemessen an der Radiointensität F10.7, konnte keine klare Verbindung entdeckt werden. Die Resultate stimmen mit vorhergehenden Analysen über ozeanischen und atmosphärischen Schwankungen und deren Einfluss auf Australien überein. Darüber hinaus wurde demonstriert, dass die WACMOS SSM Daten sowohl die Bodenfeuchte von Australien zufriedenstellend wiedergeben als auch klimatische Langzeitanalysen erlauben.

Danksagung

Ich bin dankbar, nicht weil es vorteilhaft ist, sondern weil es Freude macht.

Seneca

Diese Diplomarbeit entstand am Institut für Photogrammmetrie und Fernerkundung (IPF) und ich möchte daher in erster Linie meinen Kollegen danken, die mir stets mit einem offenen Ohr zur Seite standen. Besonders hervorheben möchte hier meinen Betreuer Wouter Dorigo, der mit Fachkenntnis und Sorgfalt zum Gelingen dieser Arbeit beigetragen hat. An dieser Stelle möchte ich auch Wolfgang Wagner und Marcela Doubkova danken, die mich oft mit ihrer wissenschaftlichen Expertise zu neuen Fragestellungen und Experimenten inspirierten.

Meine Worte des Dankes richten sich auch an all die hellen Köpfe, die im Rahmen des WACMOS Projekts dafür gesorgt haben, dass mir mit dessen Bodenfeuchtedaten ein neuartiger, aktueller Datensatz als Experimentierfeld zu Verfügung stand. Ich möchte hier nicht nur die Kollegen am IPF erwähnen, sondern auch die Forschungsgruppe um Richard de Jeu, die maßgeblich an der Erstellung der WACMOS Daten beteiligt war.

Die Fertigstellung der Diplomarbeit bedeutet auch den erfolgreichen Abschluss meines Studiums an der TU Wien und ich möchte daher hier auch all jenen herzlich danken, die mich vor und während meines Studiums begleitet und unterstützt haben oder mit mir auch ordentlich fortgegangen sind. Besonderen Dank möchte ich meiner ganzen Familie, vom Opa über meinen Eltern bis zur kleinen Schwester, aussprechen, ohne die dies alles sicherlich nicht, oder zumindest weniger reibungslos, geschähen wäre.

Contents

List of Acronyms viii

List of Figures ix

List of Tables xi

1 Introduction 1

2 Climate Modes and Solar Activity 4

2.1 Climate 4
2.2 Climate Modes 6
2.2.1 El Niño Southern Oscillation 7
2.2.2 Indian Ocean Dipole 10
2.2.3 Southern Annular Mode 12
2.3 Solar Activity 15
2.4 The Climate of Australia 18

3 Soil Moisture and Microwave Remote Sensing 22

3.1 Water Cycle and Soil Moisture 23
3.1.1 Soil Moisture Determination 24
3.2 Microwave Remote Sensing 25
3.2.1 Emission and Scattering 27
3.2.2 Properties of Microwaves 30
3.3 Soil Moisture from Spaceborne Microwave Systems 32
3.3.1 Radiometer 33
3.3.2 Scatterometer 33
3.3.3 Soil Moisture Retrieval 33

4 Data and Methods 35

4.1 WACMOS Soil Moisture 35

4.2 Correlation Analyses 38
4.2.1 Spearman Rank Correlation 39
4.3 Empirical Orthogonal Functions 40
4.3.1 Basic EOF Analysis 41
4.3.1.1 EOFs from Eigenvalue Analysis 43
4.3.1.2 EOFs from Singular Value Decomposition 46
4.3.2 Data Gaps 47
4.3.3 Complex EOF Analysis 48
4.3.3.1 Hilbert Transform 49
4.3.3.2 Hilbert EOF Analysis 51
4.3.4 EOF Interpretation 51
4.4 Implementation 53

5 Results and Discussion **55**
5.1 Resampled WACMOS SSM over Australia 55
5.2 Correlation Maps 59
5.3 EOF Analyses 62
5.3.1 EOFs from Time Series 1979-2010 63
5.3.2 EOF Seasonal Decomposition 1979-2010 66
5.3.3 EOFs from Time Series 1998-2010 72
5.4 CEOF Analyses 75
5.4.1 CEOFs from Time Series 1979-2010 75
5.4.2 CEOFs from Time Series 1998-2010 80

6 Conclusion **82**

Bibliography **84**

List of Acronyms

AMSR-E	Advanced Microwave Scanning Radiometer - Earth Observing System
ASCAT	Advanced Scatterometer
CEOF	Complex EOF
CLINO	Climate Normal
DJF	December-January-February
ECV	Essential Climate Variable
ENSO	El Niño Southern Oscillation
EOF	Empirical Orthogonal Function
F10.7	Solar Radio Flux
GCOS	Global Climate Observing System
IOD	Indian Ocean Dipole
IODMI	Indian Ocean Dipole Mode Index
ITCZ	Inner Tropical Convergence Zone
JJA	June-July-August
MAM	March-April-May
SAM	Southern Annular Mode
SAMI	Southern Annular Mode Index
SMMR	Scanning Multichannel Microwave Radiometer
SOI	Southern Oscillation Index
SON	September-October-November
SSM	Surface Soil Moisture
SSM/I	Special Sensor Microwave Imager
SST	Sea Surface Temperature
TMI	Tropical rainfall Measuring Mission Microwave Imager
WACMOS	WAter Cycle Multimission Observation Strategy

List of Figures

2.1 Global Circulation 5
2.2 Walker Circulation 7
2.3 El Niño and La Niña 8
2.4 SOI Time Series 10
2.5 Indion Ocean Dipole 11
2.6 IODMI Time Series 12
2.7 Southern Annular Mode 13
2.8 SAMI Time Series 15
2.9 F10.7 Time Series 17
2.10 Climate Classification of Australia 19
2.11 Rainfall in Australia 20

3.1 Microwave Bands 25
3.2 Permittivity of Soil 32

4.1 WACMOS Sensors Temporal Coverage 36
4.2 Correlation 38
4.3 EOF Scheme 41
4.4 EOF Vectors 45

5.1 WACMOS Climatology in Australia 56
5.2 SSM Anomaly 1983 58
5.3 SSM Anomaly 1987 58
5.4 SSM Anomaly 1998 58
5.5 SSM Anomaly 2000s 59
5.6 Correlation Maps ENSO, SAM and IOD 60
5.7 IODMI Impact 1998-2010 and F10.7 1979-2010 61
5.8 EOF 1979-2010 64
5.9 Spectrum EOF 1979-2010 65

5.10 EOF 1979-2010 Summer 68
5.11 EOF 1979-2010 Autumn 69
5.12 EOF 1979-2010 Winter 70
5.13 EOF 1979-2010 Spring 71
5.14 EOF 1998-2010 Selection 73
5.15 1st CEOF 1979-2010 77
5.16 2nd CEOF 1979-2010 78
5.17 3rd CEOF 1979-2010 79
5.18 1st CEOF 1998-2010 81

List of Tables

4.1 Specification of WACMOS Sensors 36

5.1 Spearman Coefficient EOF Analysis 1979-2010 65
5.2 Spearman Coefficient EOF Analysis 1979-2010 – Summer 68
5.3 Spearman Coefficient EOF Analysis 1979-2010 – Autumn 69
5.4 Spearman Coefficient EOF Analysis 1979-2010 – Winter 70
5.5 Spearman Coefficient EOF Analysis 1979-2010 – Spring 71
5.6 Spearman Coefficient EOF Analysis 1998-2010 – Selection 74
5.7 Spearman Coefficient CEOF Analysis 1979-2010 76
5.8 Spearman Coefficient CEOF Analysis 1998-2010 80

Chapter 1

Introduction

Only the misfortune of exile can provide the in-depth understanding and the overview into the realities of the world.

Stefan Zweig

This thesis aims to investigate the variation of *soil moisture* in respect to climatic oscillations. Soil moisture is not only an important mirror of dynamics in the hydrological cycle, it is also a main driver of water and energy fluxes at the Earth's surface, located between solid Earth and its atmosphere. Knowledge on relationship of soil moisture with weather and climate patterns is essential for understanding climatological, hydrological and biological processes. Satellite remote sensing offers valuable techniques for monitoring soil moisture conditions on a global scale.

It was in the late 1950s when humanity started to send satellites into the Earth's orbit, based on rapid advance in technology during the cold war. Although the initial motivation was of military nature, a wide field for satellite systems has evolved in the following centuries. Nowadays, there is a huge number of fields in which satellites enable a variety of services and provide a multitude of information. Communication, broadcasting, weather monitoring and positioning are among the most prominent services facilitated by satellite systems.

Moreover, the space borne characteristic also allowed, for the first time, a scientific look of the Earth's weather and climate on a global scale. Now, there are satellite observations in addition to conventional measurements of hydrological, meteorological and climatological parameters. Concerning weather-, climate- and earth sciences, their most important merits of these are the following:

- additional, independent data
- global-scale coverage

- regular, temporal coverage
- relative low costs
- timeliness

In short, our everyday weather forecast is rendered possible by specialized sensors mounted on satellites. Data from optical sensors, sensing in the visible or infra-red range, are ingested into weather prediction models as well as data from systems operating with microwave radiation.

In the course of time, numerous Earth-observing systems have been established. All techniques that allow observations of terrestrial and atmospheric parameters from sky or space can be comprised by the term *remote sensing*. In the 1990s, remote sensing was established as reliable source of data for earth sciences. One goal of remote sensing is the measurement of physical variables of the planet's atmosphere, the oceans and seas, the land surfaces and the ice bodies. This is facilitated by collection and interpretation of electromagnetic (EM) radiation reflected or emitted from objects on the planet. Highly dynamic land surface parameters like soil moisture, snow cover, evapotranspiration, vegetation structure can be observed by means of measuring the electromagnetic properties of terrestrial objects.

However, when talking about climate instead of weather, one has to think in a broader scope. Climate is defined as the sum of all weather appearances at one location in a certain time period. Thus, weather can be seen as an actual realisation of the climate, or if preferred, climate can be described as average weather at a given location (Benestad, 2006). While weather can change very quickly in a sub-daily-scale, climate has a stable character and varies only very slowly over decades or centuries. Consequently, statements about climate should only concern to time periods of at least 30 years (Kuttler, 2008). In fact, the World Meteorological Organization (WMO) framed 30 years as a reference period, called *climate normals* (CLINOs)[1]. For this distance is noted that statistical measures are representative and extreme years are compensated.

The Earth's hydro- and atmosphere underlies a permanent exchange of air and water masses with different thermal and chemical attributes. The main drivers here are the radiation from the sun and the rotation of our planet. The fact, that lower latitudes receive a multitude of energy than higher latitudes forces an exchange of energy. This transport of energy and air and water masses as carrier is known as *planetary circulation*. With the emergence of space born sensors, scientists discovered other forms of oceanic and atmospheric oscillations, called *climate modes*. These modes alter the regular oscillation patterns because of geographical or topographic features. They are clearly distinguishable from the primary, latitude-driven component of the climate system. But the mechanisms behind are not fully understood yet and their amplitude and frequency do not

[1] for example the epochs 1931-60 or 1961-90

strictly follow regular patterns. *El Niño Southern Oscillation*, *Southern Annular Mode* or *Indian Ocean Dipole* are prominent representatives of these phenomena (Kraus, 2004).

The energy emitted from the Sun into space is called *solar activity* and it is not constant. The change of the Sun's emitted radiation has distinct periodic components and the major period is 11 years, known as *solar cycle*. Historically, this oscillation was observed by counting sunspots, but nowadays it is preferred to measure the amplitude of the sun's radiation (at certain wavelengths). The impact of this extra-terrestrial variable on variations of weather patterns (or climate) on Earth is still in question. Today, science on this matter is controversially and no clear answers have yet been found (Benestad, 2006).

The data investigated in this study was collected from six satellite sensors and contains information about *Surface Soil Moisture* (SSM) from 1978 to 2010. It was developed during the WACMOS project (Liu et al., 2012, in review) and is the very first global dataset describing soil moisture over such a long time span. The subject of this thesis is the analysis of the relationship between the SSM signal and climatic variations of the Australian continent over a period of 32 years. In order to decompose the comprehensive dataset, basic and complex EOF Analysis have been used.

So why soil moisture? And which climatic variations? Soil moisture is the water at the thin layer between solid earth and atmosphere and it is very sensitive to changes in precipitation, temperature, solar irradiation, as well as humidity, wind, etc.. It is an important mirror of climatic conditions and also a major driver of the local climate (Legates et al., 2010). Thus, knowledge about soil moisture allows the examination of changes in climate and weather patterns.

Finally, the continent Australia was selected for this study due to its exposed situation to variations of global and regional climate. Surrounded by wide oceans and located in the subtropics, Australia's hydrological parameters react rather quickly and directly to changes in global circulation patterns. Its overwhelming semiarid characteristic and the homogeneous topography makes Australia to an almost ideal mirror of phenomena like climate modes or, on the long run, climate change.

Chapter 2

Climate Modes and Solar Activity

Climate is what we expect, weather is what we get.

Mark Twain

2.1 Climate

The earth's climate is a complex system with an uncountable number of variables and thus does not allow for a simple explanation. It embraces subjects as solar heating, atmospheric and oceanic circulation, land processes and anthropogenic activities (Benestad, 2006). Physical and chemical properties like temperature, pressure, humidity, albedo, etc. contribute to climate and geographic features. The latter contains the arrangement of continents and oceans and the position of mountain ranges and water currents. This study gives an overview on the relationship between climate variations in Section 2.2, solar activity in Section 2.3 and soil moisture in Section 3.1.

The Earth's climate (and the weather) is primarily driven by the energy received from the Sun, which is strongly dependent on the latitude. However, the latitudinal temperature gradient can not be explained in terms of radiative balance alone: Temperatures turn out to be higher at the poles and lower at the equator. This is reasoned by *heat advection* through air and water masses, carrying the Sun's energy from low to high latitudes. This system is called *global circulation* and is displayed in Figure 2.1.
The major characteristic of the Earth's air mass transport is properly explained by the global air circulation with the six-cell circulation model: Air rises at the equator and falls at the poles. But instead of one great circuit in each hemisphere from equator to pole, there are three circuits each. The latitudinal movement of air masses is subject to the Coriolis effect which impacts on the direction of major wind patterns. Instead of moving straight to the poles, the air is deflected laterally

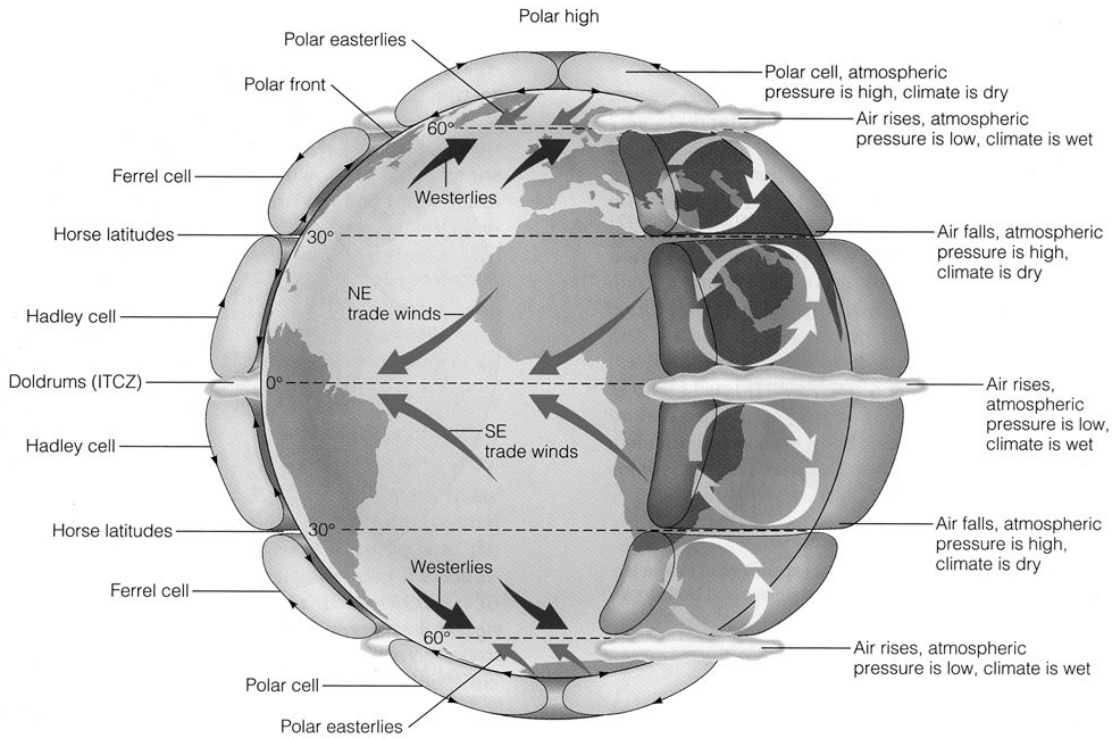

Figure 2.1: *The illustration depicts the six cell model of global circulation and labels major tropospheric cells and streams. Note the influence of the Coriolis effect on wind direction. Graphic from the Santiago Canyon College, California.*

since the Earth, as the reference body, is rotating. All around the globe at 0° and 60° latitude, the cells are divided by low pressure belts. Contrary, at 30°, a high pressure belts builds the frontier of the cells. The low pressure zone around the equator is known as Intertropical Convergence Zone (ITCZ) and is the result of merging trade winds triggering massive air convection. Latter leads to cloud formation and precipitation in these regions.
Local air pressure, wind velocity, humidity and consequently precipitation are strongly dependent on the constellation of the cells. Throughout the year, the position of the cells is varying according to the shift of the ITCZ, due to the inclination of the Earth axis.

Weather can be described highly chaotic and may appear random despite apparently similar patterns. Its prediction is reliable only on short-term due to the enormous number of unknowns. Nevertheless, general patterns and long-term conditions are accessible to science through worldwide observations and analyses of historical records.

Global climate underwent strong variations in the past, for example the alternation of glacial and

inter-glacial periods[1]. Since the last century, humanity experiences an increase of mean global temperature according to an increase in CO_2 and other greenhouse-gases in the atmosphere and several other environmental changes. The term *climate change* integrates all these recent developments.

Climate change is expected to intensify the hydrological cycle and to alter evapotranspiration, with implications for ecosystems and feedback to regional and global climate (Jung et al., 2010). In these times of changing climate conditions, a growing number of extreme weather events and disasters are more and more reported. Current models suggest that more rain will fall, but less often, which will result in a more extreme temporal distribution of water. Today, roughly one billion people lack access to safe drinking water and two billion people lack proper sanitation worldwide. Water shortages are likely to spread into agriculture and the energy sector. Especially the land masses of the southern hemisphere with their high share of areas with semiarid conditions are affected by variations of the hydrological cycle. For the last decade, a general decrease in moisture was observed for the southern hemisphere (Jung et al., 2010).

Furthermore, the ENSO phenomenon (Section 2.2.1) causes substantial fluctuations of precipitation in the Pacific region. As a result, droughts and floods appear regularly with varying intensities in regions that border on the Pacific. Another global climatic phenomenon is called IOD (Section 2.2.2) which describes cyclic variations of heat distribution in equatorial Indian Ocean. Australia (Section 2.4) is considerably exposed to ongoing developments of all critical climate variables. Large parts of the Australian continent are semiarid, and precipitation varies much from year to year. Due to this, droughts and floods are common, and as recent events show, natural hazards can often develop into life-threatening disasters.

Globally, soil moisture, being an indicator of water availability, is expected to decrease over most parts of the Earth's landmass (Gerten et al., 2007). It is therefore important to develop and improve systems recording data on air humidity, rainfall and soil moisture more than ever before.

2.2 Climate Modes

Variations of climate can have a regular cyclic nature, which are known as *climate modes*, or climate patterns. There are yearly, diurnal, seasonal or quasi-periodic cycles for example. They have specific regional impact and often oscillatory behaviour. Some of them are coupled via teleconnections, what means a relationship between weather or climate events in separated areas on the globe. The yearly cycle of the Earth's revolution around the Sun has the biggest amplitude among

[1] ice-ages and warm periods

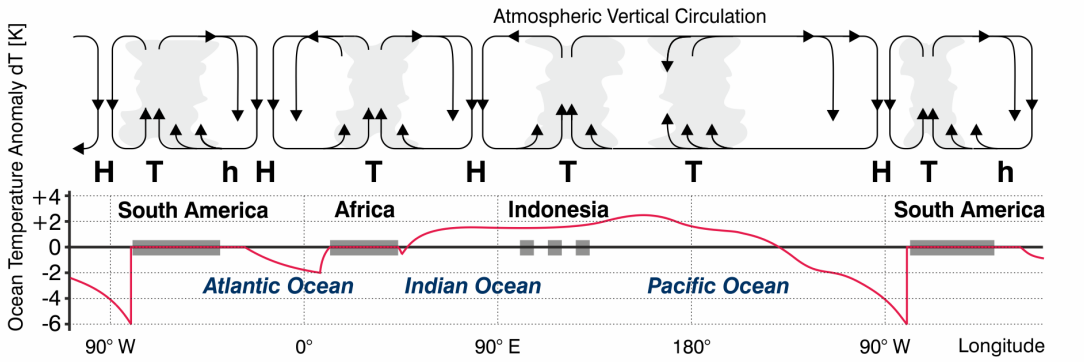

Figure 2.2: *Schematic illustration of the Walker Circulation as a vertical section: Relative SST along the equator is noted as red line. Above, major air circulation and convective cloud generation is shown. Climate modes can alter these patterns and consequently air pressure and precipitation regimes are modified. Adopted from (Schönwiese, 1994)*

climate modes, followed by the *thermohaline circulation*[2] and *ENSO*. Climate modes have been detected as major climate drivers for Australian rainfall variations.

2.2.1 El Niño Southern Oscillation

The El Niño Southern Oscillation (ENSO) refers to climate phenomena resulting from interactions between coupled large-scale oceanic and atmospheric circulation processes in the pacific region. It can be described as a global circulation of water and air masses off the landmasses at the western and eastern borders of the Pacific Ocean. This behaviour is natural. Its teleconnections to other parts of the planet as well as the interference with climate change is not completely understood (Kraus, 2004). While El Niño and La Niña describe oceanic processes, Southern Oscillation only refers to the atmospheric effects. These terms are related to Christmas season, when the effects appear typically in (Spanish speaking) South America. The periodicity of the circulation is irregular and ranges from two to seven years. ENSO is the most important coupled ocean-atmosphere phenomenon to cause global climate variability on interannual scales.

It is driven by cyclic cooling and warming of the equatorial Pacific coupled with fluctuations of an atmospheric global-scale tropical and subtropical surface pressure pattern. Accordingly, in (Kuttler, 2008) is noted that the ENSO is strongly coupled with variations of the tropical *Walker Circulation* (Figure 2.2). This term describes inner-tropical energy exchange between the continents and oceans and governs the location of high pressure systems in the tropics. During El Niño

[2] global system of ocean fluxes due to heat and salt divergence

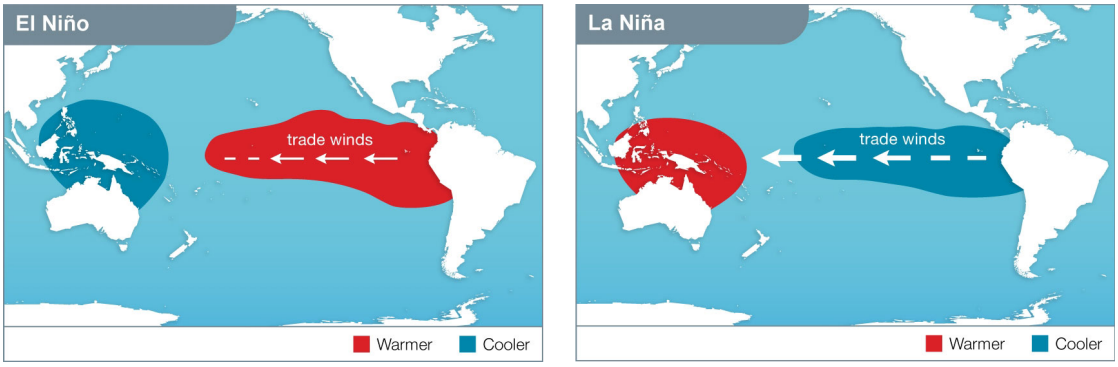

Figure 2.3: *The maps show the effects during ENSO events. In the eastern Pacific, along the coast of South America, the northward flowing Humboldt current brings cooler water from the Southern Ocean to the tropics. South-easterly trade winds cause the ocean currents in the eastern Pacific to draw water from the deeper ocean towards the surface ("upwelling") and pushes the water westward. The left map shows SST anomalies during El Niño conditions. The trade winds are weakened and less cool water is raised. In turn, because of weakening or an inversion of the Walker Circulation, warm water flows from Indonesia eastwards and eastern Pacific is warmed.*
The second map displays La Niña conditions, which strengthen the regular pattern of warming western Pacific and cooling eastern Pacific. Graphics from the Department of Primary Industries, Victoria, Australia.

conditions, the Walker Circulation is weakened or even reversed over the Pacific Ocean and the gradient off South America is less steep what results in warmer surface waters (see Figure 2.3).

The term El Niño is used to describe the appearance of warmer-than-usual water along the coasts of Ecuador and Peru, while the term La Niña describes a cooling of these waters in eastern Pacific. During strong El Niño events, SST of 5 °C above long-term mean have been measured (Kraus, 2004). The two cases are the extremes of ENSO variation and create rainfall and temperature fluctuations mainly in the equatorial Pacific region, and to a lesser extent, all around the world. The impact varies across the globe and can result in flooding in some regions and in droughts in others.

ENSO significantly impacts on rainfall, drought and tropical cyclone behaviour in the pacific region and, via teleconnection, in many parts of the world. During an El Niño [3] event, the prevailing trade winds weaken, which are the drivers for up-welling sea currents. As a consequence, *sea surface temperatures (SST)* warm and surface ocean currents are altered. This weakens trade wind even more and introduces a positive feedback mechanism (Solomon et al., 2007). El Niño events decrease precipitation in Indonesia and Australia and increase rainfall in commonly dry Peru and neighbouring countries. In southern Africa, an El Niño event is often followed by drought. La

[3] phase of the ENSO with big negative amplitude

Niña intensifies low pressure systems in western Pacific and brings additional rain to Indonesia and northern/eastern Australia, where floods are likely then. (Chiew et al., 1998) outlines the relationship of ENSO to Australia rainfall and drought patterns. The study also identifies Australia as notably vulnerable to floods and droughts because of limited water resources and arid character. On the other end of the Ocean, off South America, very dry conditions are experienced during La Niña periods. Contrary, in southern Africa a La Niña event is often followed by flooding. The last strong El Niño event appeared 1997/98 which was followed by a number of La Niño episodes until 2001.

Together with a normal phase, El Niño (a warm event) and La Niña (a cold event) form the three phases of ENSO. The latter can be seen as amplified form of the normal phase, since the waters in front of the west coast of South America are cold in general. The air pressure in the western Pacific is higher during El Niño and lower during La Niña. This is used for determination of several indices describing the status of ENSO.

Southern Oscillation Index An important statistical value here is the *Southern Oscillation Index (SOI)* that is based on the differences in the atmospheric pressure between Tahiti in equatorial Pacific and Darwin in northern Australia (West Pacific). SOI is used to quantify the strength of an ENSO event. Negative values indicate El Niño conditions and positive values La Niña conditions. Apart from indices based on atmospheric pressure variations, changes in sea surface temperatures in the central and eastern Pacific are used for descriptions of ENSO. The SOI gives an indication of the development and intensity of ENSO and consequently of the strength of El Niño and La Niña events.

Persistent negative SOI-values lower than −8 often indicate El Niño episodes. These negative values are usually accompanied by continuing warming of the central and eastern tropical Pacific Ocean, a decrease in the strength of the Pacific trade winds, and a reduction in winter and spring rainfall over much of eastern and northern Australia. In contrast, persistent positive values of the SOI greater than +8 are typical for a La Niña episode. This is associated with stronger Pacific trade winds and warmer sea temperatures to the north of Australia. Waters in the central and eastern tropical Pacific Ocean become cooler during this time. Together, these factors give an increased probability that eastern and northern Australia will be wetter than normal.

There are different methods to calculate the SOI. The method used in this study[4] is the *Troup SOI* (see fig:soi time series) which is the standardised anomaly of the *Mean Sea Level Pressure (MSLP)*

[4] and by the Australian Bureau of Meteorology (BOM)

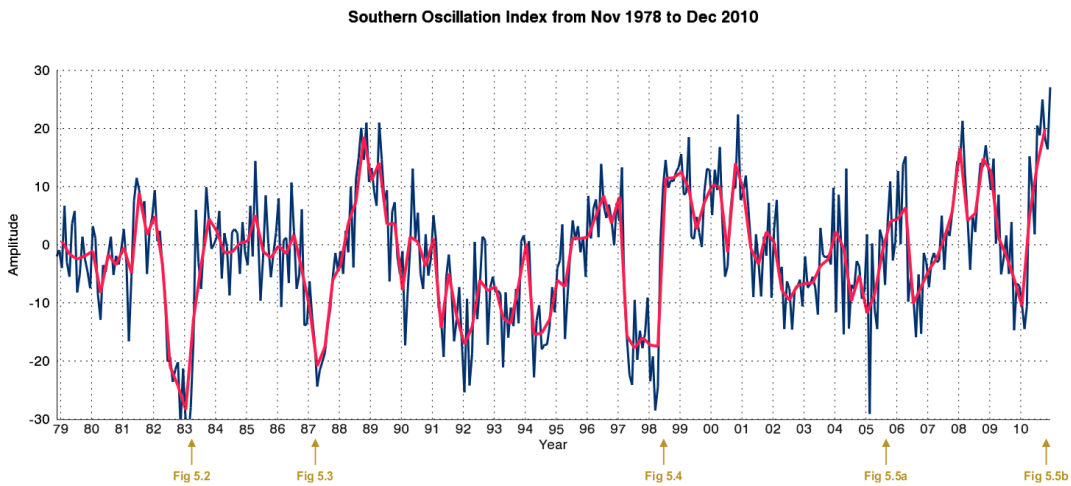

Figure 2.4: *The plot shows values of monthly SOI in blue and seasonal SOI in red over the WACMOS period 1979-2010. The last decades featured a very intensive ENSO series with several ENSO events occurring in the period: El Niño episodes (dry events in Australia) in 1982-83, 1987-88, 1991-1993, 1994-95, exceptional in 1997-98, 2002-03, 2006 and 2009 and La Niña episodes (wet events) in 1988-89, 1995-97, prolonged in 1998-2001, 2008 and exceptional since 2010. Yellow arrows indicate events outlined in Chapter 5.*

difference between Tahiti in the central Pacific Ocean and Darwin in northern Australia. The difference in MSLP for the month m is

$$\Delta_m = p_{Tm} - p_{Dm} \tag{2.1}$$

where p_{Tm} is the monthly average MSLP in Tahiti and p_{Dm} in Darwin. The SOI is then defined as

$$SOI = 10\frac{\Delta_m - \bar{\Delta}_m}{\sigma_{\Delta_m}} \tag{2.2}$$

where $\bar{\Delta}_m$ is the mean of the (calendar)-month m, σ_{Δ_m} is the standard deviation of the (calendar)-month. The factor 10 is conventional so that the SOI ranges from about −35 to +35. The BOM computes the value for every month.

2.2.2 Indian Ocean Dipole

A similar climate phenomenon to ENSO is the Indian Ocean Dipole (IOD), which terms an irregular cycle of warming and cooling of ocean waters in the equatorial Indian Ocean. The dipole structure is characterised by alternation of sea surface temperatures in the western basin on the

one side and waters off Sumatra (Timor Sea) on the other side. These oceanic oscillations are coupled to atmospheric effects which appear as variations in direction and strength of equatorial- and trade wind, what is accompanied by precipitation anomalies (see Figure 2.5).

The phases of the IOD oscillation are termed positive, negative and neutral. During a positive event, the eastern Indian Ocean is cooler than normal and in the west, there is warmer water than usual. Equatorial surface winds, which blow towards east in a normal summer season, are weakened or reversed direction and transport heat and moisture westwards and cause a shallower thermocline[5] off Sumatra (Saji et al., 1999). This all results in reduced evaporation, convective activities and precipitation in Indonesia and Australia and augmented in eastern Africa. These effects are inverted during a negative event and cause additional precipitation in Indonesia and Australia. Here, north-westerly winds are generated that pick up moisture from the ocean and carry it deep into Australia's south-eastern parts. Observations showed that each of these events last about six months and do not follow reliably any periodic schemata.

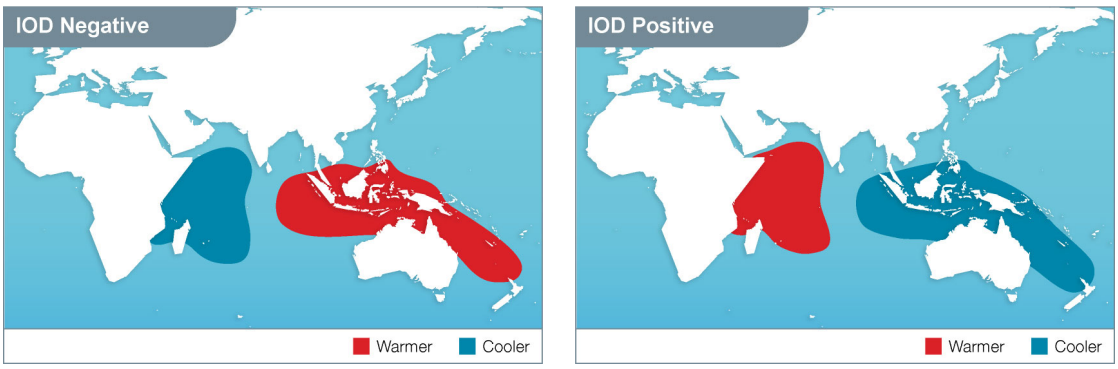

Figure 2.5: *On the left, a situation during a negative phase of the IOD is shown. At the eastern Indian Ocean, warmer water is at the surface and greater precipitation in the region is the consequence. In contrast, cooler and drier conditions are experienced in eastern Africa. The right image shows the inverse situation during a positive phase of the IOD with completely contrary conditions. Graphics from the Department of Primary Industries, Victoria, Australia*

Indian Ocean Dipole Mode Index The IOD is commonly measured by the *Dipole Mode Index (DMI)*, which is the difference between sea surface temperature (SST) in the western δ_W between 50° – 70° east and 10° south - 0° north and the eastern δ_E between 90° – 110° east and 10°-0° south at equatorial Indian Ocean. The DMI-values in °C are commonly normalised by its

[5] transition zone of warmer, superficial and mixed ocean layer to colder, deeper and calmer water

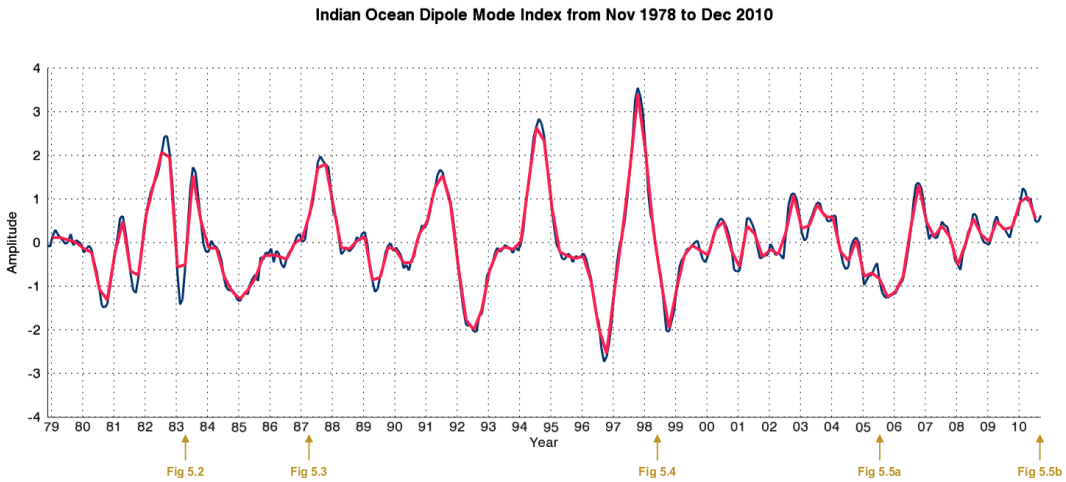

Figure 2.6: *The plot shows values of monthly SST IODMI in blue and seasonal SST IODMI in red over the WACMOS period 1979-2010. Significant positive periods (dry event in Australia) have been in 1982, 1983, 1994, 1997 and 2007 and negative periods (wet event) have been in 1989, 1992, 1996 and 2005.*

standard deviation so that the Index ranges from −3 to +3:

$$DMI = \frac{\delta_W - \delta_E}{\sigma_{DMI}} \tag{2.3}$$

For the period 1979-2010 the IODMI is plotted in Figure 2.6.

Again, a positive IODMI period is characterised by cooler than normal water in the tropical eastern Indian Ocean and warmer than normal water in the tropical western Indian Ocean. If the conditions sustain, this is associated with a decrease in rainfall over central and southern Australia. As opposite, a negative IODMI period is characterised by warmer than normal water in the tropical eastern Indian Ocean and cooler than normal water in the tropical western Indian Ocean. This pattern has been shown to be associated with an increase in rainfall over southern Australia.

2.2.3 Southern Annular Mode

In the region of the Southern Ocean there also is an alternating pattern. It is called *Southern Annular Mode (SAM)* (also known as *Antarctic Oscillation (AAO)*) and terms an oscillating pattern of weaker and stronger westerly winds between mid and high latitudes on the southern hemisphere.

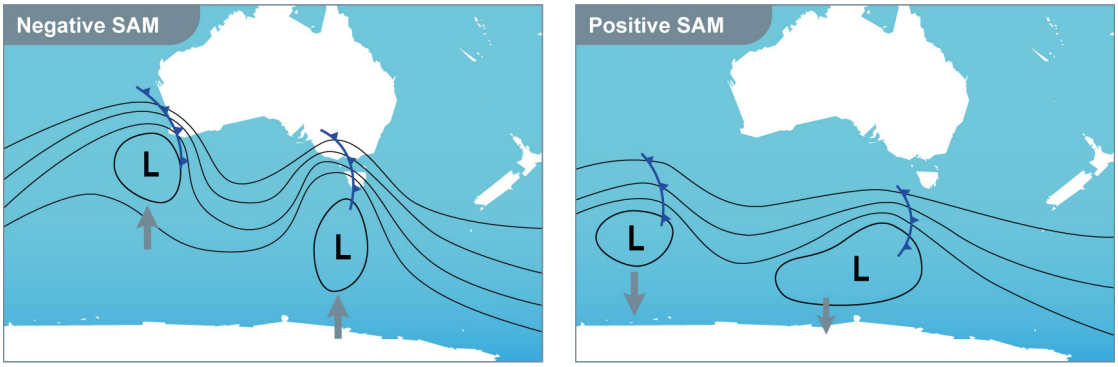

Figure 2.7: *These both images display the position of prevailing westerly wind belts during a negative (left) and positive (right) SAM event. Typical latitudinal positions during southern summer are shown. Graphics from the Department of Primary Industries, Victoria, Australia.*

Recent studies suggest that the SAM's influence on Australian hydroclimatology may be equal or even greater than the influence of ENSO or IOD in certain regions during particular seasons and epochs (Ho et al., 2011).

SAM refers to the latitudinal movement of the belt of westerly winds that dominate the middle to higher latitudes of the southern hemisphere[6]. Typically for a climate mode, SAM shows an dipole behaviour and its extreme events last for 10 to 14 days. However, the time in-between two peaks of the oscillation is quite random, but is normally in the range of a week to a few months.

The fundamental driver of SAM is the non-uniform heating of the Earth and the resulting energy transport from north to south. The zonal flow is located between 55° – 60° and 35° – 40° south latitude, where the low-pressure zone is sandwiched between the high pressure zones at the pole and the subtropics. SAM is related to latitudinal movement of the westerly wind belt between Antarctica on the one hand and South America, Africa and Australia on the other hand. The strong westerly winds regularly drive rain-bearing storm systems and cold fronts from west to east. As a consequence, the wind belt (the *southern jet stream*) governs how far north rain-bearing cyclones can move (see Figure 2.7). One should keep Figure 2.1 in mind.

During a so-called negative SAM event an equator-ward expansion of the jet stream is experienced and the belt of strong westerly winds expands towards the equator. This shift in the westerly winds tempts storm systems and lower pressure to go more north.

Conversely, during a positive SAM event, the belt of westerly winds contracts towards the south pole. In all seasons, significant rainfall anomalies of positive SAM are mainly confined to the

[6] there is an analogue in the north

southern half of the continent, but the contrast between the pattern of rainfall anomalies in autumn/winter and spring/summer is striking (Hendon et al., 2007): In autumn and winter, positive SAM is associated with decreased rainfall in south-east and south-west of Australia. In contrast, during spring/summer, positive SAM conditions are associated with increased rainfall in these regions. This is due to the relative position of the jet streams over the continent. In winter, the low pressure belt is regularly located south of Australia. If it is then contracted towards the south pole, rainfall is likely to turn out to be smaller.

In Australia, SAM explains 10% to 15% of weekly rainfall variability in the south-west and south-east during winter and on the south-east coast during spring and summer, which is comparable to or larger than the variability in these regions associated with ENSO (Hendon et al., 2007). An increasing trend regarding SAM is appearing recently. During the summer and autumn months (December through to May), SAM shows an increasing tendency to remain in a positive phase, with westerly winds contracted towards the south pole. SAM's impact on rainfall and consequently on soil moisture varies greatly depending on season and region and is therefore not straight-forward.

Southern Annular Mode Index The difference in sea-level air pressure is exploited as a measure for the strength of SAM. There are a number of different, but rather similar indices that number SAM conditions. A commonly used index is the *Southern Annular Mode Index (SAMI)* that is defined as the difference between the normalised monthly zonal mean sea level pressure (MSLP) between 40° and 70° south. SAMI is a modification of the AAO index defined by (Gong and Wang, 1999). Latter is the difference in the normalised zonal mean SLP between 40° and 65° south. There is higher correlation in the zonal mean SLP anomalies between 40° and 70° south that between 40° and 65° south and therefore SAMI reflects better the variance of the climate mode over Australia. SAMI was chosen for this study because of data availability reasons and high correlation to other SAM indices as shown in (Ho et al., 2011).

The index (Figure 2.8) is determined as followed for each month and season (e.g. DJF) and ranges from −6 to +6:

$$SAMI = P^*_{40} - P^*_{70} \tag{2.4}$$

Here, the P^* notation stands for normalised zonally mean sea level pressure for each month, indexed by southern latitude.

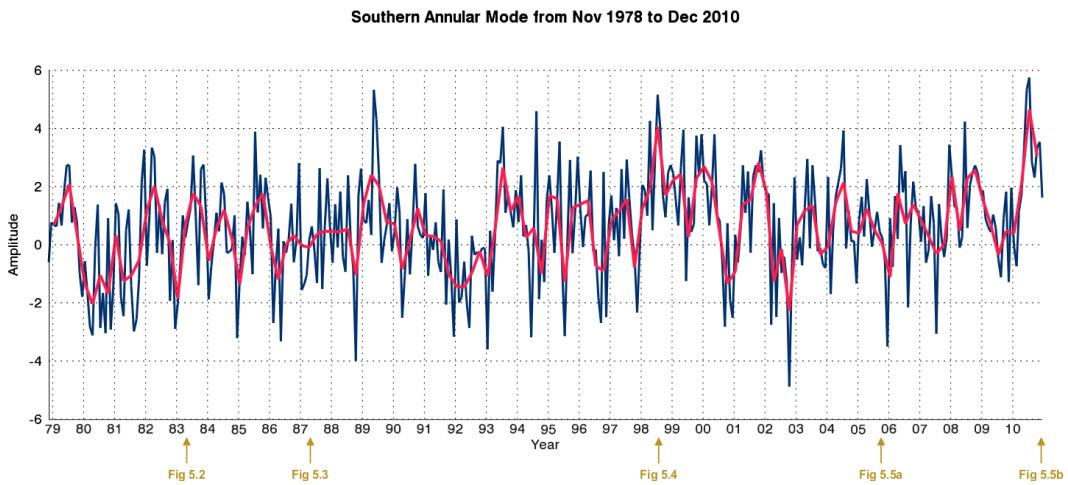

Figure 2.8: *The plot shows values of monthly SAM Index (SAMI) in blue and seasonal SAMI in red over the WACMOS period 1979-2010. Strong positive episodes occur regularly in summer season in the first half of the year (like in 1989, 1996, or 2010) and then tend to trigger a dry event in southern Australia. This in contrast to negative events, which tend to appear in the second half of the year (like in 2003, 2006 or 2007).*

2.3 Solar Activity

Ongoing research is investigating the influence of the Sun's activity on the Earth's climate. The Sun is the main driver of atmospheric and oceanic processes and facilitates the energy for almost every biological activity on the planet.

Based on the correlation between solar activity and meteorological parameters, recent research repeatedly suggested influence of solar irradiance variations on the Earth's climate (Gray et al., 2010). Recently, (Ineson et al., 2011) found that low solar activity drives cold winters in northern Europe and the United States, and mild winters over southern Europe and Canada, with little direct change in globally averaged temperature.

Our Sun undergoes cyclic and aperiodic variations in characteristics of its emitted energy. This is due to several processes occurring mostly in the Sun's convection zone, surface (photosphere), and atmosphere. The so-called *solar activity* governs the space weather[7] and is the reason for phenomena like northern lights and sunspots. Adjacent toaperiodic fluctuations of solar activity, there is a major cyclic variation and this is termed *solar cycle*. It describes the oscillation of the amount of solar irradiation experienced on Earth with a period of about 11 years.

[7] condition in the Sun system concerning cosmic and solar EM and particle radiation (e.g. sun winds = stream of ions)

The Sun is a star and fusions hydrogen to helium and consequently frees enormous amount of energy. Inside, unbalance of heat induces convective fluxes and causes a turbulent character of the Sun's body. These disturbances are of electric as well as magnetic nature. A complete explanation of the occurrence of *sunspots* and sun-flares (extremely bright spots and mass eruptions) is not found yet and there are several hypothesis. But there is an agreement on an interaction of magnetic flux and electric conduction during turbulent flow (Benestad, 2006). As a result, the radiation emitted from the Sun and received at the Earth varies in terms of amplitude and spectral composition. Strong pulses of solar winds occasionally disturb electronic systems on-board satellites or cause northern lights, which is an excitation of particles in the ionosphere.

Sunspots stem from local magnetic disturbances[8] and appear as dark patches of different size on the Sun's apparent surface and they are observable from Earth via telescopes. The count is the simplest measure for solar activity. The ancient Greeks were the first who recorded the number of sunspots. Indeed, scientists traced the development of sunspot count throughout the last centuries and thus provide an extraordinary long time series.

Since the 1950s, two "official" sunspot counts established: The Zurich (or Wolf) and the American Number. Both determine the sunspot number from visual observations with optical instruments and they correlate well. Here, the Wolf Number is introduced, which was invented by Rudolf Wolf in Zurich in 1849. He formulated following equation as an estimate for sunspot number R_z, which is an index:

$$R_z = k(10g + f) \tag{2.5}$$

The number f is the total number of (physical) sunspots, g is the number of sunspot groups, which are agglomerated, not exactly numbered, sunspots and k is a scaling factor depending on the observing method (Benestad, 2006).

The counting of sunspots via a telescope or refractor by an human operator needs interpretation and thus is not perfectly reproducible. Radiometric measurements of the incoming solar radiation offers an alternative method to observe solar activity. Various manifestations of solar activity are driven by the total amount of magnetic flux emerging through the photosphere into the (above) chromosphere and corona.

Solar Radio Flux F10.7 The *Solar Radio Flux* or *10.7cm Solar Flux (F10.7)* is a measurement of the integrated emission at 10.7 cm wavelength from all sources present on the sun disc. This is related to the amount of magnetic flux as well as to the sunspot count. Nowadays, the Solar Radio Flux is commonly used to document the solar cycle because it is an excellent indicator of

[8] induced by the *Zeeman effect*

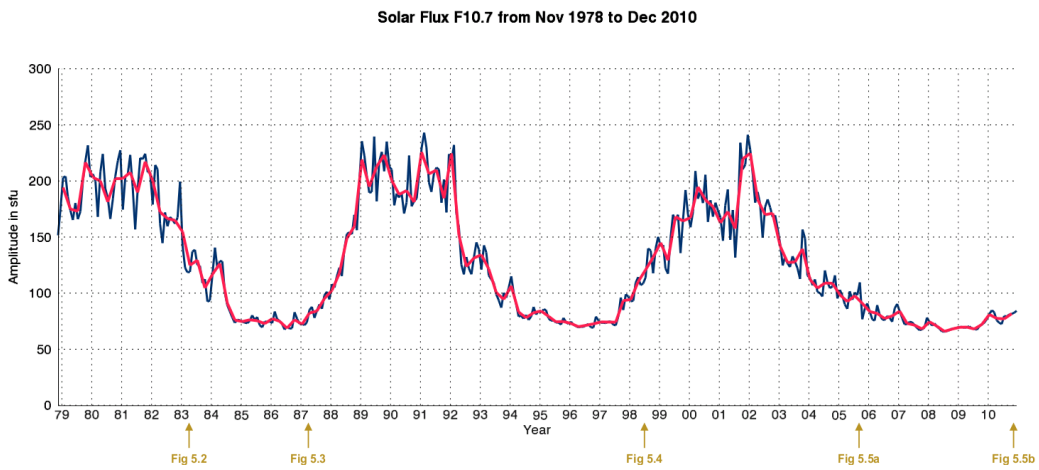

Figure 2.9: *The plot shows values of Solar Fluc F10.7 monthly in blue and seasonal in red over the WACMOS period 1979-2010. The 11-year Solar Cycle is clearly obvious and also other cyclic components of solar variation can be detected. The ongoing cycle caused some sensation due to a prolonged state of minimum activity in 2008-10.*

overall sun activity. But it is not only used for parametrisation of solar activity, also many physical models of the upper atmosphere use the F10.7 as input to determine atmospheric densities in the upper layers.

The 10.7 centimeter solar radio flux (F10.7) is the amount of radio emission from the Sun at 2.8 GHz (10.7 cm) received at the Earth and is given in $10^{-22}\,\mathrm{W\,m^{-2}\,Hz^{-1}}$. This unit is a multitude of a *Jansky (Js)* but it more commonly named *solar flux unit (sfu)*:

$$1\,\mathrm{sfu} = 10^4\,\mathrm{Js} = 10^{-22}\,\mathrm{W\,m^{-2}\,Hz^{-1}} \tag{2.6}$$

F10.7 is provided by the Dominion Radio Astrophysical Observatory on a daily basis since 1947. It shows minimum values of about 65 sfu, when the Sun does not show any sunspots and maximum values of about 300 sfu.

The Australian Bureau of Meteorology (BOM) suggests following conversions between F10.7 and sunspot number, where F is the Solar Radio Flux and S is the Wolf number.

$$S = 1.61(F - 67.0) - (0.0733(F - 67.0))^2 + (0.0240(F - 67.0))^3 \tag{2.7a}$$

$$F = 67.0 + 0.572S + (0.0575S)^2 - (0.0209S)^3 \tag{2.7b}$$

2.4 The Climate of Australia

This section gives a brief summary of the geographic, climatic and hydrological characteristics of the Australian content.

The Australian continent has a tropical climate in the north and a warm-temperate in the south. There can be further distinguished between in dry inner country and the wet coastal areas, where the northern shores are influenced by monsoon rains. At the eastern coast, a humid climate is prevailing and the south-western coastline enjoys Mediterranean climate (please see Figure 2.10). All climatic conditions are dominated by the annual latitudinal movement of the Inner Tropical Convergence Zone (ITCZ). Because of Australia's homogeneous topography there are no abrupt changes in climate. Concerning temperature, there is a distinctive trend from north-north-west to south-south-east. Due to this lack of geographical features affecting climate, like high mountains, the main factor on temperature is the latitude (Johnson, 2004).

Large parts of Australia can be identified as semi-arid. In general, semiarid environments are found in subtropical zones where the potential evaporation exceeds the received precipitation for several months per year. They undergo a seasonal precipitation regime and high dynamics of soil moisture and water surfaces are typical. These regions are characterised by low and restricted precipitation because moisture bearing winds cannot reach and cool down such regions. Also, zones of high pressure may prevent entry of winds, resulting in absence of rainfall in these areas. Semiarid areas are classified according to the amount of received rainfall, duration of the wet period, and the dominant vegetation. The wet period is the period during which rainfall is higher than evapotranspiration and lasts usually for a period of three to four months per year. The vegetative cover is characterised mainly by shrubs, scrubs and grass. In these regions, potential evapotranspiration is consistently high while actual evapotranspiration is sensitive to soil moisture availability (Legates et al., 2010). So, actual evapotranspiration falls short of potential evapotranspiration because of limited local moisture.

Change in Climate As the the *Intergovernmental Panel on Climate Change (IPCC)* stated in the climate report of 2007 ((Solomon et al., 2007), recent climate change projections predict that the Australian climate is likely to warm in this century, according to the global mean warming. This development will affect the south of the continent to a lesser extent than the northern part. An increased frequency of extremely high daily temperatures and a decreased frequency of cold extremes are prognosticated. Concerning precipitation, a decrease is likely in southern Australia in the winter season. Changes in rainfall in central and northern parts of the continent are uncertain. Following the global trend, the frequency of extreme rainfall events is likely to increase,

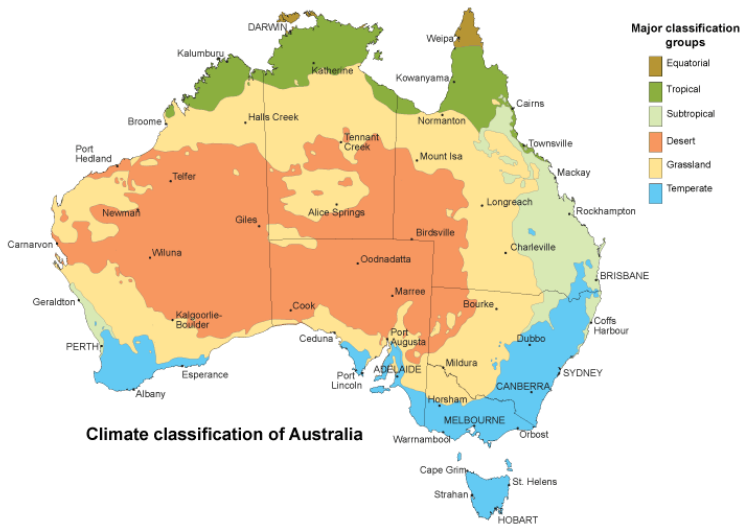

Figure 2.10: Modified Climate Classification of Australia after Köppen. Based on CLINO 1961-1990.

which escalates the risk of flooding. Nevertheless, the likeliness of drought will augment also because of the expected rise in evapotranspiration, which will be a consequence of the higher mean temperatures.

To sum up, a trend to a rougher climate with more extreme conditions is expected for the ongoing century. Keeping in mind the already extreme climatic conditions in Australia, a good understanding of hydrological processes will be of higher value more then ever before.

Hydrology The continent's hydrology is ruled by predominantly arid and semiarid climate with vast areas receiving less than 400 mm annually. In a way, all the climate zones surround the centre of Australia concentric and towards the coastlines, it is getting wetter and more moderate. In Figure 2.11 one can easily see the wet conditions in the tropic north and the subtropic north-east during summer and autumn as well as the humid conditions in the south-east throughout the year. The illustration also reflects the latitudinal shift of the high pressure zone during the year, which is related to low rainfall rates. The barren inland covers a third of the continent and has arid desert conditions with annual total precipitation below 250 mm. In summer, it is dry and hot and in winter, it is dry and warm. Evaporation and transpiration are much higher than precipitation, what charges the building of endorheic lakes (salt pans) and desert areas.

Overall, great variability of precipitation is a characteristic feature of Australia's hydrology. So, Australia is frequently subject to flooding and droughts, resulting in considerable impact on environment and economy. In general, rainfall amount decreases rapidly from the northern coasts

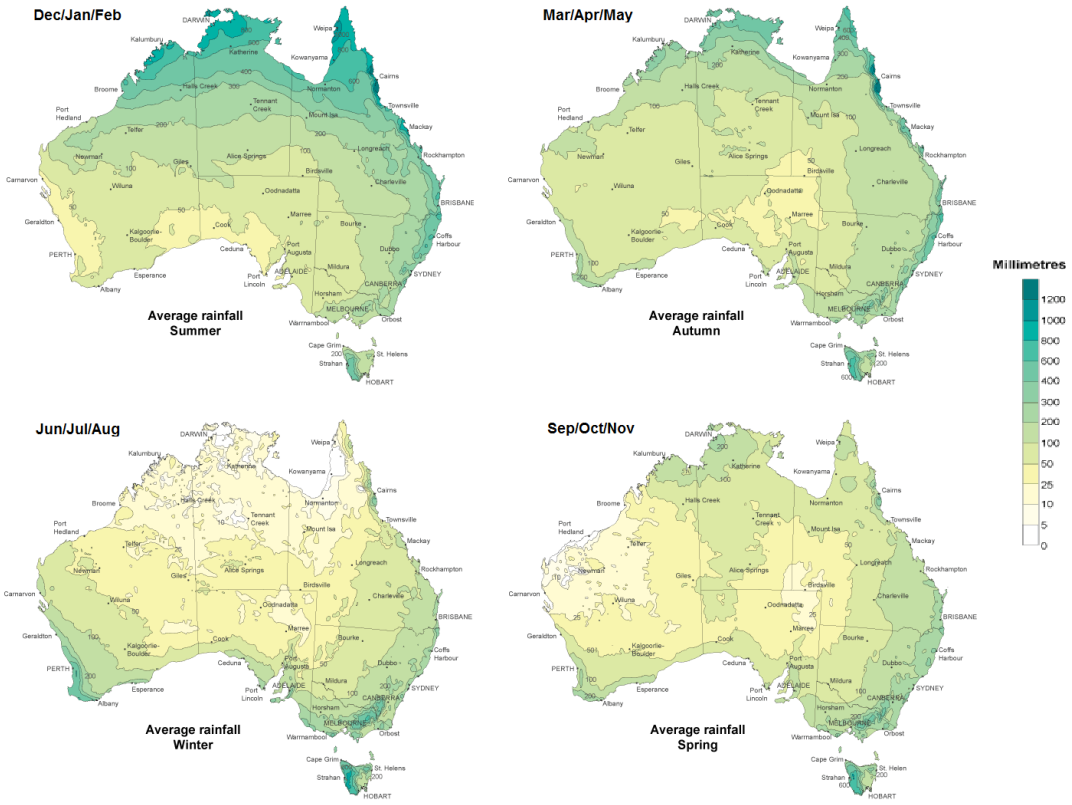

Figure 2.11: *These maps present total rainfall in millimetres per season in Australia. Based on CLINO 1961-1990. Graphics from the Australian Bureau of Meteorology.*

towards the centre. The monsoonal north is known as permanently wet and the bulk of rainfall appears in the winter months (monsoon). In the north-eastern parts (first of all Cape York Peninsula), the highest annual total rainfall is experienced with values about 4000 mm. Here, different wind systems (summer Monsoon, incidental Cyclones and winter trade winds (from seaside)) cause well distributed high rainfalls. While the north-eastern coast receives rainfall at all months, the major rain falls in south-eastern coastal areas in winter season (Johnson, 2004).

Soils Australian soils reflect the continent's age and are consequently products of environmental conditions throughout history, like climate, organisms and topography in the course of time. This means that large areas are affected by intensive weathering and salt accumulation and have various nutrient and physical limitations for vegetation. The predominant superficial colour in vast areas, especially in the west, is iron-oxide-alike-red because of the dry and oxidizing environment in Australia. Compared to the northern hemisphere, soils in Australia tend to have less organic matter and poor structure and tend to be quite clayey just below the surface, what restricts drainage and impedes root growth. They commonly contain duricrusts resulting from cementation. Limitations to productivity in agriculture have also been induced through human impacts on soils like overgrazing, over cultivation, tree clearing and irrigation. Australian agriculturally utilised soils tend to be old, salty, clayey, acidic, and to be nutritionally and organically depleted. Most are ancient, strongly weathered and infertile (Johnson, 2004; Isbell, 2002).

Chapter 3

Soil Moisture and Microwave Remote Sensing

It's a kind of magic, magic, magic

Queen

Soil Moisture is the water contained in the root zone of the soil and available for plant utilisation. Surface soil moisture makes up only 0.0012% of total water on Earth (Chow, 1988), but however, it is an important environmental variable with impact on hydrological, meteorological and climatological processes as well as on agriculture and socio-economics. Furthermore, it is a critical component in temperature, humidity and precipitation forecasts (Koster et al., 2004). Since 2008, soil moisture is listed as *Essential Climate Variable (ECV)* within the framework of the *Global Climate Observing System (GCOS)* (Wagner, 2009).

Remote Sensing of the environment aims to determine physical, chemical or biological variables on the ground, in the air or in the seas. Mostly, this is not done with direct measurements, but with indirect measures of the targets' electromagnetic (EM) properties. Thus, e.g. the temperature of the seas is not observed directly in °C, but instead the emitted electromagnetic radiation of the seas is examined. With knowledge of the *radiation laws*, one can infer the physical temperature from the emitted infrared radiation.

In general, remote sensing compromises several techniques for determination of environmental parameters that observe electromagnetic properties via radiation (EM rays or, depending on the context, EM waves) as carrier of information. Primary dependent on the frequency and consequently on the wavelength, radiation interacts with objects in a rather various way. Long waves

like radio waves interact completely different with matter than short waves like X-rays. Scientists make use of this and design systems which operate at frequencies that fit to the investigated physical processes. Since the 1960's, visible and infrared imaging sensors have been employed for observing land surface parameters, such as snow cover, surface water areas, land use and surface temperature (Schmugge, 1985). A major drawback of these instruments is their dependence on atmospheric conditions. Clouds, water vapour and aerosols can easily disturb the signals and therefore impede the observation (de Jeu et al., 2008). Instead, microwaves (Section 3.2) do not suffer from these obstacles and show many properties making them very valuable for remote sensing.

3.1 Water Cycle and Soil Moisture

The water cycle is one of the most important processes on Earth as it sustains life and controls weather and climate. Water is a fundamental resource affecting every part of human life, social systems and the environment. It is the main driver of all biological activities, weather patterns and many geomorphological processes. But however, water availability is also strongly dependent on local climate and geographical features and consequently varies considerably around the globe's land masses. Especially in regions without sufficient natural water, effective distribution and conscious use are required. In all parts of the world, people are becoming more and more aware of the necessity of regulating and limiting water consumption. Economic expansion and population growth put additional pressure on water resources by intensified agriculture, irrigation and mechanised harvest methods. Also, an expanding industrial sector consumes large amounts of water to satisfy its ever increasing demands.

Located at the boundary of solid Earth to atmosphere, soil moisture plays an important role in our planet's water, energy and carbon cycle. It governs the segregation of precipitation into seepage and runoff (Chow, 1988), the partitioning of incoming radiation into sensible and latent heat fluxes and forms the basis of any vegetation. Variations in heat fluxes are affected by spatial and temporal dynamics in soil moisture and that alters the near-surface air temperature and humidity. This can change local precipitation which, in turn, impacts on soil moisture (Legates et al., 2010). Overall, soil moisture is a measure of several climatic and hydrological conditions and a contributing factor to these conditions. Soil moisture is a strong indicator of previous weather conditions and of the ecosystem state (Liu et al., 2009). The interactions between climatological variables and soil moisture are still the object of research in various scientific disciplines. However, the strong relations with precipitation, energy fluxes and soil composition make soil moisture also a mirror of regional water availability.

3.1.1 Soil Moisture Determination

To begin with, soil moisture content can be defined in different ways:

- The *gravimetric water content* is the ratio of the mass of liquid phase to total soil mass: $\frac{m_W}{m_T}$ in $\mathrm{kg\,kg^{-1}} > 0$
- The *volumetric water content* is the ratio of the volume of liquid phase to total soil volume: $\frac{V_W}{V_T}$ in $\mathrm{m^3\,m^{-3}} > 0$
- The *degree of saturation* is the ratio of volume of liquid phase and the soil's pore volume: $\frac{V_W}{V_P}$ with values between $0 > \% > 100$

There are several techniques to measure the amount of soil moisture. Laboratory methods like thermal or chemical tests on soil conditions require samples. These methods are very precise but bear the disadvantage that samples must be obtained manually.

Another strategy to gain soil moisture information is the establishment of an in-situ-network. Soil moisture can be measured accurately in the field by means of various in-situ measurement techniques (Walker et al., 2004). Here, a number of electric devices are installed on the ground and measure soil moisture in regular means by investigating the conductivity of the soil, which is a function of the water content. However, technical developments of the last decades spawned new tools to observe soil moisture:

Since in-situ measurements or laboratory examination of soil moisture are expensive on the long run and are poorly distributed (Robock et al., 2000), large-scale-monitoring prefers the utilisation of remote sensing. Spaceborne microwave sensors have proven ability to determine soil moisture on a global scale and to deliver important data for hydrologists and meteorologists. The backscattering coefficient, an electrical material property of the Earth's ground, is linked to the water saturation of the soil. Microwave sensors have shown high sensitivity to this variable. Recently, significant progress due to advances in sensor technology and new algorithmic approaches has been achieved. (Wagner et al., 2003) generated a first global soil moisture dataset derived from the scatterometers onboard ERS-1 and ERS-2, which are operating at 5.3 GHz in the C-band.

On this background, remote sensing offers a powerful technique to measure soil moisture virtually everywhere on the planet without high time consumption. The use of microwave sensors mounted on satellites allows investigating the soil moisture conditions of large areas on the Earth's surface in proper spatial and temporal scales.

Scale One key question on monitoring soil moisture is the sample rate in space and time. How large is the area represented by a measurement and what is the time duration between two measurements? Since droughts and (the more dynamic) floods are processes that propagate in space and time, these parameters strongly determine the quality and usability of soil moisture data. Droughts are slow-onset-events and therefore do not demand high temporal resolution during monitoring. On the contrary, flood observation requires a much higher temporal sample rate to comprehend the course of inundations. In the domain of spaceborne remote sensing, spatial and temporal resolution are inversely related. On a satellite as carrier, coarse resolution radar systems like radiometers or scatterometers offer a far better temporal coverage than high resolutions sensors since they are able to scan the globe in broad swaths. So, one certain point at the ground can be measured relatively often what facilitates high temporal sampling. As an outlook, active microwave instruments like *synthetic aperture radars (SAR)* use sophisticated signal processing and achieve a higher spatial resolution at the cost of the repetition rate of measurements. The choice of a system that is addressed to a distinct application is bound to these considerations.

3.2 Microwave Remote Sensing

Microwaves EM light with a wavelength between 1 mm and 1 m is called the microwave part of the electromagnetic spectrum. This metric range is equivalent to the spectral range from 300 GHz to 300 MHz. The microwave spectrum lies between infrared spectrum and radio waves and is commonly divided into bands. In the scientific community, the preferentially used naming convention is presented in Figure 3.1.

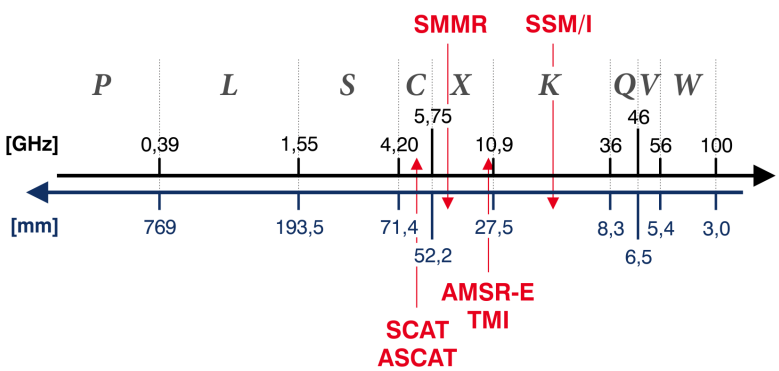

Figure 3.1: The microwave spectrum and the band divisions are plotted in a logarithmic scale. For the six sensors used in the WACMOS soil moisture product (see Section 4.1), the centre frequencies of the employed channels are indicated.

Maxwell's Equations Today, microwaves have much utilisation in a broad field of technology like wireless communication, broadcasting, microwave ovens, navigation, radars and in particular sensor systems. Microwave rays show some characteristics that make them useful for remote sensing in general but especially for observation of hydrological parameters. It should be noted that the use of microwaves for remote sensing affairs is based on the simple fact that they are *different* from "ordinary" visible or infrared light. Since physical objects interact differently with different kinds of EM radiation, one can infer supplemental information.

All theory on EM waves is based on the *Maxwell's equations* that explain electromagnetic phenomena in a very fundamental way:

$$\nabla \cdot \mathbf{E} = \frac{\rho}{\varepsilon} \qquad \nabla \cdot \mathbf{B} = 0 \tag{3.1a}$$

$$\nabla \times \mathbf{E} = -\frac{\partial}{\partial t}\mathbf{B} \qquad \nabla \times \mathbf{B} = \mu \mathbf{J} + \mu\varepsilon\frac{\partial}{\partial t}\mathbf{E} \tag{3.1b}$$

The equations are presented in its differential form with ∇ as the Nabla-operator, $\mathbf{E}$ as the electric field vector, $\mathbf{B}$ as magnetic field vector, ρ as electric charge and $\mathbf{J}$ as electric current. The constants μ and ε denote the magnetic permeability and electric permittivity and describe magnetic and electric properties of a material. The Maxwell equations postulate that EM fields propagate through space as if they are waves and therefore they describe the propagation of all EM waves. Furthermore, an oscillating electric field induces an oscillating magnetic field which in turn induces an electric field (Woodhouse, 2006). The planar and orthogonal waves $\mathbf{E_x}$ and $\mathbf{B_y}$ that propagate in z-direction are general solutions of the above mentioned equations and can be written as

$$\mathbf{E}_x = E_0 \cos(kz - \omega t) = E_0 e^{i(kz-\omega t)} \tag{3.2a}$$

$$\mathbf{B}_y = \frac{E_0}{c}\cos(kz - \omega t) = \frac{E_0}{c} e^{i(kz-\omega t)} \tag{3.2b}$$

in which E_0 is maximum amplitude in time dependence of t; $k = \frac{2\pi}{\lambda}$ is the wave number with λ as wavelength, and $\omega = 2\pi f$ is the angular frequency with f as (time) frequency.

The theory also connects EM radiation to the nature of light since the speed of light in vacuum has been found to be

$$c = \frac{1}{\sqrt{\mu_0 \varepsilon_0}} = \frac{\omega}{k} \tag{3.3}$$

in which μ_0 is the *permeability of free space* and ε_0 is the *permittivity of free space*. In matter, the

permittivity ε is usually higher and can be split into

$$\varepsilon = \varepsilon_r \varepsilon_0 \tag{3.4}$$

with ε_r as *relative permittivity*, which is *the* dielectric property observed with remote sensors (see Figure 3.2) and can be further split into a real and an imaginary part

$$\varepsilon_r = \varepsilon_r' - i\varepsilon_r'' \tag{3.5}$$

The expression ε_r' is widely known as *dielectric constant*.

3.2.1 Emission and Scattering

Every body is permanently sending out EM radiation stemming from their moving atoms and molecules. At the same time, the body is hit by EM radiation and latter is either totally transmitted (no interaction), reflected (changed in direction = scattered) or absorbed (energy is ingested) or, most likely, fractions of these three mechanisms with respect to the frequency. There is plenty of literature elaborating the theory, but just to mention a few, in (Ulaby et al., 1981; Woodhouse, 2006) the principles can be found. In the framework of this study, only microwave emission and scattering of land surface parameters are briefly discussed.

Emission Concerning emission, *Planck's law* is a fundamental concept. It describes the relationship of the physical temperature of a blackbody (an ideal radiator that totally absorbs and re-emits all incident energy) and its emitted radiation and reads as

$$B_f(T) = \frac{2hf^3}{c^2} \frac{1}{e^{\frac{hf}{kT}} - 1} \tag{3.6}$$

Here, $B_f(T)$ is the *spectral brightness* and represents the intensity of the blackbody's radiation per unit frequency range f per steradian[1] in $\mathrm{W\,m^{-2}\,sr^{-1}\,Hz^{-1}}$; h is the Planck's constant ($6.626\,069\,57 \times 10^{-34}\,\mathrm{J\,s}$); c is the speed of light ($299\,792\,458\,\mathrm{m\,s^{-1}}$) and k is the Boltzmann's constant ($1.380\,648\,8 \times 10^{-23}\,\mathrm{J\,K^{-1}}$). The important statement of this law is that the temperature of a body rules the intensity of emission at a distinct frequency. B_f is sometimes considered as surface brightness meaning the energy flow across a unit area per unit frequency and per steradian.

[1] the cubic analogue to the planar angle

The assumption of regarding microwaves allows to simplify Equation (3.6) since their frequencies are below the *Rayleigh-Jeans limit*, so that $hf << kt$. Then the relationship turns out to be linear as

$$B_f(T) \approx \frac{2f^2k}{c^2}T. \tag{3.7}$$

As a result, the *Rayleigh-Jeans equivalent brightness temperature* $T_B(f)$ or *microwave brightness temperature*, which is a quantity measured by spaceborne microwave instruments, can be derived:

$$T_B(f) = \frac{c^2}{2f^2k}B_f = \frac{\lambda^2}{2k}B_f \tag{3.8}$$

The brightness temperature has Kelvin as unit and is connected to the physical temperature like

$$T_B(f) = \varepsilon T \tag{3.9}$$

The term *emissivity*[2] ε depicts this property and ranges from 0 to 1. Contrary to a blackbody, real objects are "greybodies" with a lesser potential for emitting radiation. Similarly, *reflectivity* ρ describes the body's ability to reflect radiation and both quantities are connected for opaque (not transmissive) objects, for a certain wavelength λ, with *Kirchhoff's Radiation Law*:

$$\varepsilon_\lambda + \rho_\lambda = 1 \tag{3.10}$$

It says that emission and reflection are complementary, yielding that surfaces that are good scatters are weak emitters, and vice versa (Woodhouse, 2006). Both emission and scattering properties of the Earth's surface mainly depend on its geometric structure and the dielectric properties. Non-conductive objects are known as *dielectric* and in the domain of remote sensing this type of matter is observed in most cases. Regarding remote sensing, the important point here is that same physical phenomena on the Earth surface affect both emission and scattering. Applied on soil moisture, this means a higher water content will decrease emission and increase scattering.

Scattering Additionally to dielectric properties, the geometry and relative size of the target to the wavelength govern scattering. *Back*scattering is then also dependent on the relative viewing angle and on the size of the target, including its relative roughness. In (Woodhouse, 2006) these principles are well explained. Here, the backscattered signal of an active microwave instrument is discussed.

[2] not to confuse with electric permittivity

For an emitted and backscattered wave, the energy transfer originating from an antenna through transmission, followed by scattering at the target and reception of the transmitted signal back at the antenna, is described by the *radar equation*. It determines what proportion of the transmitted energy is scattered from the target back to the antenna (Woodhouse, 2006). In the case in which the same antenna transmits (indexed with 't') and receives (indexed with 'r'), the radar equation can be written as

$$P_r = \frac{P_t G_t A_r}{(4\pi)^2 r^4} \sigma \tag{3.11}$$

in which P_r is total power received at the instrument in Watt; P_t is total power transmitted; G_t is the directional sensitivity of the antenna (the antenna transmitting gain); A_r is the effective receiving area of the antenna; r is the range (the distance) between antenna and target and σ is the radar cross section for the observed target. The radar cross section is a collective term for interaction of the signal with the target and varies with the target's geometry and dielectric properties. When normalised by area, one talks about normalised cross section. This is the *backscatter coefficient (σ^0)*, a natural parameter of the target independent from the used radar system:

$$\sigma^0 = \frac{d\sigma}{dA} \tag{3.12}$$

This parameter as fraction of differential scattering cross section and differential unit area given in $m^2\,m^{-2}$ is an excellent quantity for describing the backscatter behaviour of an object and is *the* quantity derived from observations of active microwave systems. The radar equation (3.11) for an extensive area yields then to

$$P_r = \frac{\lambda^2}{(4\pi)^3} \int_A \frac{P_t G_t^2}{r^4} \sigma^0 dA \tag{3.13}$$

and reforming leads to

$$\sigma^0 = \frac{\sigma}{A} = P_r \frac{(4\pi)^3 r^4}{P_t G_t^2 \lambda^2 A} \tag{3.14}$$

which is commonly expressed on a logarithmic scale in decibels due to its high dynamic range:

$$\sigma^0_{dB} = 10 \log \sigma^0 \tag{3.15}$$

As mentioned above, dielectric properties of matter have impact on backscatter. Material characterised by a high dielectric constant (permittivity) reflects high intensity backscatter. Examples that can be given here are any kind of metals and wet soil. The wet soil has a distinct higher backscatter then dry soil. Also, vegetation affects the backscatter intensity mainly because of the

water vegetation content that changes the dielectric properties and vegetation structure introducing volume scattering (scattering and emitting in all directions). The occurrence of volume scattering is increasing with the amount of small particles (leaves, corns etc.) and is pronounced especially when the small particles approach the size of the wavelength. Very simply said, the backscatter increases with biomass density up to some saturation level. Additionally, corner reflectors (two or better three planes orthogonal to each other) are outstandingly good backscatters. They reverse the direction of incoming beams with 180° and so nearly the complete emitted energy is received by antenna. This causes very high backscatter in anthropogenic areas with many corners and planes, for example in cities.

3.2.2 Properties of Microwaves

The wavelength is an essential quality for remote sensing scientists. For example, travel through the dispersive[3] ionosphere as well as attenuation and transmission in atmosphere layers below are governed by the wavelength of the radiation. Most physical processes involving waves are dependent on the wavelength. The main incentives for using microwaves for Earth observation and related basic radiative principles are shortly introduced:

Atmosphere Transmission One very important reason for the usage of microwaves in spaceborne remote sensing is their capability of travelling through clouds without big energy loss. This clearly distinguishes them from visible or infrared light, which obviously cannot penetrate trough clouds. This advantage holds also for rain clouds, which do not interfere with lower-frequency microwaves[4].

Daylight Independence Optical sensors can only deliver meaningful information if the target is exposed to sunlight illumination. Consequently, during night, no observation can be done and information is missed out. Microwave sensors, either passive or active, do not require sunlight. Actually, active microwave systems like *radars* illuminate their targets themselves.

Volume Penetration Microwave beams are able to interact to some extent with volumes of targets since their waves are longer and are not reflected immediately at the surface. Thus, information about inner conditions of vegetation or soils, for example, can be gained. As a rule

[3] Dispersion is dependency on frequency; in optics it is more concretely the frequency-dependency of the wave's phase velocity (Stöcker, 2004)

[4] higher-frequency microwaves do interfere with rain drops and therefore are applied in *weather radars*

of thumb, the longer the wavelength, the deeper the radiation penetrates into plants or soils, respectively. On the contrary, optical waves only interact with surfaces and tell us about the visible colour and brightness. As later explained in more detail, microwaves allow to infer knowledge about the water content of plants and soils. It is also worth mentioning that the lower the matter's imaginary part of the permittivity ε'', the deeper the penetration of EM waves.

Vegetational Effects When observed from above the canopy, vegetation affects the microwave emission in two ways: Firstly, vegetation absorbs or scatters the radiation emitted from the soil. Secondly, the vegetation also emits its own radiation. These two effects tend to counter each other, but however, the observed soil emission decreases with increased vegetation while emission from the vegetation increases (de Jeu et al., 2008). Under a sufficiently dense canopy, the emitted soil radiation will become totally masked, and the observed emissivity will be mostly due to the vegetation. The magnitude of the absorption depends upon the wavelength and the water content of the vegetation. The most frequently used wavelengths for soil moisture sensing are in the L, C- and X-bands, with L-band sensors having greater penetration of vegetation. Generally, observations at all frequencies are subject to scattering and absorption and require some correction if the data are to be used for soil moisture retrieval. Higher frequency bands are more vulnerable to vegetation influences.

Sensitivity to Soil Moisture The theoretical basis for measuring soil moisture with microwave sensors lies in the large contrast between the dielectric properties of liquid water and dry soil material at these frequencies as illustrated in Figure 3.2. As water is added to the soil, the dielectric constant ε' as well as ε'' increase since there are more water molecules that can rotate freely and thus can be excited by radiation (Woodhouse, 2006). This physical mechanism is the basis of microwave remote sensing of soil moisture: Water molecules are dipoles and respond strongly to applied EM fields (or waves). As a consequence, water has a very high dielectric constant at common temperatures. In contrast, dry soils show very little dielectric constant and this yields a high contrast in dielectric properties between dry and wet soils since water in the soil matrix eminently increases the effective dielectric constant (Ulaby et al., 1986; Woodhouse, 2006). The critical relaxation frequency, at which particles are no longer able to follow the applied oscillating fields and act as harmonic oscillators and thus permittivity decreases, is for H_2O molecules at 0 °C around 9 GHz and at at 20 °C around 17 GHz. Microwave remote sensing instruments that operate below these frequencies show great potential for the retrieval of soil moisture (Pathe et al., 2009). The measurements are, however, also affected by vegetation, surface roughness, and other land surface parameters. Accordingly, sensor characteristics and the soil moisture retrieval

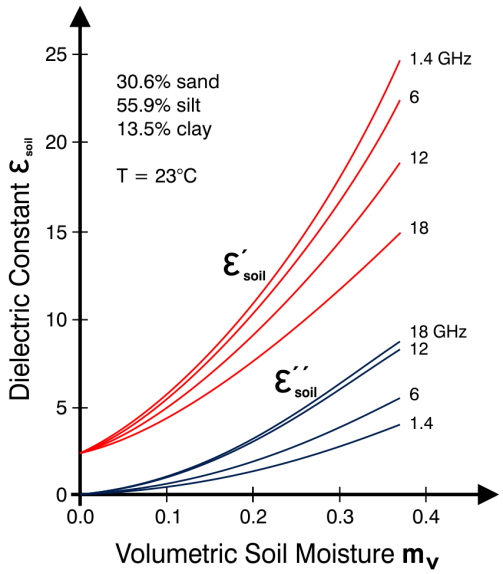

Figure 3.2: *The graph shows the relationship between soil moisture content and permittivity of a specific soil composition at 23°. For four microwave frequencies, the real part ε' and the imaginary part ε'' of the permittivity are displayed. Pure water shows values for ε' about 80 at* 1 *GHz. Graphic reproduced from (Ulaby et al., 1986).*

method must be appropriately chosen in order to obtain practicable results.

3.3 Soil Moisture from Spaceborne Microwave Systems

In the domain of Earth-observation, microwave systems are mostly mounted on *Low Earth Orbit (LEO)* satellites, which are below 1000 km altitude. In microwave remote sensing one distinguishes *active* and *passive* techniques. While passive microwave radiometers record naturally emitted radiation, active microwave sensors generate and transmit electromagnetic waves and record the backscattered radiation. The latter are often referred to as radar, which stands for radio detection and ranging. For the former, the radiation source is the target itself; it senses the naturally, and as a consequence incoherent, emitted energy originating from self-emission. An active sensor illuminates the target area, collects the reflected energy and finally gains information from this echo.

Both emission and scattering of microwaves are strictly governed by the dielectric constant. Hence, passive and active microwave instruments are highly sensitive to soil moisture (Woodhouse, 2006).

3.3.1 Radiometer

Passive systems like radiometers record the *brightness temperature* (see Section 3.2.1) of the Earth's surface, which is a measure for the amount of emitted radiation. Contrary to an active system, a radiometer receives incoherent radiation that extends over the entire EM spectrum. This increases the likeliness of noise polluting the signal. Therefore, the radiometric sensitivity[5] is one of the most important characteristics of a radiometer instrument. In typical remote sensing situations observing land surfaces, the physical temperature (and consequently the microwave brightness temperature) is relatively uniform across the observed area, or is determined otherwise. Thus, the actual measured parameter is the emissivity ε of the targets on the surface. Exemplary radiometer systems are described in Section 4.1.

3.3.2 Scatterometer

A spaceborne scatterometer is an active microwave system that transmits EM pulses towards the Earth and measures the backscattered energy. The received pulses are nearly phase-coherent and monochromatic, meaning consisting of only one or few wavelengths with a fix phase relationship.

Generally, *radars (Radio Detection and Ranging)* send out microwave radiation and receive its echo to determine distance, angle and furthermore velocity of objects by measuring the time delay of pulses and their frequency shift (due to the Doppler Effect). The development of radar technology dates back to World War II in order to detect enemy planes and ships far away and to improve weather forecasts. Nowadays, the use of radars is versatile: Air surveillance, navigation, military, weather monitoring and so on. Elementary parts are the transmitter, the antenna (mostly used for both transmission and for reception), the receiver, and the data handling equipment. The received intensity has been discussed already in Section 3.2.1, but the actual output of an scatterometer is the backscatter coefficient σ^0 of objects on the Earth's surface. Again, representatives systems are described in Section 4.1.

3.3.3 Soil Moisture Retrieval

Both emission and scattering properties of soil are strongly influenced by the soil's permittivity and consequently both passive and active microwave systems are suitable for soil moisture measuring (de Jeu et al., 2008; Woodhouse, 2006). For retrieving soil moisture it is necessary to

[5] the smallest detectable change in temperature brightness

have models that are capable of accounting for vegetation and surface roughness effects on the microwave signal and then convert accordingly the received intensity to SSM values. Again, it should be noted, that shorter a wavelength causes inferior performance due to vegetation scattering and lesser penetration depth.

Passive systems measure the microwave brightness temperature and derive indirectly the emissivity, which then is ingested in a radiative model. Data on the roughness, texture and other parameter of the observed area is necessary ancillary information. As examples, the sensors AMSR-E from NASA and SMOS from ESA are mentioned. Please see the next section 4.1 for more explanation.

Active instruments measure the backscattered intensity, which is a function of roughness, incidence angle and dielectric properties of the surface. Again, vegetation and other influences contribute to the signal, which is used to determine the backscatter coefficient. The latter is almost linearly related to soil moisture content and therefore target of SSM scatterometer missions. Prominent active microwave sensors are SCAT on ERS 1/2 from ESA or from the younger generation ASCAT on MetOp from EUMETSAT.

Chapter 4

Data and Methods

It is a capital mistake to theorise before one has data.

Arthur Conan Doyle

4.1 WACMOS Soil Moisture

ESA's Water Cycle Multimission Observation Strategy is a project cooperation of five scientific institutes. The overall aim of the project is to improve estimates of hydrological variables trough combined use of multiple sensors. In the focus are the climate variables evapotranspiration, cloud cover, water vapour and soil moisture. In order to understand climate, weather forecast and disaster predication, satellite-based monitoring-data of these variables are comprised in the framework of WACMOS.

Concerning soil moisture, the WACMOS surface soil moisture data set is the first multi-decadal database with over 30 years of observation, what allows analysing long-term variations of soil moisture. The database enables analysing the spatiotemporal behaviour of the Earth's soil moisture dating back to 1978 (Liu et al., 2009). Further, the data is built up from different types of microwave Earth observations systems (passive radiometers and active scatterometers) and combines the gained information in a synergistic manner. The blend of passive and active microwave satellite-based retrievals offers improved estimates of surface soil moisture at global scale (Liu et al., 2009). Overall, the WACMOS data can be characterised as a comprehensive and integrative set of soil moisture data and is therefore suitable to investigate connections to regional phenomena like climate modes. An detailed overview about SSM data generated during the WACMOS project is given in (Liu et al. (2012), in review).

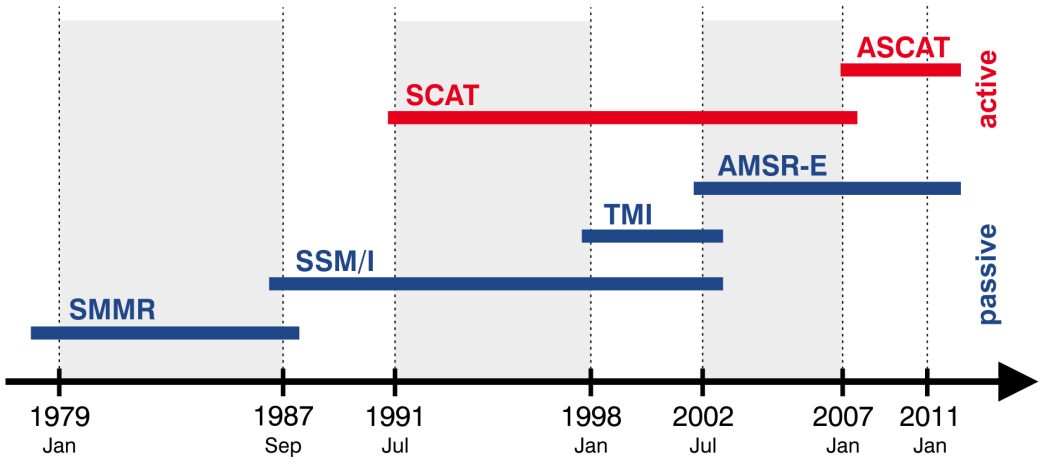

Figure 4.1: *The time graph shows when which data was used for the WACMOS soil moisture. Except for the first years, when only SMMR and SSM/I respectively data was available, minimum two sources provide data for the merging for each episode.*

A series of satellite based passive microwave sensors have been available since the late 1970s, including the *Scanning Multichannel Microwave Radiometer (SMMR)* onboard Nimbus-7 (1978-1987), the *Special Sensor Microwave Imager (SSM/I)* of the Defense Meteorological Satellite Program (since 1987), the *Tropical rainfall measuring mission Microwave Imager (TMI)* (since 1997) and the *Advanced Microwave Scanning Radiometer–Earth Observing System (AMSR-E)* onboard the Aqua satellite (since 2002). Concerning active microwave sensors, the first global satellite-observed soil moisture product was acquired by the *Scatterometers (SCAT)* onboard the European Remote Sensing satellites (ERS-1/2) since July 1991, and the *Advanced Scatterometer (ASCAT)* onboard the *Meteorological Operational satellite programme (MetOp)* which was launched in October 2006. An overview on the WACMOS sensors is given in Table 4.1 and on the temporal coverage in Figure 4.1.

		SMMR	**SSM/I**	**TMI**	**AMSR-E**	**SCAT**	**ASCAT**
		passive microwave sensors				active microwave sensors	
Platform		Nimbus 7	DMSP	TRMM	Aqua	ERS	MetOp
Time period use		1979-1987	1987-2002	1998-2002	2002-2010	1991-2007	2007-2010
Channel used	[GHz]	6.6	19.3	10.7	6.9/10.7	5.3	5.3
Spatial Resolution	[km^2]	150 × 150	69 × 43	59 × 36	76 × 44	50 × 50	25 × 25
Swath width	[km]	780	1400	780/897	1445	500	1100(550 × 2)
equat. crossing time	desc.	00:00	06:30	varies	01:30	10:30	09:30

Table 4.1: *List of sensors used for generating WACMOS soil moisture with major characteristics.*

In order to foster an enclosed product comprising the data of six sensors, a blending approach was development during the WACMOS project (Liu et al. (2012), in review). This procedure was done in three steps:

- A merging of the original passive data into one product
- A merging of the original active data into one product
- A blending of the two merged products into one final product

Passive Product The passive data was processed with the VUA[1]-NASA[2] algoritm, which is a based the Land Parameter Retrieval Model (LPRM) as described in (Owe et al., 2008). It combines various radiometer channels with different modes of polarisation and frequency and delivers simultaneously

- land surface temperature
- vegetation optical depth
- soil electric constant.

So-called volumetric soil moisture in $m^3\ m^{-3}$ is then derived from the gained soil electric constant using the model presented in (Wang and Schmugge, 1980).

Active product For the active aspect, relative soil moisture estimates are provided by the TU-Wien[3] change detection algorithm. This was originally developed for SCAT onboard ERS as by (Wagner et al., 1999) and applied with minor adaptations to succeeding ASCAT onboard MetOp by (Naeimi et al., 2009). The algorithm scales scatterometer observations between historically lowest (0% saturation) and highest (100% saturation) values and yields soil moisture m_s:

$$m_s(t) = \frac{\sigma^0(t,i) - \sigma^0_{\text{dry}}(i)}{\sigma^0(i)_{\text{wet}} - \sigma^0_{\text{dry}}(i)} \tag{4.1}$$

The measured backscatter $\sigma^0(t,i)$ at time t and under incidence angle i is set into relation with the *dry* $\sigma^0_{\text{dry}}(i)$ and *wet reference* $\sigma^0_{\text{wet}}(i)$ at the very incidence angle i. As a prerequisite, a sufficient number of previous observations is necessary to make sure that the historically driest and wettest conditions have been caught at each investigated location.

[1] Vrije Universiteit Amsterdam
[2] National Aeronautics and Space Administration
[3] Technische Universität Wien

Sensor Performance A recent report (Dorigo et al., 2010) find a generally good agreement of the passive (SMMR, SSM/I, TMI and AMSR-E) and active (SCAT and ASCAT) datasets over sparsely and moderate vegetated areas. The active product shows better performance over areas covered by moderate vegetation but they are only available since July 1991. Furthermore, the relative small number observations during the SCAT period from January 1991 to December 2006 has a relevant impact on the data density. Also the high frequency of SSM/I impacts on the data density and quality due to vegetation attenuation. AMSR-E data has been found in (Liu et al. (2012), in review) to be in good agreement with precipitation data from GPCC[4], but not so for SSM/I. Moreover, several mutual scaling and matching procedures have been applied on the initial datasets, what impairs the quality of the merged dataset as a long time-series. Concerning the radiometers, (Liu et al., 2009) detected a higher accuracy for the lower-frequency sensors SMMR (6.9 GHz) and AMSR-E (6.6 GHz) compared to SSM/I (16.9 GHz) and TRMM (10.7 GHz) and suggested as reason the less disturbing influences of vegetation.

4.2 Correlation Analyses

The questions if two or more samples of different datasets or observations have a relationship (as well as the determination of its strength) are subject of the *Correlation Analysis* (Schönwiese, 2000). Methods from this discipline provide information on the quality of the relationship of data. However, it does not say anything about causal relations(!). Therefore, some distinct statements about the quality of the correlation analysis itself should be provided together with the actual correlation values.

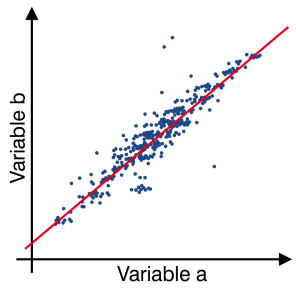

Figure 4.2: *A scatterplot of two variables with pretty high correlation.*

Correlation measures can also be deployed for evaluation of synchronism of two or more signals. Simply speaking, a question would be if $a(t)$ goes up will $b(t)$ do so as well? This is the motivation

[4]Global Precipitation Climatology Centre

why this study uses correlation measures for investigation of the relationships of different climate modes and principal components of WACMOS soil moisture over Australia. Climate modes and solar activity can be observed conveniently with special indices that form handy time series. The correlation analysis of these time series with local soil moisture or dominating modes of regional soil moisture is the main subject of this study.

A detailed explanation of correlation analysis and its derivation, tools and application can be found in various books and literature, for example in (Schönwiese, 2000; Storch and Zwiers, 2002; Wilks, 1995).

4.2.1 Spearman Rank Correlation

Very generally, the correlation coefficient of two samples X and Y is defined as

$$\rho(X,Y) = \frac{\mathrm{Cov}(X,Y)}{\sqrt{\mathrm{Var}(X)}\sqrt{\mathrm{Var}(Y)}} \tag{4.2}$$

where Cov() donates the covariance and Var() the variance of the samples. Therefore, the correlation coefficient sets the joint variance into relation with their own variances. Thus, if both vary in the same manner, the coefficient value is highly positive (synchronous) or negative (anti-synchronous). Otherwise, if their behaviour mismatch, the coefficient value is low (near to zero). Per definition, the correlation coefficient can obtain values from the interval $[-1,1]$, contrary to covariance and variance, which can obtain any value. If their is no correlation, $\rho(X,Y)$ is zero. This coefficient is called correctly *Pearson Product-Moment Correlation Coefficient*.

A very commonly used method for determination of correlation is the *Spearman Correlation Analysis*. It is very popular because it does not require assumptions about the probability distribution[5] of the samples and the fact that it also delivers feasible estimates of the relation when latter is not linear (Schönwiese, 2000)).

The *Spearman Rank Correlation Coefficient* can be seen as a special case of Pearson's coefficient. Instead of actual values, the *ranks* of the values flow into calculation. Actually, it is the Pearson's coefficient of the ranked variables and the Spearman coefficient reads as

$$\rho = \frac{\sum_i (x_i - \bar{x})(y_i - \bar{y})}{\sum_i (x_i - \bar{x})^2 \sum_i (y_i - \bar{y})^2}. \tag{4.3}$$

[5] it is so-called non-parametric

where x_i, y_i and their means $\bar{x}, \bar{y}$ do not donate for the values of the samples but for the ranks (the ordered position) of the values of the samples.

In the absence of ties (no same values with consequently same rank), this simpler formulation works and should demonstrate the simple but meaningful kernel of the Spearman coefficient (from Schönwiese (2000)):

$$\rho = 1 - \frac{6 \sum^i D_i^2}{n^3 - n}. \tag{4.4}$$

Here, D_i donates for the difference in ranks $d_i = x_i - y_i$ and n is the number of observation in each sample.

The significance of a non-zero value of ρ can be tested by computing the test quantity

$$t = \rho \sqrt{\frac{N-2}{1-\rho^2}} \tag{4.5}$$

which is distributed approximately as Student's distribution with $N - 2$ degrees of freedom.

4.3 Empirical Orthogonal Functions

This section presents a statistical method called *Empirical Orthogonal Function (EOF) Analysis* or *Principal Component Analysis (PCA)*[6]. Both terms describe the same set of procedures but their naming depends on the scientific discipline. The subject is extremely interdisciplinary, and each field has its own nomenclature, habits and notation. EOF analysis is a widely used statistical technique in atmospheric and earth sciences. It was firstly introduced into these disciplines by (Lorenz, 1956). Lorenz also stated that climate is considered as the long term statistics of weather, and climate variations are the result of exceedingly complex nonlinear interactions between very many degrees of freedom or modes (Lorenz, 1970). Both, weather and climate, are characterised by non-linearity and high dimensionality. Consequently, a challenging task is to find ways to reduce the dimensionality of the system to a few modes if possible (Hannachi et al., 2007).

The goal of the EOF technique is to derive the dominant patterns (the dominant *modes)* of variability from a statistical field, which is considered as a random vector indexed by location in space (Storch and Zwiers, 2002). The purpose of EOF analysis is the reduction (the compression) of a dataset containing a large number of variables to a smaller, handy dataset consisting of fewer new variables. Nevertheless, the new dataset should contain a large fraction of the variability (the variance) contained in the original dataset. This is exploited especially in geophysical sciences, since

[6] in German it is mostly known as *Hauptkomponentenanalyse*

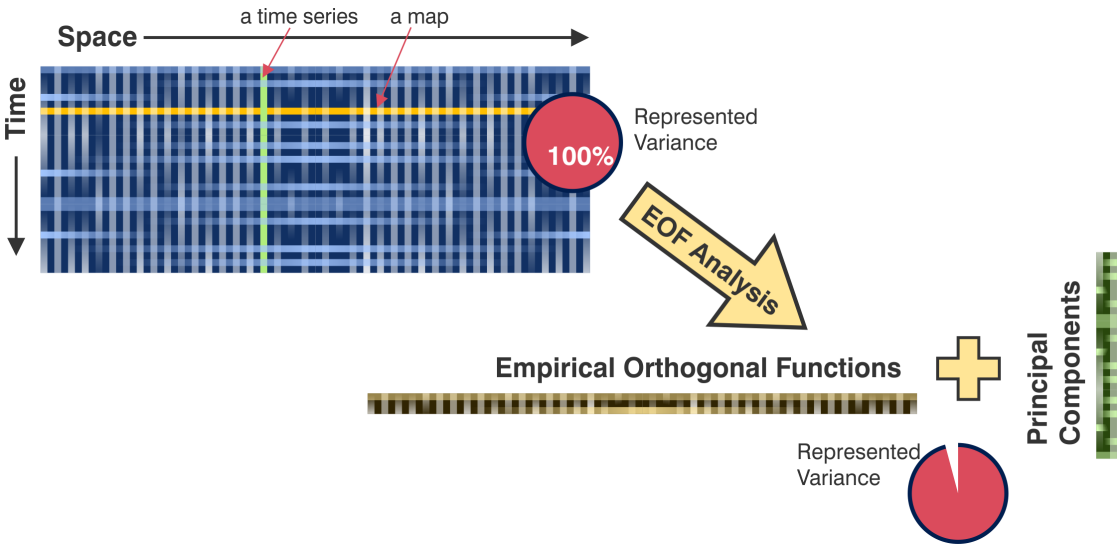

Figure 4.3: *This scheme shows the main idea of the EOF analysis.*

atmospheric and environmental fields exhibit many large correlations among their variables and the resulting *principal components* build an uncorrelated set of functions representing the data (Wilks, 1995).

The main idea of the EOF analysis is illustrated in Figure 4.3. It is an analysis, meaning decomposition, of the original dataset with its load of data through the high number of locations and associated time series. The EOF technique offers a method to represent the majority of the data's variance with a relatively small number of EOF and PC functions. If we examine a geophysical field[7], we can assume that the observations are highly correlated in space and time. This is exploited by the EOF analysis due to completely uncorrelated output vectors.

The two upcoming sections examine the basic EOF Analysis and the *Complex Empirical Orthogonal Function (CEOF)* Analysis. The latter is a special case of the initial, but it also investigates the time order of the variables, which is not facilitated by the regular EOFs.

4.3.1 Basic EOF Analysis

This examination of the EOF procedures is taken from (Hannachi et al., 2007) and (Wilks, 1995) and follows the most common notation and structure. A very general and academic approach is given in (Storch and Zwiers, 2002).

[7] air pressure, ocean temperature or soil moisture for example

The initial motivation for EOFs (e.g. by Lorenz) was to achieve a decomposition of a space-time field $X(t,s)$:

$$X(t,s) = \sum_{k=1}^{M} c_k(t) u_k(s) \tag{4.6}$$

Here, t and s represent for temporal and spatial position and M is the number of functions (modes) contained in the dataset (the field). $X(t,s)$ is decomposed into a set of basic functions of space $u_k(s)$ and expansion functions of time $c_k(t)$. This can be seen as new set of variables that capture the most of the observed variance from the initial dataset through a linear combination of the original variables (Hannachi et al., 2007). The very point here is that although the vast majority of information is reproduced, M is much smaller than s and consequently the new set of variables is much more handy.

To begin with, a gridded dataset is presumed that describes a spatiotemporal field $X(t,s)$, representing the value of the field[8] X at time t and location s. Then the data can be noted as matrix X:

$$X = (\mathbf{x}_1, \mathbf{x}_2, \ldots, \mathbf{x}_{\mathcal{T}})^T = \begin{pmatrix} x_{11} & x_{12} & \cdots & x_{1\mathcal{S}} \\ x_{21} & x_{22} & \cdots & x_{2\mathcal{S}} \\ \vdots & \vdots & \ddots & \vdots \\ x_{\mathcal{T}1} & x_{\mathcal{T}2} & \cdots & x_{\mathcal{T}\mathcal{S}} \end{pmatrix} \tag{4.7}$$

In the matrix, the row-vectors in the matrix $\mathbf{x}_{t.} = (x_{t1}, x_{t2}, \ldots, x_{t\mathcal{S}})^T$ are the value (or the map) of the field at times t and the column-vectors in the matrix $\mathbf{x}_{.s} = (x_{1s}, x_{2s}, \ldots, x_{\mathcal{T}s})$ are the time series at locations s. The indexing in time is $t = 1, 2, \ldots, \mathcal{T}$[9], in space the indices are $s = 1, 2, \ldots, \mathcal{S}$. In this study, all datasets are considered to contain more spatial than temporal variables, meaning $\mathcal{S} > \mathcal{T}$.

To eliminate the impact of the actual size and unit of values, EOF analysis is conducted on centred data, or on *anomalies* x'. For each time series, the mean is calculated and then subtracted from the time series values:

$$\bar{x}_{.s} = \frac{1}{\mathcal{T}} \sum_{k=1}^{\mathcal{T}} x_{ks} \tag{4.8}$$

$$x'_{ts} = x_{ts} - \bar{x}_{.s} \tag{4.9}$$

An alternative approach is to define anomalies as deviation from *climatology values*. Hence, the mean of all values from the same period p during the year is built and then subtracted from the

[8] e.g. soil moisture in Australia
[9] Please do not confuse with $()^T$ (matrix transposition)

original values:

$$\bar{c}_{.s} = \frac{1}{\mathcal{P}} \sum_{k=1}^{\mathcal{P}} x_{ks} \tag{4.10}$$

$$x'_{ts} = x_{ts} - \bar{c}_{.s} \tag{4.11}$$

For the sake of simple notation, from now on, the dash for the anomalies will be dropped and X or x will simply denote the anomaly data. As a note, the covariance matrices for the original data (x) and the anomalies (x') are identical as shown in (Wilks, 1995).

If the data stems from a regular geographic grid defined by latitudes and longitudes, an area weighting is recommended as in (Hannachi et al., 2006). In order to account for the actual area represented by the locations s, the times series (the columns) in the data matrix X are multiplied with latitudinal weights w_s, which depend on the location's latitude φ_s:

$$w_s = \sqrt{\cos \varphi_s}. \tag{4.12}$$

As a next step, the sample covariance matrix is assembled. It contains the covariance between the time series of any pair of grid points (s_i, s_j):

$$s_{ij} = [S]_{ij} = \frac{1}{\mathcal{T}} \sum_{t=1}^{\mathcal{T}} x_{ti} x_{tj} \tag{4.13}$$

or in matrix notation:

$$S = \frac{1}{\mathcal{T}} X^T X. \tag{4.14}$$

The covariance matrix S has in its diagonal the sample variances of the $\mathcal{S}$ spatial elements of the dataset X and the covariances among these variables in the off-diagonal positions. If a correlation analysis is desired, this empirical covariance matrix is replaced by the empirical correlation matrix, which simply can be done by the division of the anomalies by the standard deviation of the time series samples in the beginning. This is suggested by (Wilks, 1995) if different units or physical parameters form the initial dataset, which would distort the numerical conditions of the procedure (e.g. values in Metres would outnumber values in Kilometres).

4.3.1.1 EOFs from Eigenvalue Analysis

In order to find among the variables uncorrelated linear combinations (*the modes*) that explain maximum variances, vectors $\mathbf{e} = (e_1, e_2, \ldots, e_{\mathcal{S}})^T$ need to be found that point in the directions

of maximum variability. This, together with $\mathbf{e}$ has unit-length, means that $X\mathbf{e}$ has maximum variability, which further yields:

$$\max(\mathbf{e}^T S\mathbf{e}) \text{ with } \mathbf{e}^T\mathbf{e} = 1 \tag{4.15}$$

This now leads to an eigenvalue problem:

$$S\mathbf{e} = \lambda^2\mathbf{e} \tag{4.16}$$

where the eigenvectors $\mathbf{e}_k$ and the eigenvalues λ_k of the k'th EOF have to be found:

$$\lambda_k^2 = \mathbf{e}_k^T S\mathbf{e} = \frac{1}{\mathcal{T}}\|X\mathbf{e}_k\|^2 \tag{4.17}$$

This gives a measure of the variance of the data accounted for the direction of $\mathbf{e}_k$. Normally, the eigenvalues are sorted in decreasing order as $|\lambda_1| \geq |\lambda_2| \geq \cdots \geq |\lambda_{\mathcal{S}}|$. Consequently, the largest eigenvalue is associated with the first eigenvector. The second largest eigenvalue describes the variance in direction of the second eigenvector, which is orthogonal to the first and so on. The spectrum of the covariance matrix S composed of the eigenvalues λ_k provides information on the distribution of power (variation) and on the separation of the EOF patterns. For example, high/low power is associated respectively with low/high frequency variability. Low frequency and large scale patterns tend to capture most of the variance observed in the system. The first modes, or empirical orthogonal functions, represent most of the variability in the data. Furthermore, the sum of all eigenvalues equals one:

$$\sum_{k=1}^{\mathcal{S}} \lambda_k = 1 \tag{4.18}$$

This counts for the fact that the entirety of modes represents all variability in the data field. Commonly, the fraction of the eigenvalues is expressed in percent to emphasise the EOF's share in total variance.

Finally, the anomaly field X is projected onto the EOFs. The results are the *k Principal Components (PCs)* $\mathbf{p}_k$ of the data field X:

$$p_{tk} = \sum_{j=1}^{\mathcal{S}} x_{tj} e_{kj} \tag{4.19}$$

or in matrix notation

$$\mathbf{p}_k = X\mathbf{e}_k. \tag{4.20}$$

The geometrical meaning of these vectors is depicted in Figure 4.4.

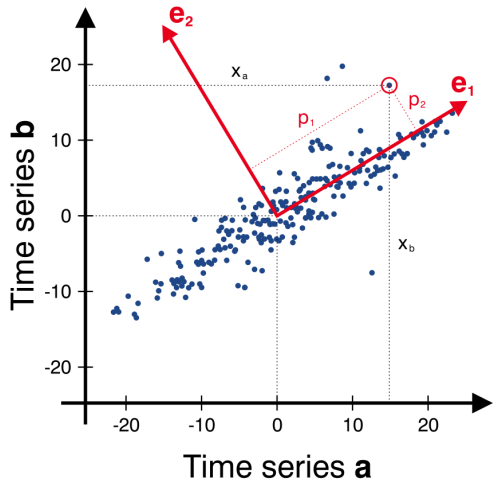

Figure 4.4: *To illustrate the outputs of an EOF analysis, this figure shows a scatterplot of two timeseries of some geophysical parameter. This can be interpreted as a very simple case of a field $X(t,s)$, meaning it contains only one time series for two locations. Anomalies have been calculated so that the data is centred. After (Wilks, 1995).*
One can see the pairs of observations in blue; the eigenvectors of the fields' covariance matrix e_1 and e_2 are in red with exaggerated length for clarity. Latter are the two EOFs of this system and have unity length. Please note their orthogonality and e_1 is aligning with the direction of greatest variance. The coordinates are specified in two coordinate systems: The black ordinates correspond to original values and the red ordinates are the values of the PCs of each observation. Again, the PCs are the projections of the original data onto the EOFs as written in Equation (4.20).

Now, the initial problem in equation (4.6) has been solved and the principal components a_k of the dataset $X(t,s)$ can be calculated. Equation (4.6) and Equation (4.19) have the same structure and describe the same dataset. The time function $c_k(t)$ and the space function $u_k(s)$ correspond to x_{tj} and u_{kj}, respectively (Hannachi et al., 2007).

To avoid any confusion, the kth EOF $\mathbf{e}_k$ (spatial indexing) and PC $\mathbf{p}_k$ (temporal indexing) are noted again separately:

$$\mathbf{e}_k = \begin{pmatrix} e_{k1} \\ e_{k2} \\ \vdots \\ e_{k\mathcal{S}} \end{pmatrix} \qquad \mathbf{p}_k = \begin{pmatrix} p_{1k} \\ p_{2k} \\ \vdots \\ p_{\mathcal{T}k} \end{pmatrix} \tag{4.21}$$

Depending on the scientific discipline or literature, there are several terms for the PCs: EOF expansion coefficients, EOF amplitudes, PC time series or PC scores. On the other hand, EOFs are often called PC loadings, pattern coefficients, modes of variation or simply PCs(!). It should be clearly stated that this study sticks with the in Earth sciences commonly used terms EOFs and PCs for the spatial and temporal patterns, respectively. Again, the EOFs are the eigenvectors of the data's covariance matrix; the PCs are the projection of the data onto these eigenvectors.

4.3.1.2 EOFs from Singular Value Decomposition

Instead of determination of the covariance matrix and the eigenvectors and -values, the *Singular Value Decomposition (SVD)* technique can be used (Hannachi et al., 2007; Esquivel and Messina, 2008). The $\mathcal{T} \times \mathcal{S}$ data matrix X can be decomposed as

$$X = P\Sigma E^T. \tag{4.22}$$

With $r = \text{rank}(X)$ and $r \leq \min(\mathcal{T}, \mathcal{S})$, the matrix P has the dimension $\mathcal{T} \times r$. E has the dimensions $r \times \mathcal{S}$. Both matrices are orthogonal, so that $P^T P = E^T E = I_r$, which is the identity matrix of order r. The columns of P are the left singular vectors $\mathbf{p}_r$, and the columns of E are the right singular vectors $\mathbf{e}_r$ of the data matrix X.

The Σ matrix is diagonal and contains the (positive) singular values of X, so that

$$\Sigma = \text{diag}(\sigma_1, \sigma_2, \ldots, \sigma_r) \tag{4.23}$$

in decreasing order

$$\sigma_1 \geq \sigma_2 \geq \cdots \geq \sigma_r \geq 0 \tag{4.24}$$

The SVD applied to the covariance matrix S yields to

$$S = \frac{1}{\mathcal{T}} XX^T = \frac{1}{\mathcal{T}} (P\Sigma E^T)(P\Sigma E^T)^T = \frac{1}{\mathcal{T}} E\Sigma\Sigma^T E^T = \frac{1}{\mathcal{T}} E\Sigma^2 E^T \tag{4.25}$$

It can be shown that the SVD of the anomaly data X and the eigenvalue analysis of its covariance matrix X deliver the same information. The columns $\mathbf{p}_r$ of P and the columns $\mathbf{e}_r$ of E are the left and right singular vectors of X, respectively. As examined in (Storch and Zwiers, 2002), the left singular vectors are the eigenvectors of $X^T X$ and the right singular vectors are the eigenvectors of $S = XX^T$. One can therefore infer directly the EOFs and PCs from the SVD of X. The singular values σ_r of X are the square roots of the eigenvalues λ_k of S per $\mathcal{T}$, so that

$$\lambda_k = \frac{1}{\mathcal{T}} \sigma_k^2 \tag{4.26}$$

After separation of singular vectors and -values of X, equation (4.22) can be written as

$$\mathbf{x}_t = \sum_{k=1}^{r} \mathbf{p}_{tk} \sigma_k \mathbf{e}_k \tag{4.27}$$

This equation describes the synthesis of original data at all spatial locations at time t by r principal components. If a compression of the original data without a significant loss of information is desired, a truncation of the sum in equation (4.27) is possible, which means summing only over the first singular values instead of over all r. The choice of number of PCs or modes is arbitrary, but the first PC contain the most variability, as can be seen in equation (4.24). The truncation of modes M to m drops the equal sign in equation (4.6) and the synthesis of the original data out of the EOFs and PCs becomes an approximation:

$$X(t,s) \approx \sum_{k=1}^{m<M} c_k(t) u_k(s) \tag{4.28}$$

This formulation of the SVD is one out of many, but it offers a compact representation of the original data since it drops unnecessary zero singular values due to $r = \mathcal{T} \ll \mathcal{S}$, which is the case for meteorological or environmental parameters.

4.3.2 Data Gaps

Spatio-temporal datasets as $X(t,s)$ often show some discontinuities in time series. Gaps in the data X cause problems as the covariance matrix can not be formed completely. Replacing no-data-values by some distinct gap-value distorts the analysis arbitrarily. Unluckily, the places and

times of missing observations are not regular in most cases, which would render the treatment of these gaps easy by simply omitting the observations of certain locations (or times).

However, some literature like (Storch and Zwiers, 2002) presents methods to counter this problem. The method suggested here includes an alternative computation of the covariance matrix S and of its eigenvectors $\mathbf{e}_k$.

At occurrence of gaps in the data matrix X, Equation (4.13) needs to be altered to

$$\hat{s}_{ij} = [\hat{S}]_{ij} = \frac{1}{\|T_i \cap T_j\|} \sum_{t \in T_i \cap T_j} x_{ti} x_{tj} \tag{4.29}$$

in which, T_i is the set of components (values) that exists (no gap). Consequently, $T_i \cap T_j$ is the set of all indices, so that x_{ti} and x_{tj} exist. The $\| \cdot \|$ notates for the size (the number of elements) of the enclosed set. This facilitates that pairs of values only contribute to the calculation of the (co-)variances if both values mutual exist. In other words, if element i of time series j does not exist, element i of the other time series is skipped. Thus, in case of gaps, the dot product in equation (4.29) for $\hat{s}_{ij}$ is formed by vectors with fewer elements.

The second alteration affects equation (4.20) since the dot product with a gappy data vector in X can not be obtained. But however, a least square estimate can be obtained by choosing $\hat{\mathbf{p}}_i$ to minimise $\|\mathbf{x}_i - \hat{\mathbf{p}}_i \mathbf{e}^i\|$ (Storch and Zwiers, 2002). The least square estimate is given by

$$\hat{\mathbf{p}}_i = \frac{\sum_{j \in T} \mathbf{x}_j \hat{\mathbf{e}}_j^i}{\sum_{j \in T} \|\hat{\mathbf{e}}_j^i\|^2} \tag{4.30}$$

Here, the selection of sets of components is done in the same way as above. Only mutual existing elements in the data vector $\mathbf{x}$ and adopted eigenvector $\hat{\mathbf{e}}$ contribute to the calculation of the PC $\hat{\mathbf{p}}$. The denominator is the length (the norm) of the truncated eigenvector. Note that in case of no missing data, this equation is simply equation (4.20).

4.3.3 Complex EOF Analysis

With the basic EOF analysis presented in above section, we can derive dominant patterns (modes) in the variability of some geophysical dataset. It delivers the amount, or the amplitude, of the impact of one modes into the dataset's variance in space and time. But we can only find stationary patterns in the sense that they are not evolving in time. Thus, we have no clue about the relative time, or the phase, of this impact. The reason is that we completely disregarded the time order of the observations or the temporal evolution of the analysed field $X(t, s)$. EOFs are based on

(simultaneous) covariances, and consequently, the way the elements are arranged is irrelevant. In fact, two univariate time series and any permutation ($\pi_{f(t)}$) of them will yield the same covariance (Hannachi et al., 2007). This equality reads for two time series x_t and y_t as

$$\rho_{xy} = \mathrm{cov}(x_t, y_t) = \mathrm{cov}(\pi_{x_t}, \pi_{y_t}) \tag{4.31}$$

This means that any evolving or propagating pattern in the field can not be captured by basic EOFs. *Complex EOF analysis* brings here a remedy.

The complex EOF analysis provides a look at the temporal variability of the observed data while simultaneously it provides spatial information about the dominant modes as known from the basic EOF analysis. The complex technique is again empirical and data driven, which makes it well suited for the analysis of general linear and non-linear phenomena. Compared to basic EOF analysis, it can provide quantitative understanding of the underlying oscillating mechanisms (Esquivel and Messina, 2008). The method can detect propagation of spatial patterns and therefore enables analysis of moving modes. The presumption is that the signal can be represented as a wave and can therefore be generally described as:

$$x(t) = Ae^{i\omega t+\phi_0} = Ae^{i\phi} = A(\cos\phi + i\sin\phi) \tag{4.32}$$

in which A is the wave amplitude, e the Euler's constant (e ≈ 2.7182818284), i the imaginary unit, ω the frequency, ϕ_0 the phase shift at the origin and ϕ the actual phase (Woodhouse, 2006).

The main idea is then to complexify the original data in a clever way. There are several techniques suggested in literature (a good overview is given in Hannachi et al. (2007)). The method used in this study is called *Hilbert Empirical Orthogonal Functions (HEOF) Analysis* and its selection is reasoned by the fact that it is properly useful for analysis of a single spatiotemporal dataset. It was introduced by (Rasmusson et al., 1981).

4.3.3.1 Hilbert Transform

The HEOF analysis is based on the "complexification" of the original data. The original real-valued time series is made complex by adding its Hilbert transform as the imaginary part. As a consequence, the Hilbert transform gives information about the rate of change of the field, as an artificial imaginary part. It can be therefore seen as the time derivative of the original process. The HEOF analysis builds upon this complexified data and thus reveals variance characteristics of the process as well as its change (Storch and Zwiers, 2002).

The Hilbert transform should be shortly introduced, but a complete derivation is out of this study's scope and can for example be found in (Storch and Zwiers, 2002; Rasmusson et al., 1981).

A time series from a field $X(t,s)$ can be described as already shown like

$$\mathbf{x}_t = (x_{1s}, x_{2s}, \ldots, x_{tS}) \tag{4.33}$$

but also with vector Fourier coefficients $\mathbf{a}(\omega)$ and $\mathbf{b}(\omega)$ as

$$\mathbf{x}_t = \sum^{\omega} \mathbf{a}(\omega) \cos \omega t + \mathbf{b}(\omega) \sin \omega t. \tag{4.34}$$

However, if the wave is propagating and not static, a complex representation as in Equation (4.32) is required. The general complex Fourier decomposition yields

$$\mathbf{y}_t = \sum^{\omega} \mathbf{c}(\omega) e^{-i\omega t} \quad \text{with} \quad \mathrm{Re}[\mathbf{y}_\mathrm{t}] = \mathbf{x}_\mathrm{t} \quad \text{and} \quad \mathbf{c}(\omega) = \mathbf{a}(\omega) + i\mathbf{b}(\omega). \tag{4.35}$$

Re[] denotes for the real-part-operator. Above equation can then be reformed to

$$\mathbf{y}_t = \mathbf{x}_t + i\mathcal{H}(\mathbf{x}_t) \tag{4.36}$$

where the imaginary part is the Hilbert transform of $\mathbf{x}_t$:

$$\mathcal{H}(\mathbf{x}_t) = \sum^{\omega} \mathbf{b}(\omega) \cos \omega t - \mathbf{a}(\omega) \sin \omega t \tag{4.37}$$

$\mathcal{H}(\mathbf{x}_t)$ can simply be seen as function describing the initial time series shifted by $\frac{\pi}{2}$ (Hannachi et al., 2007). As noted already, it can also be thought of as the time derivative of the original process (Storch and Zwiers, 2002). Therefore, locally in the frequency domain, $\mathcal{H}(\mathbf{x}_t)$ provides information about the rate of change of $\mathbf{x}_t$ with respect to time t. When looking at equation (4.34) and equation (4.37), the derivative character as well as the $\frac{\pi}{2}$-shift become manifest in the change of the *sin* to the cos at the **b**-term and the change of the cos to the $-\sin$ at the **a**-term, which reflects the basic relations between these two functions.

As a note, in formal terms, the Hilbert transform of a continuous time series $x(t)$ is defined by the convolution

$$\mathcal{H}(x(t)) = \frac{1}{\pi} \int \frac{x(u)}{t-u} du. \tag{4.38}$$

In practice, an estimate of the Hilbert transform is obtained from the Fourier coefficients and they are commonly derived from fast Fourier transform (FFT) routines (Bouzinac et al., 1998).

4.3.3.2 Hilbert EOF Analysis

The calculation of the Hilbertian EOFs (HEOFs) is very similar to the derivation of "normal" EOFs. In the very beginning, the real-valued time series of the field $X(t,s)$ are expanded as in Equation (4.36). Then, the covariance matrix of the complexified dataset Y yields

$$S_{yy} = \frac{1}{\mathcal{T}} \sum_{k=1}^{\mathcal{T}} \mathbf{y}_t \mathbf{y}_t^{*T} \tag{4.39}$$

in which $*$ donates the complex conjugate, and $\mathcal{T}$ is the number of elements of the time series as above. The eigenvectors of S_{yy} are equal to the wanted HEOFs. Again, they can also be obtained as the right complex singular vectors of the data matrix Y through SVD. The complex PCs (CPCs) are obtained similarly to equation (4.20). The eigenvalues (they are still real-valued) follow the same calculations as in the regular EOF case, too.

4.3.4 EOF Interpretation

So, what do we have got? We calculated the anomaly data X of the spatiotemporal field $X(t,s)$ that describes some geophysical parameter. We created the covariance matrix to learn about the relationships between the values. Either from eigenvalue analysis or from SVD of X, we inferred the EOFs $\mathbf{e}_k$, the PCs $\mathbf{p}_k$ and the eigenvalues λ_k. Please remind equation (4.21). Additionally, we used the complex Hilbert transform to include also time derivative information.

The EOFs and the PCs reflect spatial and temporal patterns, respectively, and the eigenvalues describe share on total variance in X for all k modes in the data. Indeed, EOFs can be mapped descriptive to cartographic figures and PCs can be plotted meaningful as time series.

Empirical Orthogonal Functions The kth EOF carries information about the spatial distribution of the kth mode. Each eigenvector $\mathbf{e}_k$ contains exactly $\mathcal{S}$ elements, and these elements correspond one-to-one with each of the $\mathcal{S}$ locations in the original dataset. Each of these eigenvector elements e_{jk} can be plotted on a map at the same location as its respective data value x_j (Wilks, 1995). Such a map depicts which locations contribute most strongly to the associated mode. To put it into other words, this map shows the geographic distribution of simultaneous data anomalies associated with the kth mode. It should be noted that the different modes are completely uncorrelated since the EOFs (the eigenvectors) are mutual orthogonal in the data space.

Principal Components The kth PC provides information about the temporal variation of the kth mode throughout the observation time of the field $X(t,s)$. The vector $\mathbf{p}_k$ is the dot product as in equation (4.20) and contains exactly $\mathcal{T}$ elements and reflects the amplitude (the strength) of the mode in the dataset in the time domain. Again, the kth PC, as a time series, is completely uncorrelated with the other mode's time series.

Statistical Significance of Modes The spatial orthogonality of the EOF's imposes constraints upon the shapes of the modes. Each mode k must be spatially orthogonal to all the modes $l < k$ that precede it in the hierarchy. The lower the rank of its eigenvalue the more modes it is required to be to be orthogonal to, and the more likely that its pattern is dictated by mathematical constraints, rather than real physics or natural dynamics. For this reason, many studies recommend to regard only the leading three to four EOFs (Wilks, 1995; Hannachi et al., 2006).

Complex EOFS The question on the purpose of complex-valued HEOFs and CPCs may arise. The answer is that with the complex methods not only spatial and temporal amplitudes of the modes are obtained, but also spatial and temporal phase functions. From the decomposition, these four functions are gained for each mode, or pattern, k:

The spatial amplitude yields

$$S_k(s) = \sqrt{\mathbf{e}_k \mathbf{e}_k^*}. \tag{4.40}$$

The spatial phase yields

$$\phi_k(s) = \arctan \frac{Im[\mathbf{e}_k]}{Re[\mathbf{e}_k]} \tag{4.41}$$

The temporal amplitude yields

$$T_k(t) = \sqrt{\mathbf{p}_k \mathbf{p}_k^*} \tag{4.42}$$

The temporal phase yields

$$\varphi_k(t) = \arctan \frac{Im[\mathbf{p}_k]}{Re[\mathbf{p}_k]} \tag{4.43}$$

in which $Re[]$ is the real part and $Im[]$ the imaginary part of the complex valued vectors and $*$ donates the complex conjugate.

The spatial phase function provides information on the relative phase within the oscillation of the respective mode. The temporal phase function allows drawing conclusion on the frequency of the oscillation of the associated mode. The amplitude functions deliver the same kind of information as the EOFs and PCs obtained in basic EOF analysis.

4.4 Implementation

The elaboration of this study was carried out at the *Institute of Photogrammetry and Remote Sensing (IPF)* and local hard- and software was utilised. Hence, the implementation of the above described formulae was done in *Interactive Data Language (IDL)*.

Data Preparation Several manipulations of WACMOS SSM data have been performed during the study work:

1. SSM *daily time series* were resampled to *monthly* and *seasonal means* by simply building the average for each period. This is reasoned by the fact that daily values are not meaningful with regard to climatological considerations and monthly or better seasonal means provide a more stable representation of SSM conditions.

2. SSM *climatologies* have been calculated for the months and seasons of the year. Accordingly, for each of the 12 months an average over all years was built. The same was done for the four seasons *December-January-February (DJF)*, *March-April-May (MAM)*, *June-July-August (JJA)* and *September-October-November (SON)*. As equation, the calculation of seasonal climatology for season p at locations s is

$$\bar{c}_{ps} = \frac{1}{32} \sum_{k=1}^{32} x_{ks} \quad \text{with} \quad k \in \mathcal{P}. \tag{4.44}$$

   $\mathcal{P}$ is the set of all values over the 32 years stemming from the specified season. One should keep in mind, that in the southern hemisphere, these represent the seasons in the following sequence: Summer-Fall-Winter-Spring.

3. SSM *anomalies* have been derived from monthly and seasonal means by building the difference *mean - climatology* for each period over the 32 years of WACMOS data.

These operations were done for each $0.25° \times 0.25°$ point of the WACMOS grid point, yielding roughly 11000 datasets for each datatype over Australia. Concerning climate indices, also monthly and seasonal means have been built to adapt them to the temporal formate of the SSM datasets. Begin and end dates of the seasonal times series investigated in the study are DJF 1979 and SON 2010 what yields 386 samples. The IODMI time series ends earlier (September 2010/JJA 2010) due to data restrictions starting October 2010.

EOF Analysis Both non-complex and complex EOF analysis were applied to the WACMOS SSM data according to Section 4.3. Initially not clear, what will deliver a better performance in representing the soil moisture, the analysis has been carried out with monthly and seasonal samples, respectively. Instead of simply centred time series (anomalies in respect to overall mean), anomalies as described above have been used as input data. The latter calculation was chosen, since deviation from the climatology is expected to reflect better the variation of SSM conditions.

Accounting for the inferior data density (and quality) of SSM/I as reported in (Liu et al., 2009), the period JJA 1987 - MAM 1992 has been disregarded by the EOF analysis. This is mathematically necessary for the CEOF analysis since a big number of irregularly occurring data gaps endangers the accuracy of the Hilbert transform estimate. For consistency reasons, the data truncation was also done for the non-complex EOF analysis. Recognising the improved data quality on the basis of WACMOS' augmented sensor constellation since 1998, the period January 1998 to December 2010 (DJF 1998 to SON 2010) has been examined separately. First, a data selection based on time series sample size was done: Only time series with an sample size greater than an empirical determined threshold are considered valid and only the corresponding locations (gridpoints) take part in the EOF analysis.

The analysis has been done for the complete (but truncated) time series as well as for the seasonal time series separately. Here, time series consisting only of values stemming from the particular season throughout 1979-2010 are meant. Consequently, as an example, a sample describes all 32 values from DJF and allows to investigate impacts on Australia's SSM conditions in summer.

Correlation Analysis The main purpose of the thesis is to detect relationships between SSM in Australia and regional climate modes. Therefore, Spearman correlations between SSM time series and climate indices time series have been calculated at each of the 11000 locations in Australia. The resulting correlation coefficients have been plotted to maps, masking out all correlations with significance (as described in Section 4.2.1) lower than $p = 0.95$. This was done for the complete time period 1979-2010 and for 1998-2010 all over the seasons and again, for the seasons separately.

Secondly, the correlations ρ between the indices and the temporal amplitudes (from the PCs) of the EOFs have been computed in order to find relations between the major SSM modes and climate modes. Previously to computation of ρ, a boxcar average with width 2 was applied for smoothing of time series. Once again, the same temporal investigation scheme as above was done.

Chapter 5

Results and Discussion

A picture is worth a thousand words

This section presents the results from the methodology as elaborated above applied on the WACMOS SSM data and the climate mode indices. It starts with a selection of resampled WACMOS data and its capability to reflect soil moisture conditions. Afterwards, the SSM data is set into relation with climate modes with Spearman correlation as measure. It concludes with extensive non-complex and complex analyses of the WACMOS data in respect to climate modes.

5.1 Resampled WACMOS SSM over Australia

The daily time series from WACMOS SSM have been resampled into monthly and seasonal mean time series. Monthly and seasonal climatologies have been computed to determine the overall soil moisture regime as shown in Figure 5.1. All WACMOS SSM values are given in $\frac{1}{100} m^3 m^{-3}$.

In Figure 5.1 the seasonal SSM climatology maps of Australia are mapped. In accordance with Figure 2.11, the latitudinal movement of the ITC-zone throughout the year is evident and the general rainfall regime is reproduced. However, discontinuities are obvious too and it is not trivial to clarify whether they reflect correctly soil properties or if the local SSM is flawed. At least the two stretched regions north-east of the centre and the spots in north-west with clearly wetter conditions than the surrounding can be recognised as wet vertisol-soils as reported in (Liu et al., 2010).

On the basis of the climatologies, SSM anomalies have been calculated to investigate months and seasons with large deviations from the overall seasonal mean. Selected periods with outstanding anomaly patterns are mapped in the following figures.

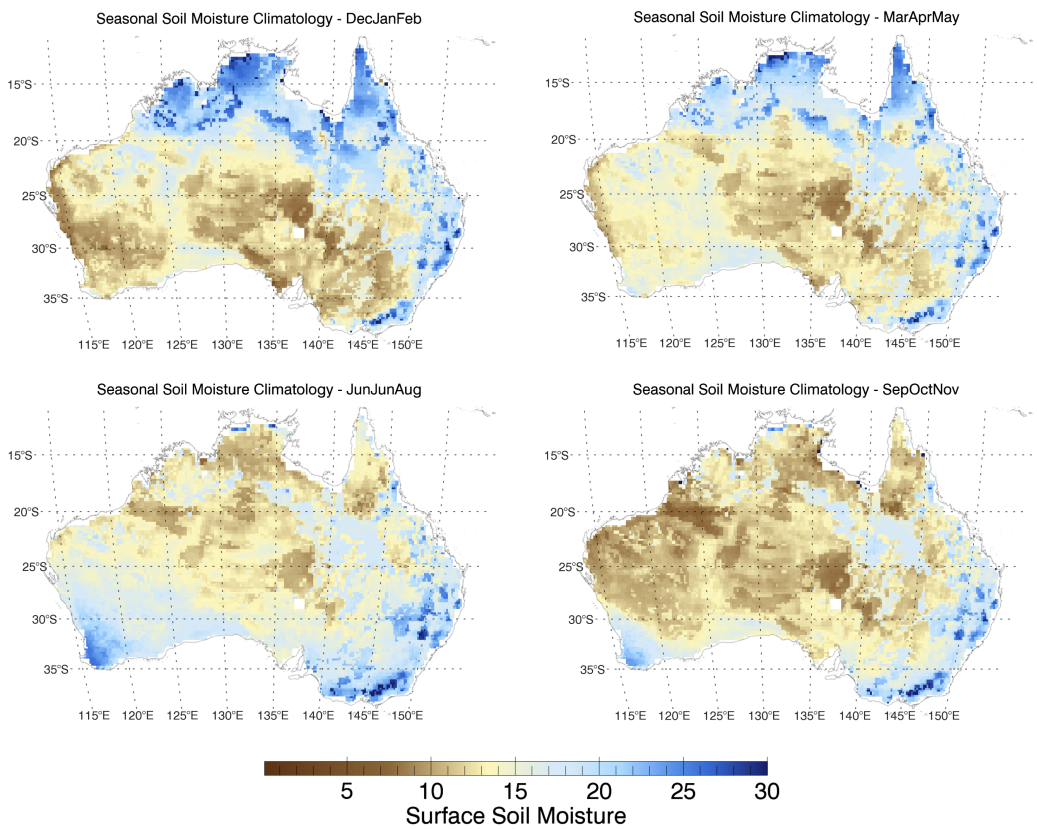

Figure 5.1: *This assembly consists of maps displaying the seasonal climatology SSM values from the WACMOS dataset. Hence, the colours indicate the mean SSM value for summer (top left), autumn (top right), winter (bottom left) and spring (bottom right) from DJF 1979 to SON 2010.*

Summer/Autumn 1983 (Figure 5.2) During the summer, overwhelming drier-than-normal conditions for the entire continent have been observed and this is totally contrary to the following spring season. The greater centre seemed to receive an extraordinary amount of rainfall between summer and spring. For the complete year 1982, the IOD was in a strongly positive phase (values above +2) which ended at the begin of 1983. Simultaneously, ENSO entered an all-time negative episode (down to -30) at the beginning of 1983 and negative conditions sustained until mid of 1984. Both observations perfectly fit to theory of the climate indices' impact on Australian rainfall patterns.

Summer/Winter 1987 (Figure 5.3) Compared to 1983, the anomalies are far not so developed but however, IODMI and SOI show similar amplitudes. This reflects that there is no one-to-one relationship of the climate modes and rainfall or SSM in Australia. As in 1983, SAM is in a rather neutral state.

Autumn/Winter 1998 (Figure 5.4) 1998. THE year of big changes climate index amplitudes: SOI values were boosting from a very negative state with -28 (during the long-lasting 1997-El Niño) to above +15 in July 1998. IODMI fell from all-time positive +3,5 in mid of 1997 to -2 in autumn 1998. SAM entered a longer positive episode at the end of 1997. Although the SSM anomalies do not follow the huge amplitudes of the indices, their transitions comes out clearly: Dryness during 1997 due to El Niño and negative IOD is especially eminent in northern and western Australia. After six months, wetter-than-normal conditions spread over the continent.

Autumn 2005 / Spring 2010 (Figure 5.5) A strong, widespread, dry anomaly hit Australia in autumn 2005. In February of the same year, a short, but distinct negative peak, is recorded in the SOI monthly time series. IOD shows a negative, but low-key negative amplitude with a suspected impact on the wetter south-east. A completely inverted pattern is apparent in the SSM anomaly map of spring 2010. During this period, several severe floods hit eastern Australia. The Queensland-floods are widely known in public due to news broadcasting and causing human deaths and big damage in infrastructure. Both ENSO and SAM have been in distinct positive conditions since the beginning of 2010. Again, IODMI maybe counters the dominant pattern and causes wetter conditions in the south-east as being in a slightly positive state. Please note that white gridpoints indicate absence of sufficient samples.

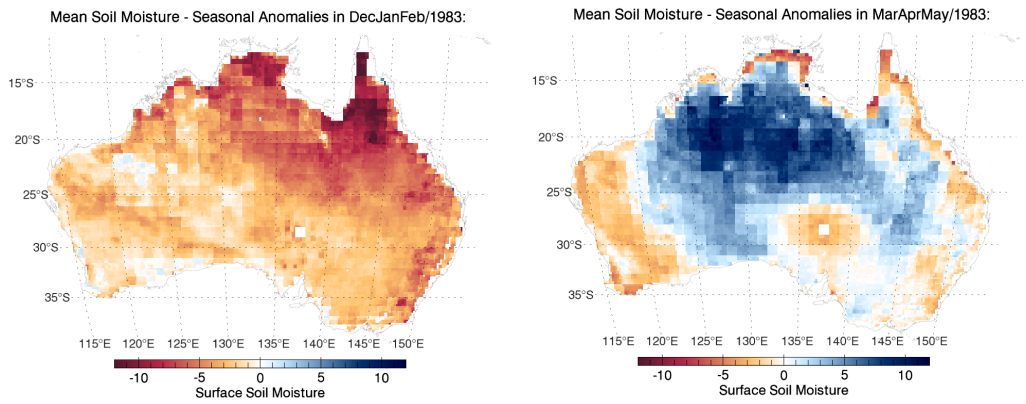

Figure 5.2: *The maps show seasonal SSM anomalies in DJF (summer, left) and MAM (autumn, right) in 1983.*

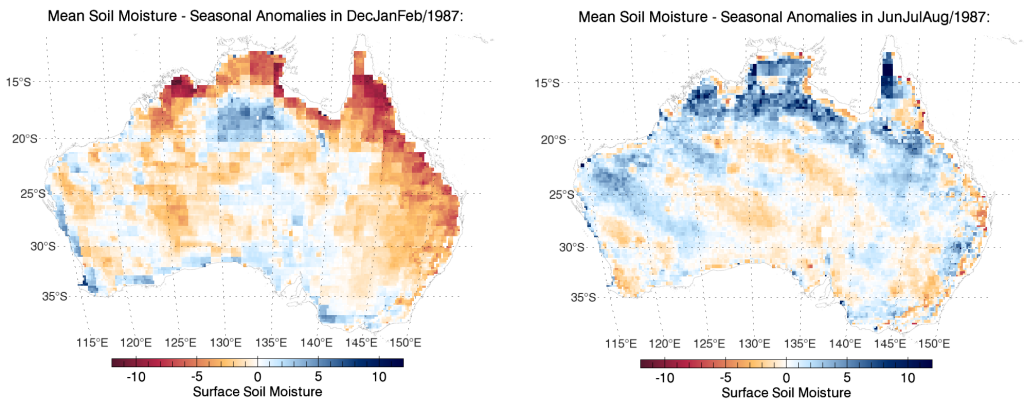

Figure 5.3: *Same as in Figure 5.2 but for DJF 1987 and JJA 1987.*

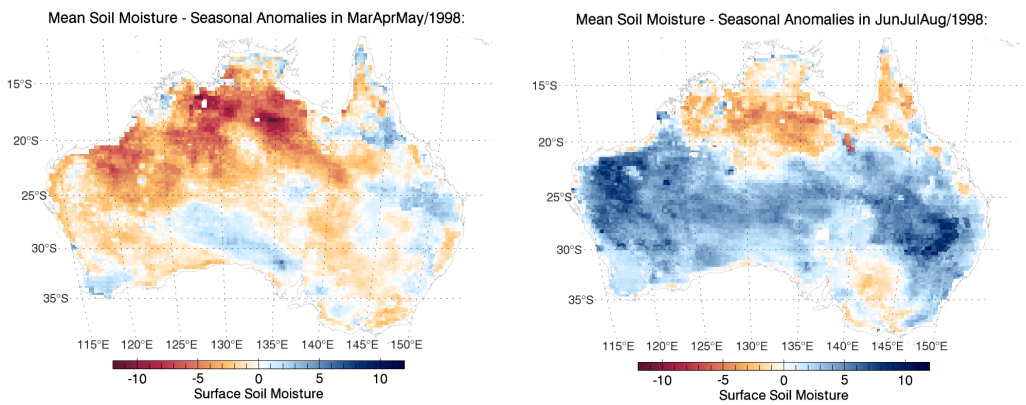

Figure 5.4: *Same as in Figure 5.2 but for MAM 1998 and JJA 1998.*

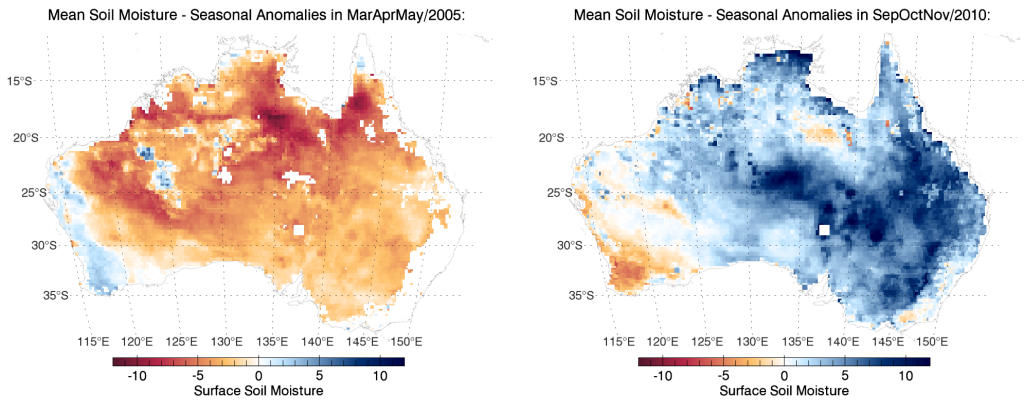

Figure 5.5: *Same as in Figure 5.2 but for MAM 2005 and SON 2010.*

5.2 Correlation Maps

This section is dedicated to correlation maps. These maps depict for each gridpoint in Australia the Spearman correlation coefficient of seasonal WACMOS SSM anomaly time series and climate mode indices or Solar Flux. Consequently, the impact areas of climate modes can be identified. To focus on highly correlated areas, a significance masking was applied so that only pixels are coloured with a significance-level below 5% ($p < 0.05$).

In Figure 5.6 the influence areas of ENSO in eastern and northern Australia towards the Pacific Ocean is certain, especially when regarding the shorter time series starting 1998. In (Liu et al., 2009; Chiew et al., 1998), similar findings have been published. As for ENSO, comparable certainty is observed for IOD in the western parts and the south-eastern region, which is also known as impact area of the IOD. For SAM, strong correlations are found in the center, in the east and in the north. These regions do not build a compact coverage of the area and thus reflect the complex nature of SAM as described in Section 2.2.3. Figure 5.7 envisages two very interesting findings of the correlation analyses: The influence of IOD on Australia's "Big Dry" starting in 1995 is documented by strong and widespread negative correlation that is evident in the south, east and north, but not in the west. The gap in the west is in contrast to above findings but in good accordance to findings of (Ummenhofer et al., 2009): The article discovered an eminent impact of IOD in precipitation amount in south-eastern Australia since 1995 and is a major reason for consecutive droughts called "Big Dry". The right map of Figure 5.7 presents a possible relationship of SSM and solar activity represented by Solar Flux F10.7. The observation period is 1979-2010 and thus features long-term investigation of the relationship. Although not many gridpoints seem affected, a weak but distinct pattern can be detected. All around Australia's coastline an inverse relationship may reflect some (direct or indirect) connection between solar activity and SSM.

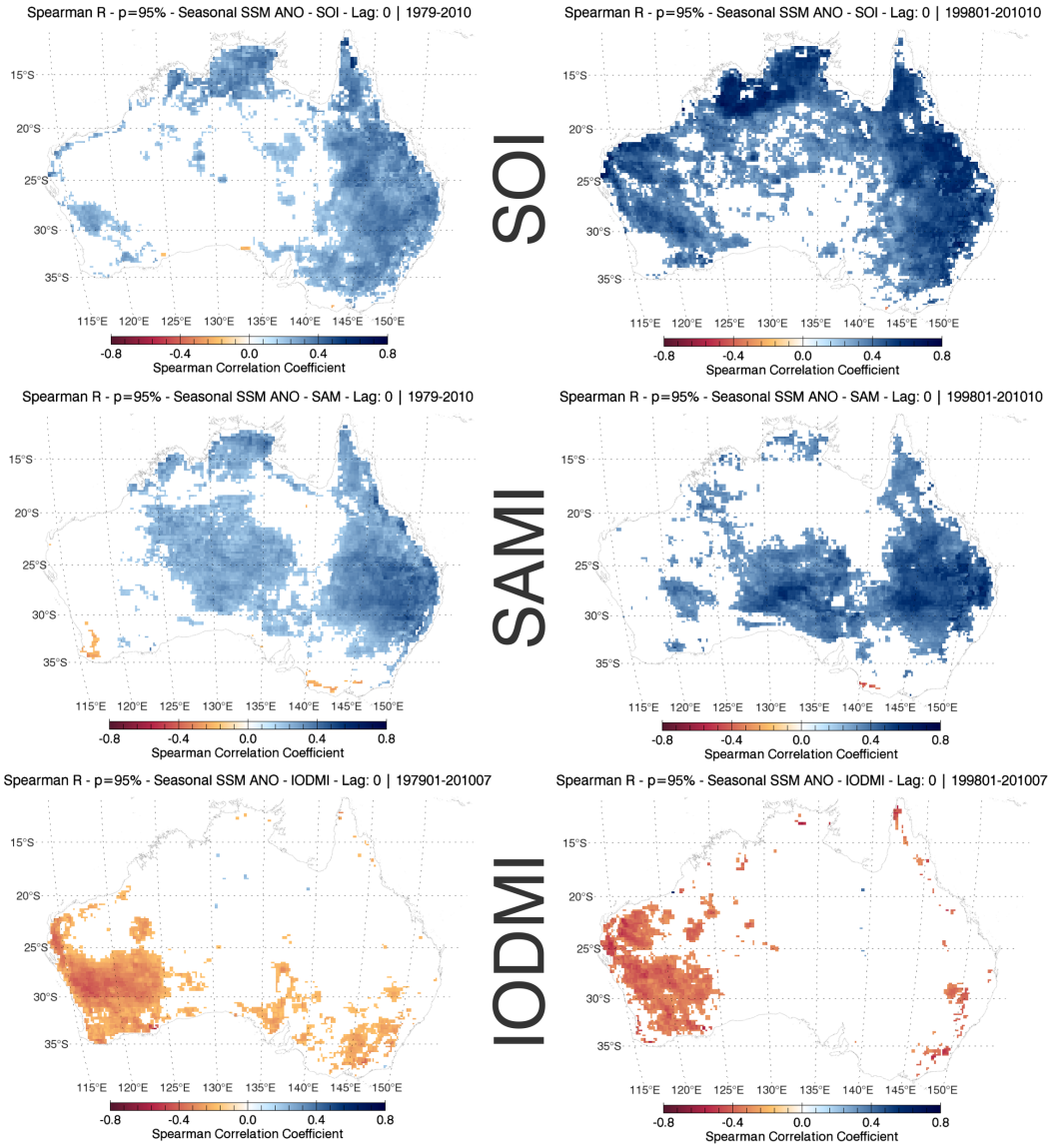

Figure 5.6: *The maps of Australia reflect Spearman correlation of climate indices and seasonal WACMOS SSM anomalies with positive correlation in blue and negative in red. In the left column the observation period is 1979-2010; in the right it is 1998-2010. White areas are masked due to poor significance higher than 0.05. The maps proof theoretical assumptions as discussed in the text above.*

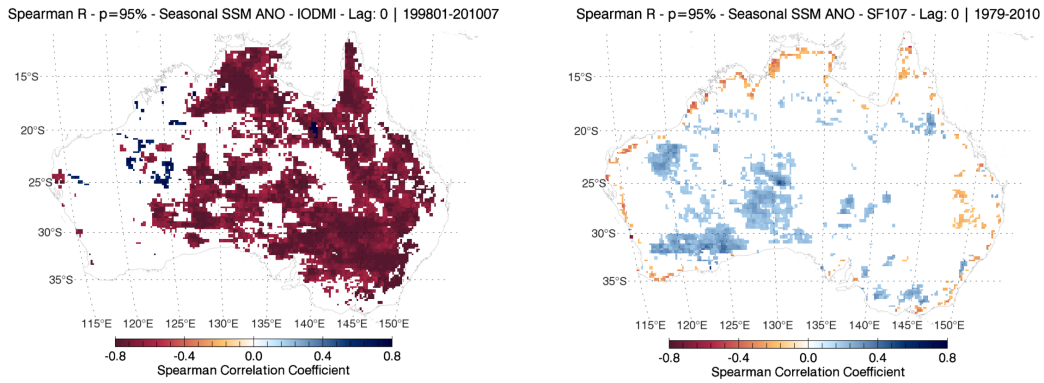

Figure 5.7: *On the left, correlation between IODMI and SSM for the period 1998-2010 is displayed. On the right, correlation between F10.7 and SSM is displayed.*

5.3 EOF Analyses

The EOF methodology was applied to the WACMOS SSM anomaly field over Australia. Before EOF analyses were performed, several different selections of Australian WACMOS time series samples concerning data density have been done. Consequently, a discrimination of datasets regarding

1. the usage of time series as a whole or mute out some periods of low data density
2. muting out locations with a sample size below a certain threshold

yielded a variety of pre-settings concerning the EOF-input-matrix $X(t, s)$. The first consideration altered the temporal coverage of the EOF output, whereas the second option determines its spatial coverage. The choice of these preferences turned out to be crucial to the result since the configuration of the input matrix determines greatly the geometry of the eigenvectors and consequently the EOFs. Indeed, the first EOF patterns show only very little affection to the considerations 1 and 2 as above mentioned, but lower-ranking EOFs of different selections of the same dataset can not be compared in many cases. The settings leading to the results presented in this section were chosen in order to minimize both outliers in the modes' temporal amplitude (PCs) and spatial amplitude (EOFs).
Concerning discrimination 1: For all EOF and CEOF analysis the period SON 1987 to JJA 1993 is muted out to account for poor performance of SSM/I at densely vegetated areas in northern and eastern Australia
Concerning discrimination 2: For the EOF analysis on the complete SSM time series (over all seasons, Figure 5.8), only time series with a sample size ≥ 72 out of 108 have been accepted. Gridpoints that do not reach this limit are mapped in white. The 1979-2010 CEOF analysis (Figure 5.15, Figure 5.16, Figure 5.17) was applied to gridpoints with at least 76 samples.
For the seasonal decomposition presented in Figure 5.10, Figure 5.11, Figure 5.12 and Figure 5.13 the period SON 1987 to JJA 1993 is muted out too. Minimum sample size is here 20 out of 28.
For the separate analysis on the data starting in 1998 (Figure 5.14) no period needed to be cancelled out and the minimum time series sample size is for the complete series (all seasons) 40 out of 52 and for the seasonal decomposition it is 10 out of 13. The 1998-2010 CEOF analysis in Figure 5.18 is also applied to time series with at least 40 samples.

It needs also to confessed that the temporal and spatial data selection can also affect significantly the correlation coefficient between the PCs and climate mode indices. Thus, knowledge of the physical relation is essential when it comes to interpretation.

The EOF analyses presented in this section are stemming exclusively from seasonal WACMOS SSM data since the monthly analyses turned out to be less stable and do not bring valuable additional information. The gaps in the daily time series are considerably crucial to the monthly averages, but not to the seasonal.

5.3.1 EOFs from Time Series 1979-2010

Figure 5.8 presents the output of a non-complex EOF analysis applied on the WACMOS SSM anomalies over Australia from DJF 1979 to SON 2010. The (greater) SSM/I period from JJA 1987 to MAM 1992 has been disregarded by the analysis. Furthermore, only pixels with a temporal sample size greater than 72 seasons contribute to the calculation. On the left, the spatial patterns of the first five modes are mapped in colours from red over white to blue. White pixels indicate no amplitude of the mode at the location. Red and orange colours represent negative and blue colors positive amplitude, which correspond to the temporal normalized amplitudes on the right, respectively. The values are arbitrary in scale; only their relative amplitude is of importance (except if a re-assembling of the original data is desired). The EOF analysis as a decomposition of a dataset into discriminative parts is demonstrated.

On the first map, a homogeneous pattern dominates the entire continent, except for the southern coastal areas showing an inverse sign. It gradually increases from north to south and the PC proposes a strong, but irregular oscillation. The second EOF depicts a distinct north-south gradient and the corresponding PC points out a clear annual signal. This mode can be interpreted as the yearly, latitudinal movement of the ITC-zone. It governs the overall rainfall pattern as can be seen in Figure 2.11. For the third mode, a north to south-east behaviour can be detected. Mode 4 features a strong south-east to north-west slope and a still annual, but more varying temporal amplitude. Similar is mode 5 but with inverse signs and directions. Visually, the last mode shows an ENSO character with the strong negative spatial amplitude in the north and east and distinct negative PC since 2007.

The modes are ordered by the amount of represented variance, as mentioned in Section 4.3. This is reflected by the *spectrum* of the covariance matrix of $X(t, s)$ as shown in Figure 5.9.

As a next step, the PCs are set into relation to climate mode indices and Solar Flux as introduced in Section 2.2. Spearman correlation has been chosen as a measure for the relationship as described in Section 4.2.1 and the results are presented in Table 5.1.

Considering the correlation analysis, three points can been detected at a first glance:

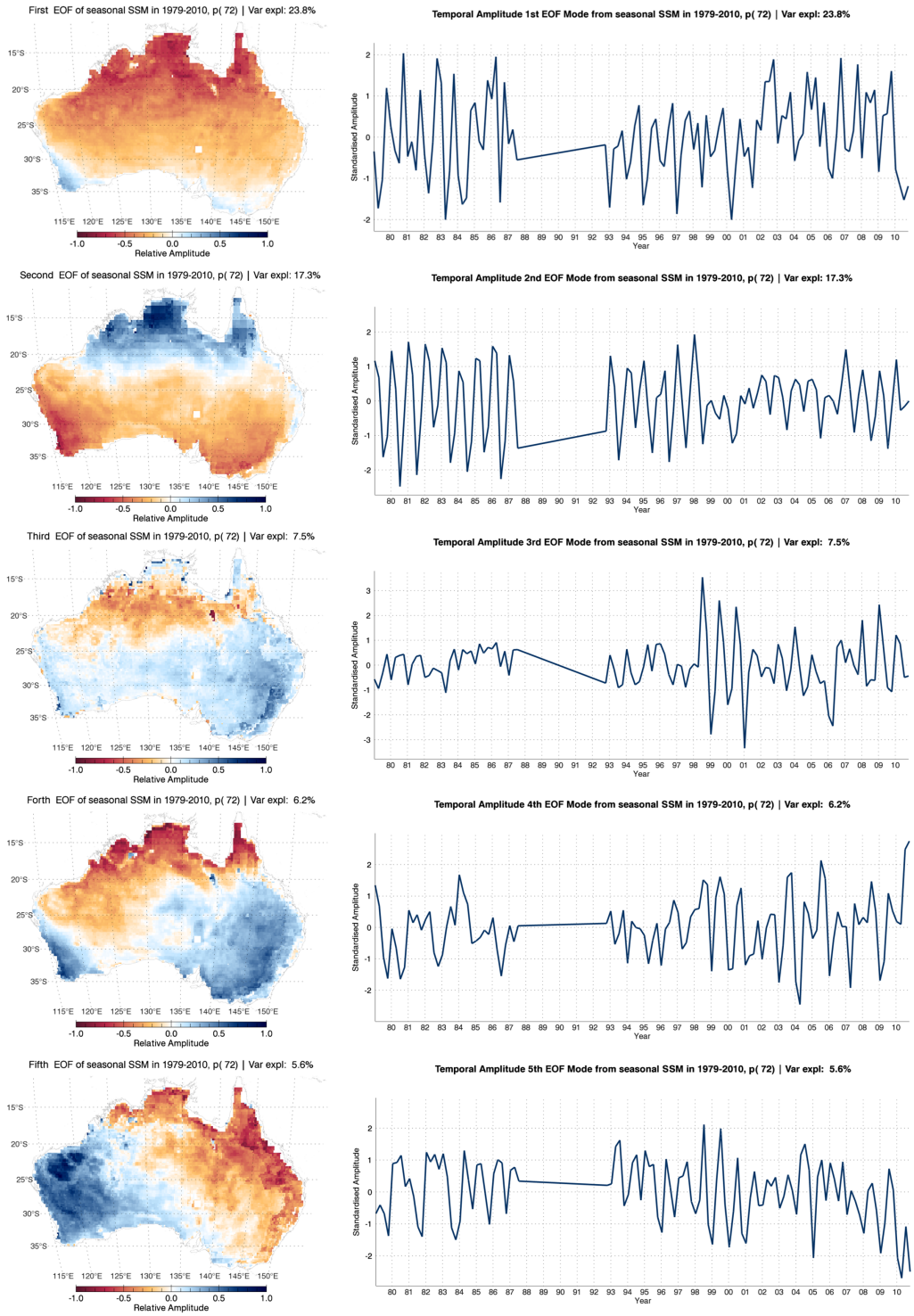

Figure 5.8: *WACMOS SSM 1979-2010: Spatial amplitude (EOFs, left) and temporal amplitude (PCs, right) for the first five modes. The SSM/I-period is muted out. Discussed in the text above.*

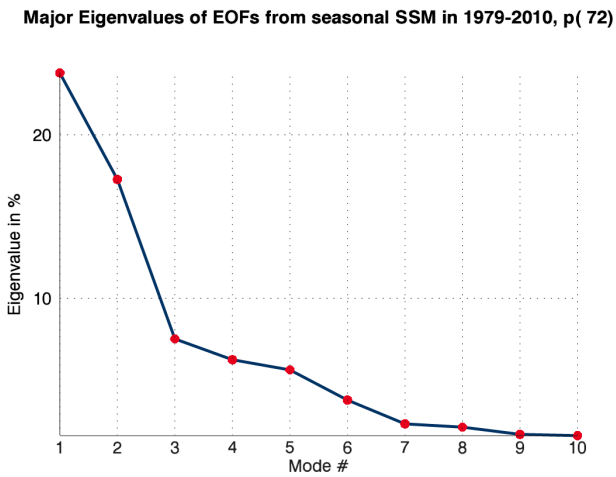

Figure 5.9: *The graph shows the eigenvalues of the first ten modes of the EOF analysis displayed in Figure 5.8 in percent of total variance in $X(t,s)$. As one can see, the modes' eigenvalues decrease rapidly with their rank; the fifth mode represents ("explains") only 5.6%. The first both modes are clearly distinguishable, whereas the modes 3-5 can not be separated.*

Mode	Variance	SOI	SAMI	IODMI	F10.7
	%	Spearnman R in %			
I	23.8	-23^{*}	-25^{**}	–	–
II	17.3	–	–	–	–
III	7.5	$+32^{**}$	$+23^{*}$	–	–
IV	6.2	–	–	–	–
V	5.6	-49^{**}	-33^{**}	–	–

Table 5.1: *Spearman correlation coefficients of WACMOS PCs and climate mode indices and Solar Flux in % for the period 1979-2010. XX^{*} donates for significant ($p < 0.05$) and XX^{**} for high significant correlation ($p < 0.01$) (two-sided significance test). For the sake of clarity, absolute coefficients below 20 or with significance below 0.1 ($p > 0.10$) are neglected. The modes' share in total variance is also displayed.*

- IOD and Solar Flux F10.7 do not feature any (significant) relationship. From the remote sensing perspective, the latter is expected but not so for the IOD.
- Modes 2 and 4 seem not related to climate modes, which is easily explained for the second mode (annual ITC movement), but not so for the forth. Factors driving SSM variation explained by mode 4 need to be detected. IOD is a candidate, since the pattern is negative towards the Indian Ocean and negative IODMI values are related to increased rainfall over these areas.
- ENSO and SAM follow the same patterns all over the observation period. In modes 1 and 3 a weak, but significant relation is measured. For mode 5 that is representing 5.6% of total variance, relatively high correlation between SAMI and especially SOI is observed. Here, also the spatial pattern can is well-grounded by ENSO, with strong amplitude towards the Pacific Ocean.

Indeed, focusing on the last point above, the nature of ENSO and SAM can explain the observed patterns:

1. For modes 1 and 5 the coefficients for SOI and SAMI are negative, meaning if SOI or SAMI goes up, EOF 1 goes down. However, EOF 1 is overwhelming negative and thus, if the indices goes up, SSM also goes up ($-1\times-1\times+1 = 1$), which perfectly fits to theory as elaborated in Section 2.2. This holds also for SAM, considering that most rainfall in southern Australia fell during autumn and winter season.
2. The same is valid for mode 5 but with even higher correlations. Also the spatial structure of EOF 5 can be recognized as typical ENSO impact area. Furthermore, the negative peaks in 2005 and 2010 align perfectly with positive peaks in the SOI time series (Figure 2.4).
3. Mode 3 is positive in the south and east, which coincide as well with the area of influence for SAM and ENSO, respectively.

5.3.2 EOF Seasonal Decomposition 1979-2010

In order to investigate the seasonal behaviour of WACMOS SSM over Australia, a second EOF decomposition was applied to the WACMOS data: The original times series have been split into four parts, each for summer, autumn, winter and spring (DJF, MAM, JJA and SON). The maximum sample size at each location reduces from 128 to 32 then. Again, the SSM/I period is muted out and minimum sample size per location is 20. The next four figures present SSM modes 1 to 4 of each season. Also four tables containing the Spearman Coefficients between seasonal SSM and seasonal climate indices are given.

Summer - DJF Figure 5.10 along with Table 5.2 prove many theoretical considerations regarding climate modes and their impact on Australian hydrology: First of all, SAMI positively correlates with all modes, which is expect by theory for this season. For ENSO, spatial patterns with high amplitude in the north and east fit well to theory. IOD shows some positive correlation with the mode 1, evoking questions on the sign of the relationship since a negative correlation is expected. For Solar Flux, weaker, negative correlations are experienced throughout the modes at a same level. For the best-correlating mode 4, the coastal areas in the southern part of Australia are pronounced.

Autumn - MAM Figure 5.11 and Table 5.3 describe the SSM situation in autumn (MAM) from 1979 to 2010. Regarding the correlation coefficients, mode 1 and 4 seem to describe the same phenomenon and the same can be said for mode 2 and 3. The for climate modes typical patterns and signs can be recognised in the maps: Mode 2 and 3 correlate positively with SOI and they are positive themselves in the northern and eastern part towards the Pacific Ocean. The forth mode is positive in the west and correlates negatively with IODMI, which is explained well by theory. However, although the spatial patterns of EOF 1 and 4 coincide with impact areas of IOD and SAM, their signs only fulfil the expectation for the IOD in mode 4: Here, negative correlation between IODMI and positive SSM variance is supported by general theory.

Winter - JJA Regarding the winter time series (Figure 5.12 and Table 5.4), the major mode is not affected by climate mode or solar activity and is quite homogeneous. On other hand, mode 2 fits well to known impact of ENSO since the negative east part of the pattern is relatively highly correlated with the SOI. Also SSM mode 3 accords to theory regarding the negative correlation with IODMI and the outstanding positive pattern in western Australia off the Indian Ocean. Mode 4 shows the complete same behaviour concerning F10.7 as mode 4 from the summer time series (same correlation and same EOF pattern).

Spring - SON The spring season is examined in Figure 5.13 and Table 5.5. Concerning climate modes, the spring EOFs and correlations follow well the theory: SAMI correlates positively with positively SSM anomalies captured by the north-weighted mode 1. For mode 2 and 4, the negative EOF patterns in the east and south verify the observation, that SAM is linked to precipitation in these regions during spring. SOI shows a strong inverse relation to negative SSM anomalies in the east explained by modes 2, 3 and 4. Similarly, IODMI correlates negatively with mode 3 that is positive in the south and west. The hypothesis of some relationship between Solar Flux and coastal areas in Australia is strengthened by the patter in mode 3. As in summer mode 4 and winter mode 4, locations close to the coast all around Australia show higher amplitudes. For all these cases, F10.7 shows notable correlation coefficients.

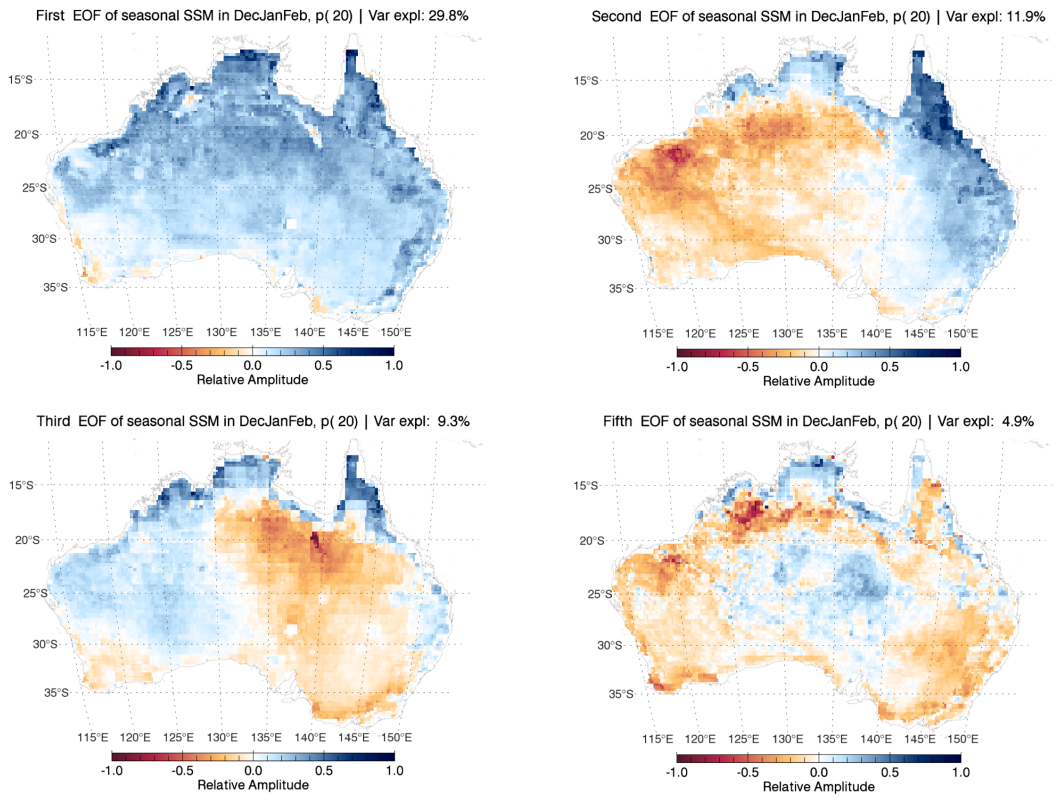

Figure 5.10: *The maps depict the SSM modes 1 to 4 for summer (DJF). The first EOF (representing 29.9% of total variance) is almost entirely positive whereas the second EOF (11.9%) shows a clear east to west gradient. Mode 3 (9.3%) graduates inversely, but not in the north. Mode 4 (5.5%) is positive in the center and the far north and negative in the west, east and inner north.*

Mode	Variance	SOI	SAMI	IODMI	F10.7
	%	Spearnman R in %			
I	29.8	+37*	+82**	+39*	−36
II	11.9	+49**	+50**	–	−35
III	9.3	+57**	+70**	–	−38
IV	4.9	+58**	+53**	–	−45*

Table 5.2: *Same as for Table 5.1 but for summer season (DJF) only. High correlation with SSM is evident for SOI and SAM in all modes, featuring exceptional values for SAM. Also IODMI shows correlation with the first mode. Solar Flux seems to be negative correlated for this season.*

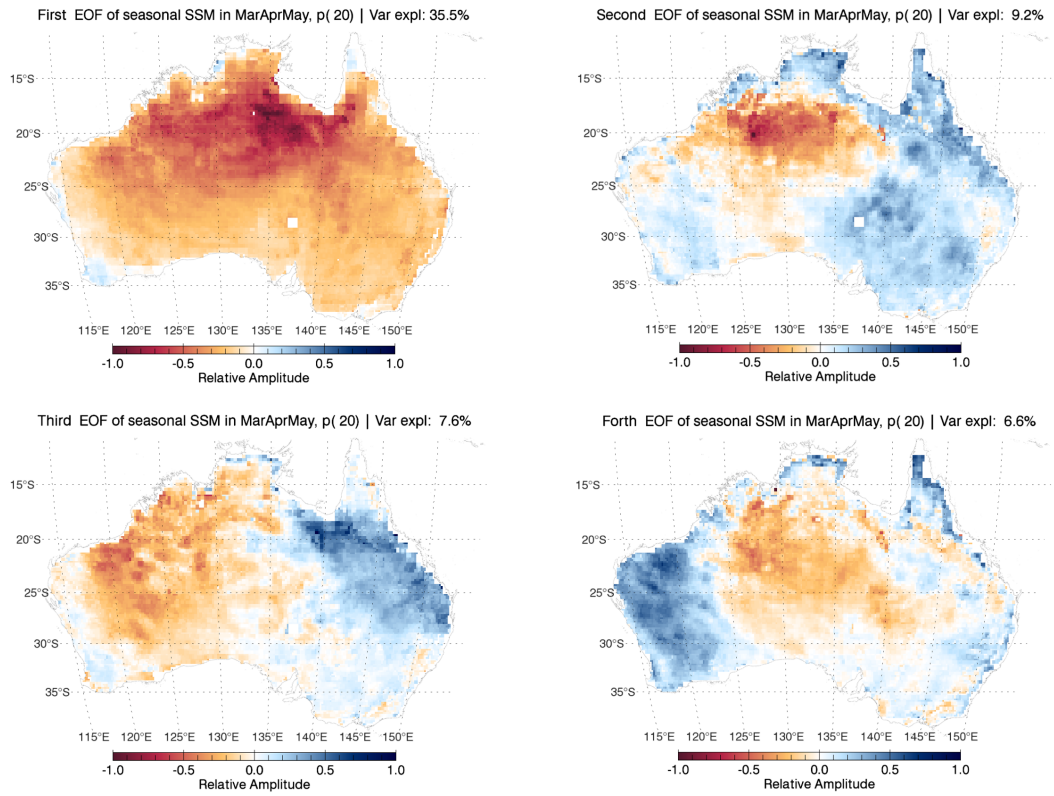

Figure 5.11: *Same as for Figure 5.10 but for autumn (MAM). The first mode (35.5% of total variance) describes quite uniformly a continent-wide structure in the SSM variance in MAM. Mode 2 (9.2%) depicts a clear spot north-east of the center whereas mode 3 (7.6%) shows an east-west gradient. An Indian-Ocean component can be seen in the forth mode (6.6%).*

Mode	Variance	SOI	SAMI	IODMI	F10.7
	%	Spearnman R in %			
I	35.5	–	-35^{**}	-35^{**}	–
II	9.2	$+63^{**}$	–	–	–
III	7.6	$+39^{**}$	–	–	–
IV	6.6	–	$+43^{*}$	-45^{**}	–

Table 5.3: *Same as for Table 5.2 but for autumn (MAM). Negative correlation for SAMI and IODMI with mode 1 and 4. Strong relation for SOI and the second mode and weaker connection to the third mode.*

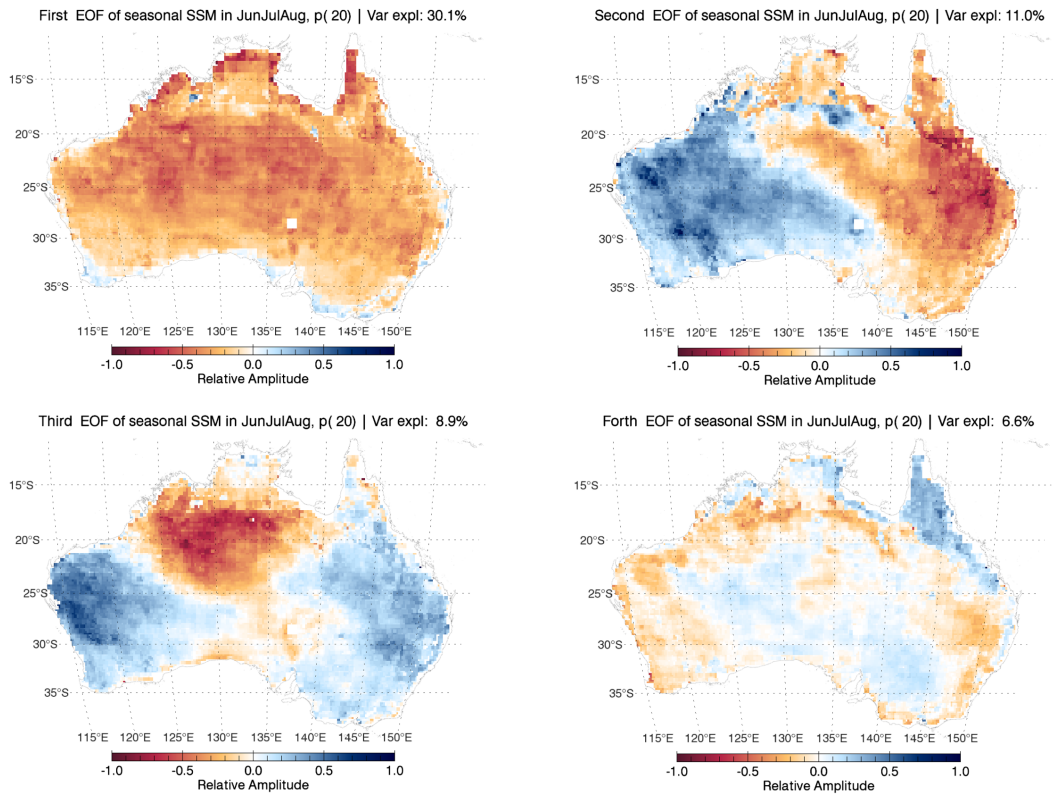

Figure 5.12: *Same as for Figure 5.10 but for winter (JJA). The first mode (representing 30.1% of total variance) features a uniform, continent-wide structure. In contrast, mode 2 (11.0%) obviously contains a gradient from west to east. Mode 3 (8.9%) depicts a amplitude that starts positive in the west, evolves negatively in the center and swings back to positive in the east. The forth mode (6.6%) is shows great similarity to the forth mode in MAM.*

Mode	Variance	SOI	SAMI	IODMI	F10.7
	%	Spearnman R in %			
I	30.1	–	–	–	–
II	11.0	−39**	–	–	–
III	8.9	–	–	−49**	–
IV	6.6	–	–	–	+47*

Table 5.4: *Same as for Table 5.2 but for winter (JJA). Few significant correlation has been found for these time series: SOI negatively with mode 2, the IODMI also negatively with mode 3 and F10.7 positively with mode 4.*

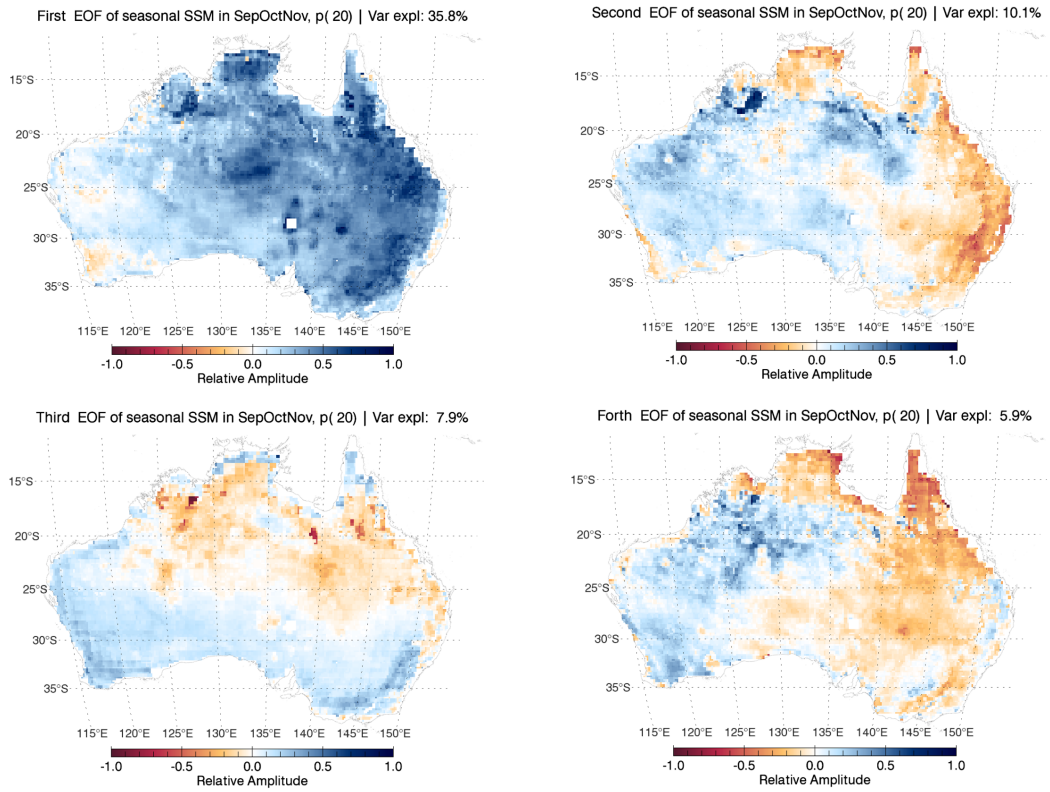

Figure 5.13: *Same as for Figure 5.10 but for spring (SON). Mode 1 (Var.: 35.8%) decreases from east to west whereas modes 2 (10.1%), 3 (7.9%) and 4 (5.9%) graduate from south-west to north-east.*

Mode	Variance	SOI	SAMI	IODMI	F10.7
	%	Spearnman R in %			
I	35.8	–	+34	–	–
II	10.1	−56**	−41*	–	–
III	7.9	−34	–	−41**	+50**
IV	5.9	−62**	−41**	–	–

Table 5.5: *Same as for Table 5.2 but for spring (SON). SAMI plays a role in mode 1, SOI drives mode 2, 3 and 4. The latter is also in relationship with the IOD. Solar Flux can not be neglected in the third mode.*

5.3.3 EOFs from Time Series 1998-2010

When the EOF method is applied to WACMOS SSM from 1998 to 2010 same general patterns in the modes were found. However, while in the 1979-2010 analysis no strong impact of the IOD is apparent, in the 1998-2010 analysis a eminent influence by the IOD is obvious. Simultaneously, overall correlation of SOI and SAMI with SSM anomaly modes is on a same level as for 1979-2010. A selection of the most important findings is presented below in Table 5.6 and Figure 5.14 and they reveal clearly the impact of climate modes: In Figure 5.14, the left column tells that the connection of ENSO with SON 1, MAM 1 and JJA 1 is striking with continent-wide impact and outstandingly high correlation values. This holds in reduced manner for the second mode of the complete time series (ALL 2), where SAM is also a notable driver. In general, smoother and more uniform patterns manifest in the EOF maps of the shorter SSM time series. In the right column, the influence of IOD on SSM in western Australia is evident since IODMI is highly negatively correlated with positive SSM anomalies (or vice-versa) in all four cases.
The study published in (Liu et al., 2007) investigated the same phenomena and the results are in good accordance.

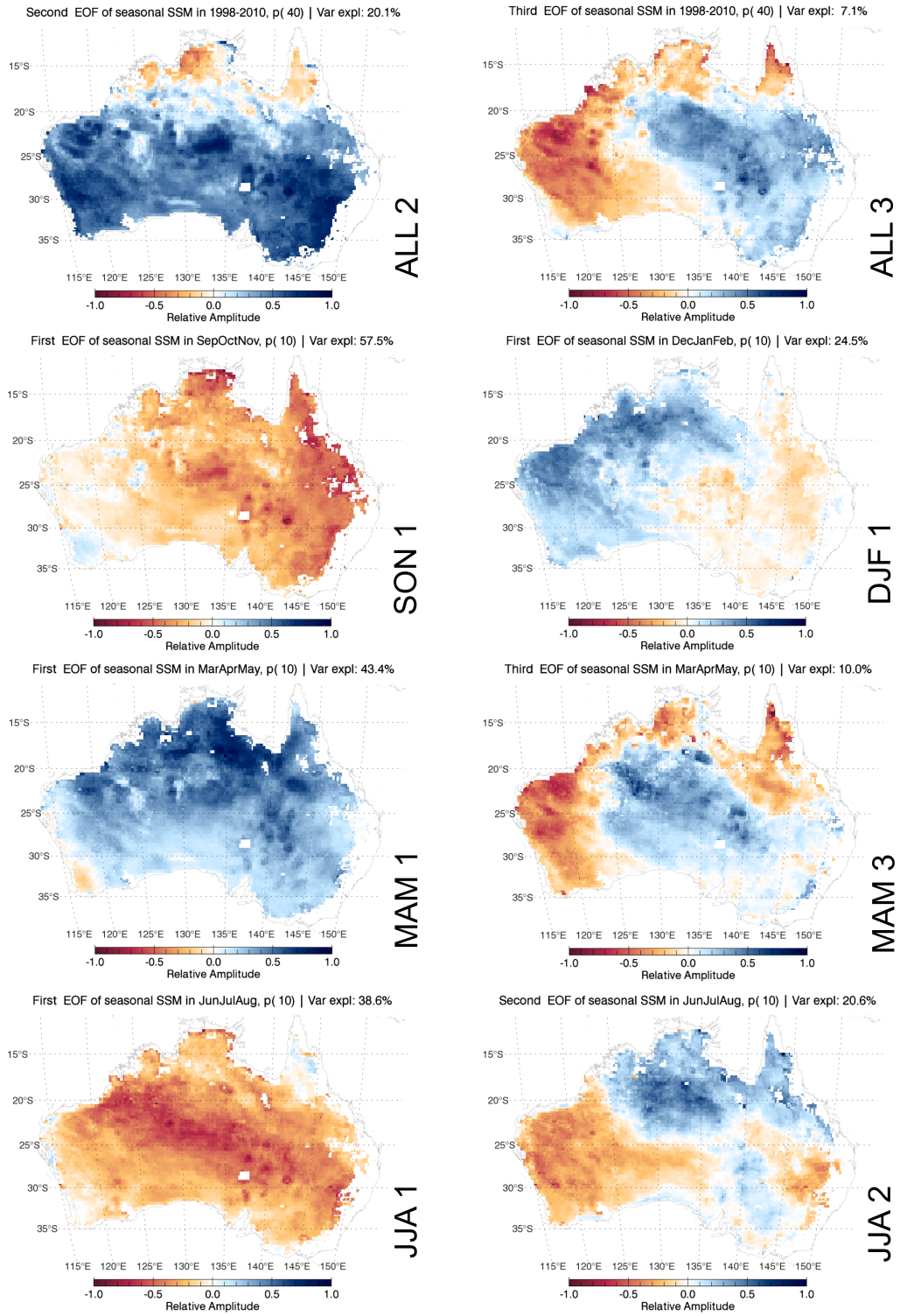

Figure 5.14: *This arrangement depicts EOFs of SSM data from 1998-2010: 2nd and 3rd mode of complete series in the 1st row and seasonal modes (rank according to numbers aside the graphics) below.*

Mode		Variance	SOI	SAMI	IODMI	F10.7
		%	Spearnman R in %			
ALL	**I**	38.0	-36^{**}	–	–	–
	II	20.1	$+45^{**}$	$+49^{**}$	–	–
	III	7.1	–	–	$+30^{*}$	-29^{*}
	IV	5.8	-42^{**}	-29^{*}	–	$+49^{**}$
	V	3.6	–	$+24^{*}$	–	–
DJF	**I**	24.5	$+66^{**}$	–	-67^{**}	+47
	II	16.5	–	-61^{*}	–	$+58^{*}$
	III	13.3	–	–	–	–
	IV	9.7	–	–	–	–
	V	6.8	$+84^{**}$	$+60^{*}$	–	–
MAM	**I**	43.4	$+86^{**}$	–	–	–
	II	12.2	–	–	-62^{*}	$+63^{*}$
	III	10.0	–	–	$+73^{**}$	–
	IV	9.0	–	-53^{*}	-53^{*}	–
	V	5.7	–	–	–	$+58^{*}$
JJA	**I**	38.6	-66^{**}	-54^{**}	–	–
	II	20.6	–	–	$+71^{**}$	-62^{*}
	III	11.2	$+74^{**}$	+50	–	-72^{**}
	IV	5.5	–	–	–	–
	V	4.4	–	–	–	–
SON	**I**	57.5	-91^{**}	-63^{**}	–	–
	II	8.8	–	–	-66^{**}	–
	III	6.0	-68^{**}	-76^{**}	–	$+63^{*}$
	IV	4.5	–	–	–	$+77^{**}$
	V	4.0	–	–	–	–

Table 5.6: *This table lists all major EOF modes of the 1998-2010 dataset. For the complete time series analysis the notation "ALL" is used. The share on total variance is listed as well as the Spearman coefficients (scaled by 100). Modes highlighted in gray are presented in Figure 5.14.*

5.4 CEOF Analyses

Analogical to EOF analyses above, CEOF analyses were applied to the WACMOS SSM anomaly field over Australia. Similar data truncation settings as above have been chosen. Contrary to non-complex analyses, only the full-time data was investigated (no separate seasonal decomposition) since the phase information is poor in case of only one observation per year. On the next pages, the first three CEOF modes comprising 70.8% of total variance (spatial and temporal) in WACMOS SSM from 1979 to 2010 are presented:

5.4.1 CEOFs from Time Series 1979-2010

1st Mode Figure 5.15 presents the characteristics of the first mode which representing 47.1% of total variance in the SSM data. This value is notably higher than for the first EOF mode. This accounts for fact that they carry different information: CEOF modes also contain information about the observations' temporal relationship and therefore the results allow a different view on the data. Also the spatial pattern in Figure 5.15 a) differs from the EOF mode: Here, the majority of variance covered by the first mode is located at the (predominantly wet) northern and south-western edge of the continent.

The spatial phase in Figure 5.15 b) together with the temporal phase in Figure 5.15 d) reflect the propagating nature of the pattern: It is a clear annual signal what is demonstrated by one phase revolution per year in the phase graph in Figure 5.15 d) (with 0° = 360°). This is bound to the spatial phase in Figure 5.15 b), where one can see a propagation from north to south during one cycle (which is a year in this case). Keeping in mind that at the beginning of the year (exactly: at 15th of January) the phase is zero degrees (or 360) and that a year has 365 days, one can see that maximum amplitude is reached in the north around February-March and in the south in August-September. This is in perfect accordance with the general rainfall pattern of Australia as shown in Figure 2.11. The irregular positive peaks in the phase graph stem from small delays in the annual cycle.

The temporal amplitude, which contains the same kind of information as the temporal amplitude of an EOF mode, is shown in Figure 5.15 c). The graph shows three distinct negative peaks in 2002, 2005 and 2010. Concerning climate indices, 2002 featured very low values of SAMI and an 11-year-high of F10.7. In 2005, both IODMI and SOI show highly negative values. In 2010, SOI values were outstandingly high.

2nd Mode In Figure 5.16 the second mode is presented, which contains 17.8% of total variance. The central parts off the coasts are captured by the spatial amplitude in Figure 5.16 a). The

propagation in Figure 5.16 b) is from south to north with a phase jump at around 17° south. But contrary to the first mode, the signal is not annual and rather difficult to interpret as can be seen in Figure 5.16 d). On average, it takes two years to complete one revolution, so the assumption of a two-year-period is possible.

3rd Mode In Figure 5.17 the third mode is presented, which contains 5.9% of total variance. The spatial amplitude map in Figure 5.17 a) shows a strong impact of this mode in the north-eastern and north-western regions whereas the spatial phase map displays a distinct movement from east to west per cycle. The cycle-length is clearly multi-annual with periods from 3-6 years, what can be inferred from the red circles representing each January value. The spatial pattern in phase and amplitude as well as the temporal phase and amplitude of mode 3 suggest a connection to ENSO: The east-west character refer to typical ENSO impact areas and the peaks in Figure 5.17 c) coincide with peaks in the SOI graph. The multi-year-cycle is also in accordance with the nature of ENSO.

These modes are set into relation with climate modes as it was done for the EOF modes and the results can be seen in Table 5.7. The first mode, that explains half of total variance, is connected to all climate indices and Solar Flux. The signs of the coefficients for SOI and IODMI confirm expectations based on theory. This holds also for SAM, keeping in mind that for summer season SSM and SAMI are positively correlated and that in the north, where the first mode has its highest amplitude, the majority of precipitation falls in summer. The latter can be seen in Figure 2.11 as well as in Figure 5.15. However, mode 3 does not show any connection to IOD or ENSO, although the obvious east-west pattern and the multi-annual character discussed above would lead to this assumption. Future research should investigate why here only low or insignificant correlations is found.

Mode	Variance	SOI	SAMI	IODMI	F10.7
	%	Spearnman R in %			
I	47.1	$+32^{**}$	$+27^{**}$	-20^{**}	-22^{*}
II	17.8	$+21^{*}$	–	–	–
III	5.9	–	–	–	–

Table 5.7: *The table shows the Spearman correlation coefficient between the CEOF modes 1-3 presented above and climate indices. The first mode is weakly, but significantly correlated with all climate indices and solar activity. The second mode shows some connection with ENSO but not all with the other phenomena.*

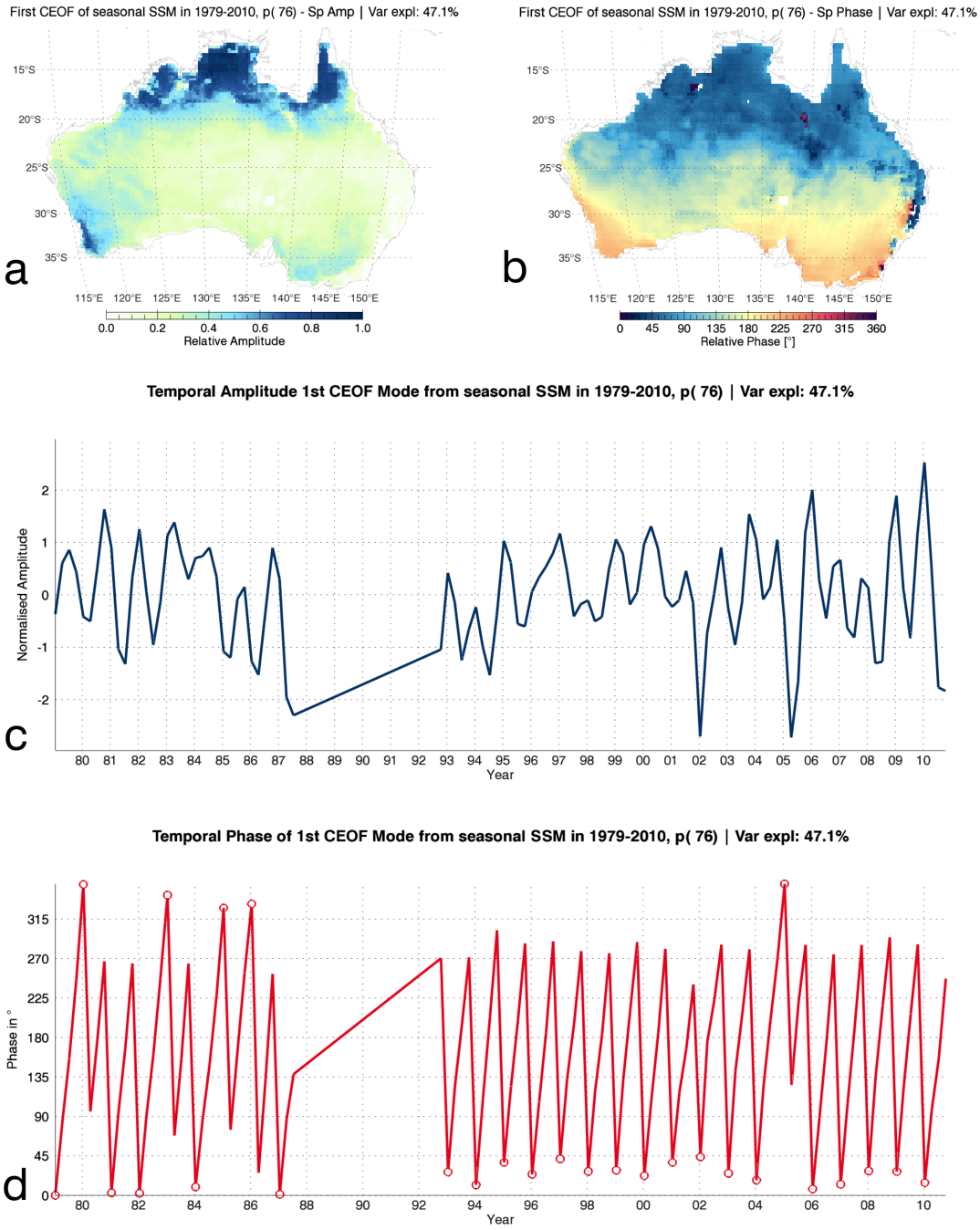

Figure 5.15: *This arrangement displays the first mode (47.1% of variance) of the WACMOS data from 1979 to 2010 extracted by a CEOF decomposition. The figures show in a) the spatial amplitude (range: [0,1]), in b) the spatial phase (range: [0,360]), in c) the temporal amplitude (normalised) and in d) the temporal phase (range: [0,360]). Each January is marked by red circles. Discussion in the text.*

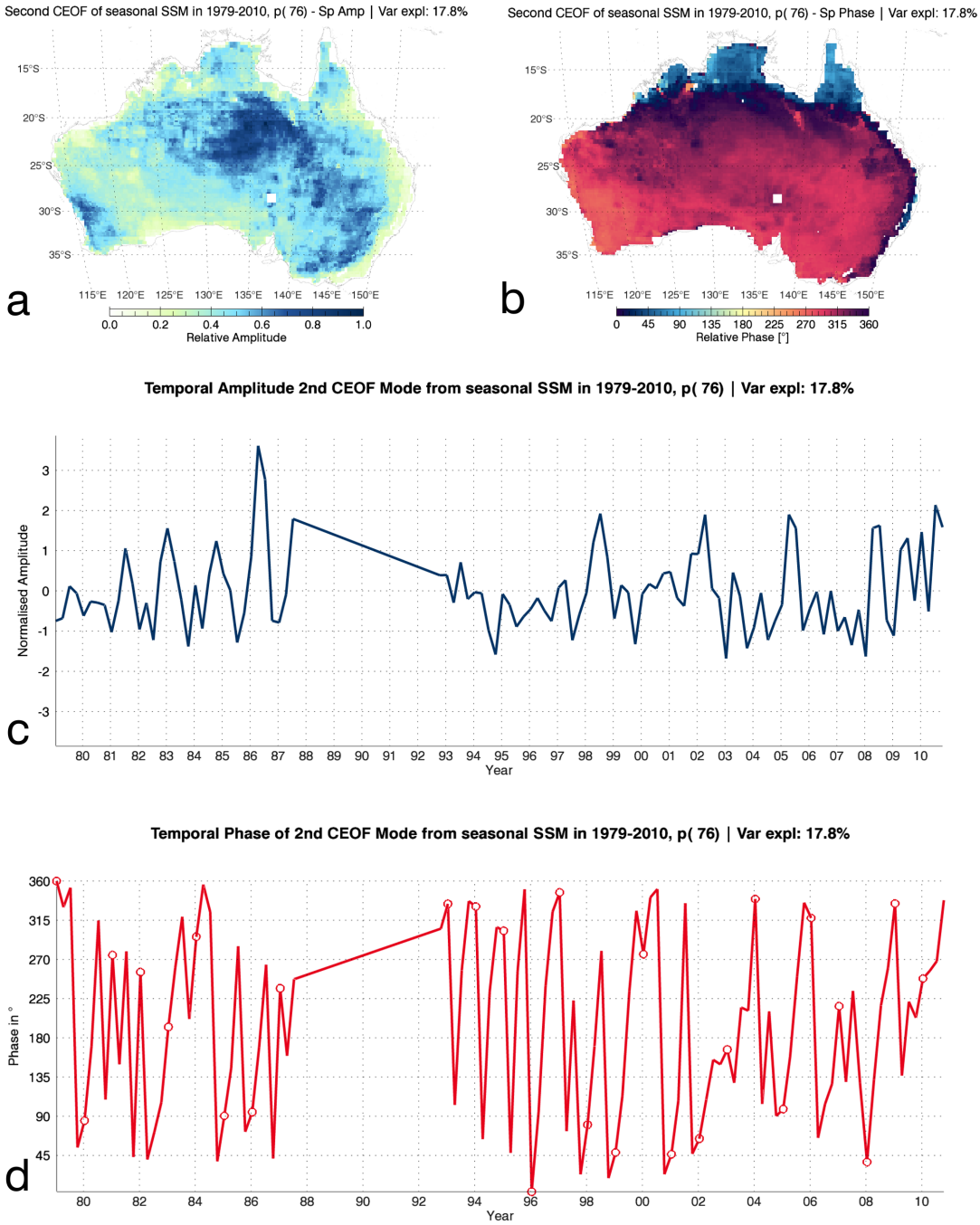

Figure 5.16: *Same as for Figure 5.15 but for the second mode.*

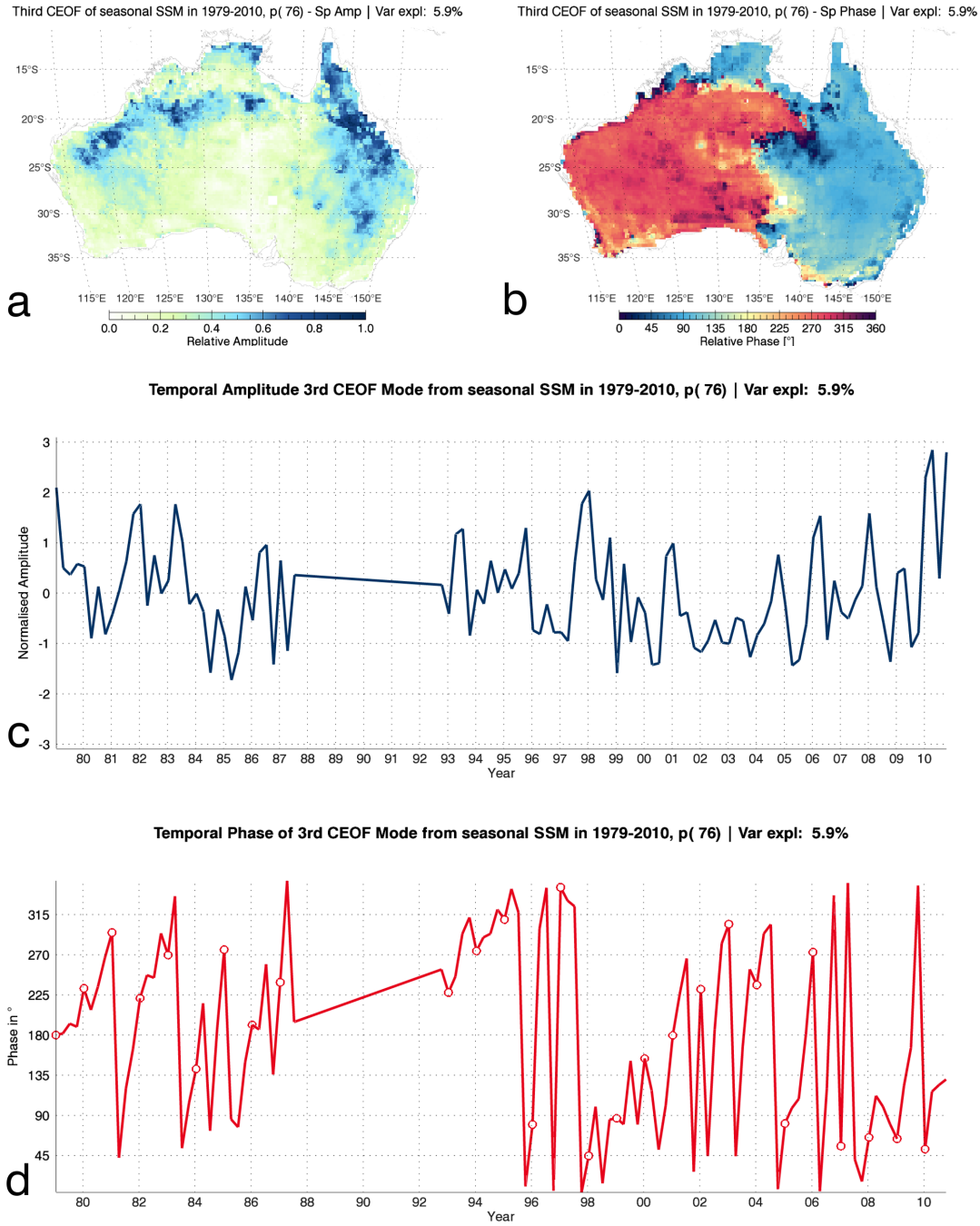

Figure 5.17: *Same as for Figure 5.15 but for the third mode.*

5.4.2 CEOFs from Time Series 1998-2010

In order to demonstrate the temporal stability of the CEOF analysis from above, the same decomposition was done for the period DJF 1998 to SON 2010. This period excels in superior performance of the WACMOS SSM due the to the beneficial satellite configuration as can be seen in Figure 4.1. Furthermore, the results (displayed in Figure 5.18) can be easily compared to the findings of (Garcia-Garcia et al., 2011), who is applying a CEOF decomposition to water mass variations of Australia derived from GRACE gravity anomaly data. The analysis in the article is in great accordance with the results of the CEOF analysis carried out in this study.

Only the first CEOF mode is depicted since for the lower ranked modes the same parallels between CEOFS of SSM 1979-2010 and 1998-2010 were found. Concerning the Spearman correlation coefficients, comparable values account for the rather stable relationships between the CEOF modes and climate indices (Table 5.8). However, the correlation coefficients for 1998-2010 are higher than for the long period. While SOI, SAM and IOD show stronger connection to SSM variations than for 1979-2010, F10.7 does not show a relation anymore.
The higher temporal stability of the CEOF analysis compared to the EOF method can explained by the greater amount of information on the investigated process. The inclusion of timely relationship of the observations leads to major modes that represent a bigger share in total variance (in space and time). Consequently, the characteristics of major CEOF modes are more pronounced and they tend to be more stable regarding varying analysis periods. This is manifest in the comparison of the CEOF analyses of 1979-2010 and 1998-2010.

Mode	**Variance**	**SOI**	**SAMI**	**IODMI**	**F10.7**
	%	Spearnman R in %			
I	51.5	$+52^{**}$	$+40^{**}$	-50^{**}	–
II	20.0	–	–	–	–
III	6.9	–	$+30^{*}$	–	–

Table 5.8: *The table shows the Spearman correlation coefficient between the CEOF modes 1-3 from 1998-2010 and climate indices.*

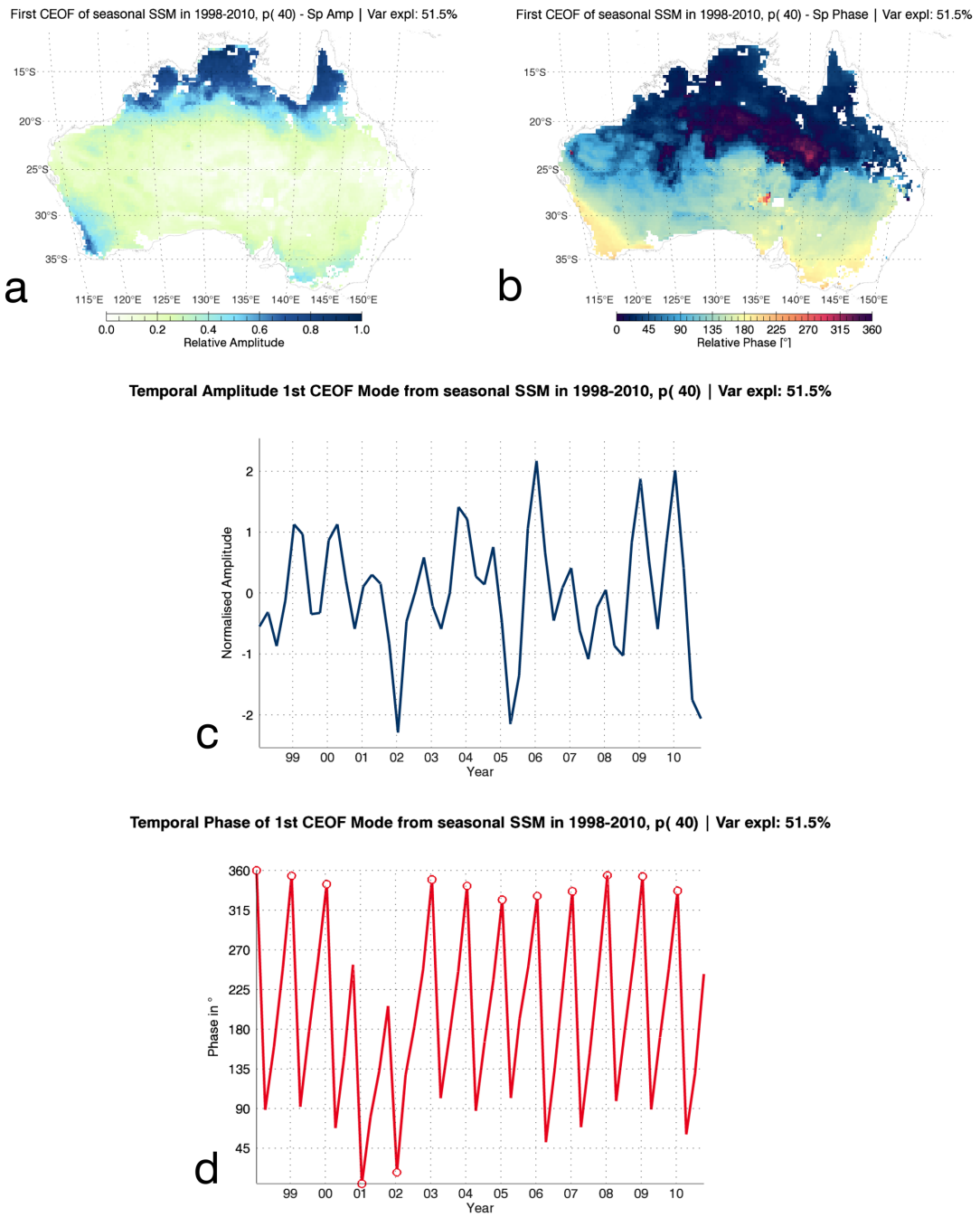

Figure 5.18: *Characteristics of the first complex mode of WACMOS SSM from SON 1998 to DJF 2010. All graphics confirm the insights from the CEOF analysis of SSM over the period 1979-2010. The spatial amplitude in a) is identical to its corresponding CEOF of SSM from 1979 to 2010 (except for the data gaps in the east). The same holds for the temporal amplitude in c). The spatial phase map in b) shows slightly earlier dates of maximum amplitude all over Australia than in Figure 5.15. In d), the annual signal is even clearer compared to the first CEOF 1979-2010.*

Chapter 6

Conclusion

Da steh ich nun, ich armer Tor! Und bin so klug als wie zuvor.

Goethe's Faust

No, no, our dear Faust has learned many things: He has learned how global atmospheric and oceanic circulations interact with each other and influence the climate of the continents. He has learned about the nature of climate modes and how they alter general precipitation patterns. Then he discovered the hydrological conditions of the Australian continent and its integration into surrounding climate systems. He got to know what solar activity is and how it can be observed. He found out about the essential climate variable soil moisture and how spaceborne microwave remote sensing can be utilized for its measurement. He learned about the WACMOS project and its surface soil moisture dataset for the period from 1978 to 2010. As next, our Faust got introduced to the multivariate statistical technique of EOF analysis and also learned about the complex EOF decomposition using the Hilbert transforms of the time series. Finally, he got to know the basics of correlation measures.

This study offered an insight in the spatio-temporal characteristics of surface soil moisture in Australia over the last three decades and also investigated the relationship to "neighbouring" climate modes that affect the entire planet. One big part of the work on this study was to handle the big amount of data and to extract handy information about the behaviour of Australian SSM conditions. Both in space and time, the WACMOS data gives huge amount of SSM values since it covers almost the Earth's entire landmasses and comprises data starting in 1978. The long duration in the dimension of a CLINO allows examination of climatic parameters. Therefore, also the influence of solar activity is examined, but however, the main focus lies on the impact of climate drives as ENSO, IOD or SAM on Australia's hydrology. The statistical tool EOF analysis was chosen due to its capability of clever data compression and extraction of independent factors.

Spearman correlation was opted because of its robustness and its independence on distribution presumptions.

The resampled WACMOS SSM data has proven its capability to reflect soil moisture conditions over Australia. The continent has a predominantly arid and semi-arid character and thus it is an ideal test bed for soil moisture retrieval with microwave remote sensing systems. The wide absence of dense vegetation lessens the sensors' and algorithms' inadequateness.

The EOF technique has shown that it is a useful tool to brake down a diversified dataset into distinguishable modes and allows therefore separate investigation of these inherent factors. Relationships of ENSO and SAM have been found for the complete observation period, especially in the eastern and northern parts of Australia. The results evoke some conflicts with theory, but in summary, many of theoretical assumptions are confirmed and results are supported by previous research. In particular, during summer and spring season the impact of SOI and SAM is significant and the relationship remains of the temporal scale is varied. This holds not for the impact IOD, which only can be measured well in the shorter period 1998-2010. It is an open question, if this is caused by real changes in the physical processes or by the higher quality of the satellite data.

The complex EOF analysis has shed light on the propagating nature of SSM conditions over Australia and the findings are in perfect accordance with previous studies and hydrological characteristics of the continent. The technique's ability to reflect propagating oscillations has been demonstrated and thus allows not only to find *where* but also *when* is much variation.

Due to the focused character of this master thesis, several additional experiments are still subject of future research. One suggestion is to make use of *rotated EOFs* which sacrifice orthogonality to gain more distinct, clear patterns with higher contrast in amplitudes. An other topic is the *degeneracy* of EOFs that is describing the relevance of lower ranked modes. Concerning correlation analysis, time shifts can be introduced to examine if climate indices affect SSM with a certain lag. This would facilitate rough but solid forecasts on the basis of easily (and cheap) determinable climate indices. Also, the quality of the input data is inspected only superficially and since it is (partially) highly varying in space and time, special effort may improve future results.

However, the thesis closes with the insight that the climate modes do have significant impact on Australia's soil moisture and that the WACMOS SSM is a valuable long-term dataset. Furthermore, the spatial and temporal patterns have been detected as well as the amplitude of the climate modes' influence. Regarding solar radiation, no clear relationship has been found. Only a fragile hypothesis concerning effects appearing close to Australia's coasts can be proposed. SSM variations at areas close to the oceans seem to be positively correlated with solar activity.

Bibliography

Benestad, R. (2006). *Solar activity and earth's climate*. Springer Praxis Books / Environmental Sciences Series. Springer. 2, 3, 4, 16

Bouzinac, C., J. Vazquez, and J. Font (1998). Complex empirical orthogonal functions analysis of ers-1 and topex/poseidon combined altimetric data in the region of the algerian current. *Journal of Geophysical Research 103 C4*, 8059–8071. 50

Chiew, F. H. S., T. C. Piechota, J. A. Dracup, and T. A. McMahon (1998). El nino southern oscillation and australian rainfall, streamflow and drought: Links and potential for forecasting. *Journal of Hydrology 204*(1–4), 138–149. 9, 59

Chow, V.T.; Maidment, D. M. L. (1988). *Applied hydrology*. McGraw-Hill Inc. 22, 23

de Jeu, R. A. M., W. Wagner, T. R. H. Holmes, A. J. Dolman, N. C. van de Giesen, and J. Friesen (2008). Global soil moisture patterns observed by space borne microwave radiometers and scatterometers. *Surveys in Geophysics 29*, 399–420. 23, 31, 33

Dorigo, W. A., K. Scipal, R. M. Parinussa, Y. Y. Liu, W. Wagner, R. A. M. de Jeu, and V. Naeimi (2010). Error characterisation of global active and passive microwave soil moisture datasets. *Hydrology and Earth System Sciences 14*(12), 2605–2616. 38

Esquivel, P. and A. Messina (2008). Complex empirical orthogonal function analysis of wide–area system dynamics. *Power and Energy Society General Meeting - Conversion and Delivery of Electrical Energy in the 21st Century, 2008 IEEE*. 46, 49

Garcia-Garcia, D., C. C. Ummenhofer, and V. Zlotnicki (2011). Australian water mass variations from grace data linked to indo-pacific climate variability. *Remote Sensing of Environment 115*, 2175–2183. 80

Gerten, D., S. Schaphoff, and W. Lucht (2007). Potential future changes in water limitations of the terrestrial biosphere. *Climatic Change 80*(3–4), 277–299. 6

Gong, D. and S. Wang (1999). Definition of antarctic oscillation index. *Geophys. Res. Lett. 26*, 459–462. 14

Gray, L., J. Beer, M. Geller, J. Haigh, M. Lockwood, K. Matthes, U. Cubasch, D. Fleitmann, G. Harrison, L. Hood, J. Luterbacher, G. Meehl, D. Shindell, B. van Geel, and W. White (2010). Solar influences on climate. *Rev. Geophys. 48*. 15

Hannachi, A., I. T. Jolliffe, and D. B. Stephenson (2007). Empirical orthogonal functions and related techniques in atmospheric science: A review. *International Journal of Climatology 27*(9), 1119–1152. 40, 41, 42, 46, 49, 50

Hannachi, A., I. T. Jolliffe, D. B. Stephenson, and N. Trendafilov (2006). In search of simple structures in climate: Simplifying eofs. *International Journal of Climatology 26*(1), 7–28. 43, 52

Hendon, H. H., D. W. J. Thompson, and M. C. Wheeler (2007). Australian rainfall and surface temperature variations associated with the southern hemisphere annular mode. *Journal of Climate 20*(11), 2452–2467. 14

Ho, M., A. S. Kiem, and D. C. Verdon-Kidd (2011). The southern annular mode: a comparison of indices. *Hydrology and Earth System Sciences Discussions 8*(4), 7461–7498. 13, 14

Ineson, S., A. A. Scaife, J. R. Knight, J. C. Manners, N. J. Dunstone, L. J. Gray, and J. D. Haigh (2011). Solar forcing of winter climate variability in the northern hemisphere. *Nature Geoscience 4*, 753–757. 15

Isbell, R. (2002). *The Australian soil classification*. Australian soil and land survey handbook. CSIRO Pub. 21

Johnson, D. (2004). *The geology of Australia*. Cambridge University Press. 18, 21

Jung, M., M. Reichstein, P. Ciais, S. I. Seneviratne, J. Sheffield, M. L. Goulden, G. Bonan, A. Cescatti, J. Chen, R. De Jeu, and et al. (2010). Recent decline in the global land evapotranspiration trend due to limited moisture supply. *Nature 467*(7318), 951–4. 6

Koster, R. D., P. A. Dirmeyer, Z. Guo, G. Bonan, E. Chan, P. Cox, C. T. Gordon, S. Kanae, E. Kowalczyk, D. Lawrence, P. Liu, C.-H. Lu, S. Malyshev, B. McAvaney, K. Mitchell, D. Mocko, T. Oki, K. Oleson, A. Pitman, Y. C. Sud, C. M. Taylor, D. Verseghy, R. Vasic, Y. Xue, and T. Yamada (2004). Regions of strong coupling between soil moisture and precipitation. *Science 305*(5687), 1138–1140. 22

Kraus, H. (2004). *Die Atmosphäre der Erde: Eine Einführung in die Meteorologie*. Springer. 3, 7, 8

Kuttler, W. (2008). *Klimatologie*. Schöningh. 2, 7

Legates, D. R., R. Mahmood, D. F. Levia, T. L. DeLiberty, S. M. Quiring, C. Houser, and F. E. Nelson (2010). Soil moisture: A central and unifying theme in physical geography. *Progress in Physical Geography 35*(1), 65–86. 3, 18, 23

Liu, Y., R. de Jeu, A. van Dijk, and M. Owe (2007). Trmm-tmi satellite observed soil moisture and vegetation density (1998–2005) show strong connection with el nino in eastern australia. *Geophysical Research Letters 34*. 72

Liu, Y., W. Dorigo, R. Parinussa, R. de Jeu, W. Wagner, M. McCabe, J. Evans, and A. van Dijk (2012). Trend-preserving blending of passive and active microwave soil moisture retrievals. *Remote Sensing of Environment*. 3, 35, 37, 38

Liu, Y. Y., M. F. McCabe, J. P. Evans, A. I. J. M. van Dijk, R. A. M. de Jeu, and H. Su (2010). Influence of cracking clays on satellite observed and model simulated soil moisture. *Hydrology and Earth System Sciences Discussions 7*(1), 907–927. 55

Liu, Y. Y., A. I. J. M. van Dijk, R. A. M. de Jeu, and T. R. H. Holmes (2009). An analysis of spatiotemporal variations of soil and vegetation moisture from a 29-year satellite-derived data set over mainland australia. *Water Resour. Res. 45*. 23, 35, 38, 54, 59

Lorenz, E. N. (1956). Empirical orthogonal functions and statistical weather prediction. technical report, statistical forecast project report 1. Technical report, Dept. of Meteor., MIT. 40

Lorenz, E. N. (1970). Climate change as a mathematical problem. *J. Appl. Meteor 9*, 325–329. 40

Naeimi, V., Z. Bartalis, and W. Wagner (2009). Ascat soil moisture: An assessment of the data quality and consistency with the ers scatterometer heritage. *Journal of Hydrometeorology 10*, 555–563. 37

Owe, M., R. de Jeu, and T. Holmes (2008). Multisensor historical climatology of satellite-derived global land surface moisture. *J. Geophys. Res. 113*. 37

Pathe, C., W. Wagner, D. Sabel, M. Doubkova, and J. B. Basara (2009). Using envisat asar global mode data for surface soil moisture retrieval over oklahoma, usa. *IEEE Trans. On Geo. and Rem. Sens. 47*. 31

Rasmusson, E., A. P.A., C. W.Y., and J. J.B. (1981). Biennial variations in surface temperature over the united states as revealed by singular decomposition. *Monthly Weather Review 109*, 587–598. 49, 50

Robock, A., K. Y. Vinnikov, G. Srinivasan, J. K. Entin, S. E. Hollinger, N. A. Speranskaya, S. Liu, and A. Namkhai (2000). The global soil moisture data bank. *Bull. Amer. Meteorol. Soc. 81*, 1281–1299. 24

Saji, N. H., B. N. Goswami, P. N. Vinayachandran, and T. Yamagata (1999). A dipole mode in the tropical indian ocean. *Nature 401*(6751), 360–363. 11

Schmugge, T. (1985). *Remote sensing of soil moisture*. Anderson M, Burt T (eds) Hydrological forecasting, Wiley, New York. 23

Schönwiese, C. (1994). *Klimatologie*. Uni-Taschenbücher M. E. Ulmer. 7

Schönwiese, C. (2000). *Praktische Statistik für Meteorologen und Geowissenschaftler*. Borntraeger. 38, 39, 40

Solomon, S., D. Qin, M. Manning, Z. Chen, M. Marquis, K. Averyt, M. Tignor, and H. Miller (2007, September). *Climate Change 2007 - The Physical Science Basis: Working Group I Contribution to the Fourth Assessment Report of the IPCC*. Cambridge, UK and New York, NY, USA: Cambridge University Press. 8, 18

Stöcker, H. (2004). *Taschenbuch der Physik*. Deutsch. 30

Storch, H. and F. Zwiers (2002). *Statistical analysis in climate research*. Cambridge University Press. 39, 40, 41, 47, 48, 49, 50

Ulaby, F. T., R. K. Moore, and A. K. Fung (1981). *Microwave Remote Sensing: Active and Passive. Vol. I – Microwave Remote Sensing Fundamentals and Radiometry*. Reading, MA, USA: Addison-Wesley, Advanced Book Program. 27

Ulaby, F. T., R. K. Moore, and A. K. Fung (1986). *Microwave Remote Sensing: Active and Passive. Vol. III – Volume Scattering and Emission Theory, Advanced Systems and Applications*. Dedham, MA, USA: Artech House, Inc. 31, 32

Ummenhofer, C. C., M. H. England, P. C. McIntosh, G. A. Meyers, M. J. Pook, J. S. Risbey, A. S. Gupta, and A. S. Taschetto (2009). What causes southeast australia's worst droughts? *Geophys. Res. Lett. 36*. 59

Wagner, W., R. d. J. P. v. O. (2009, 4–8 May). Towards multisource global soil moisture datasets for unravelling climate change impacts on water resources. *Electronic Proceedings of the 33rd International Symposium on Remote Sensing of Environment (ISRSE)*. 22

Wagner, W., G. Lemoine, and H. Rott (1999). A method for estimating soil moisture from ers scatterometer and soil data. *Remote Sensing of Environment 70*(2), 191–207. 37

Wagner, W., K. Scipal, C. Pathe, D. Gerten, W. Lucht, and B. Rudolf (2003). Evaluation of the agreement between the first global remotely sensed soil moisture data with model and precipitation data. *Journal of Geophysical Research D: Atmospheres 108*. 24

Walker, J., G. Willgoose, and J.D.Kalma (2004, June). In situ measurements of soil moisture: a comparision of techniques. *J. Hydrol. 293*(1–4), 85–99. 24

Wang, J. and T. Schmugge (1980). An empirical-model for the complex dielectric permittivity of soils as a function of water-content. *IEEE Transactions on Geoscience and Remote Sensing 18*, 288–295. 37

Wilks, D. S. (1995). *Statistical methods in the atmospheric sciences: an introduction*. Number v. 59 in International geophysics series. Academic Press. 39, 41, 43, 45, 51, 52

Woodhouse, I. H. (2006). *Introduction to Microwave Remote Sensing*. Boca Raton, FL, USA: CRC Press. 26, 27, 28, 29, 31, 32, 33, 49